DEVELOPMENT OF WHOLE SYNTHETIC ENZYME-LIQUID CRYSTAL PLATFORMS FOR NEXT GENERATION SENSOR APPLICATIONS

A THESIS SUBMITTED TO
THE GRADUATE SCHOOL OF NATURAL AND APPLIED SCIENCES
OF
MIDDLE EAST TECHNICAL UNIVERSITY

BY

DENİZ KARAMAN

IN PARTIAL FULFILLMENT OF THE REQUIREMENTS
FOR
THE DEGREE OF MASTER OF SCIENCE
IN
CHEMICAL ENGINEERING

AUGUST 2025

Approval of the thesis:

DEVELOPMENT OF WHOLE SYNTHETIC ENZYME-LIQUID CRYSTAL PLATFORMS FOR NEXT GENERATION SENSOR APPLICATIONS

submitted by **DENİZ KARAMAN** in partial fulfillment of the requirements for the degree of **Master of Science** i**n Chemical Engineering, Middle East Technical University** by,

Prof. Dr. Naci Emre Altun
Dean, **Graduate School of Natural and Applied Sciences** _____

Prof. Dr. Yusuf Uludağ
Head of the Department, **Chemical Engineering** _____

Assoc. Prof. Dr. Emre Büküşoğlu
Supervisor, **Chemical Engineering, METU** _____

Assoc. Prof. Dr. Salih Özçubukçu
Co-Supervisor, **Chemistry, METU** _____

Examining Committee Members:

Prof. Dr. Nihal Aydoğan
Chemical Engineering, Hacettepe University _____

Assoc. Prof. Dr. Emre Büküşoğlu
Chemical Engineering, METU _____

Assoc. Prof. Dr. Salih Özçubukçu
Chemistry, METU _____

Assoc. Prof. Dr. Nazar İleri Ercan
Chemical Engineering, METU _____

Asst. Prof. Dr. Necip Berker Üner
Chemical Engineering, METU _____

Date: 29.08.2025

I hereby declare that all information in this document has been obtained and presented in accordance with academic rules and ethical conduct. I also declare that, as required by these rules and conduct, I have fully cited and referenced all material and results that are not original to this work.

Name Last name : Deniz Karaman

Signature :

ABSTRACT

DEVELOPMENT OF WHOLE SYNTHETIC ENZYME-LIQUID CRYSTAL PLATFORMS FOR NEXT GENERATION SENSOR APPLICATIONS

Karaman, Deniz
Master of Science, Chemical Engineering
Supervisor : Assoc. Prof. Dr. Emre Büküşoğlu
Co-Supervisor: Assoc. Prof. Dr. Salih Özçubukçu

August 2025, 127 pages

Liquid crystal (LC)–aqueous soft interface sensors have shown potential for a wide range of analytes, including the tracking of their reactions. While these sensors have shown promise in studying enzymatic activity, their utilization has been dominated by natural enzymes. In this thesis, we introduce a whole-synthetic approach for detecting molecular species through their interactions with enzyme mimics. We employed highly stable fullerene-based synthetic enzyme mimics and performed structural and response characterizations of the LC–aqueous interfaces to track the catalytic hydrolysis of *p*-nitrophenyl acetate (*p*NPA) in solutions in contact with nematic 4-pentyl-4′-cyanobiphenyl (5CB) droplets. Building upon this approach, we introduce chemical modifications to these enzyme mimics to explore chemistry-dependent response characteristics of LC–aqueous interfaces. We employed polarized light microscopy to monitor temporal configuration changes of 5CB droplets during hydrolysis, while interfacial tension measurements and UV–Vis spectrophotometry provided insights into adsorption characteristics, interfacial structuration, and reaction kinetics. Our findings reveal two distinct interfacial structuring: enzyme-mimic–immobilized interfaces and interfaces characterized by

a dynamic adsorption–desorption equilibrium of enzyme mimics, with no influence of LCs on the reaction kinetics. We showed that LC droplets exhibit an instantaneous response originating from bulk enzyme mimic–substrate interactions, with recovery times governed by the bulk phase composition. The tailored modifications of enzyme mimics strongly affect the LC droplet responsiveness to enzymatic *p*NPA hydrolysis. Overall, the design flexibility of these fullerene-based enzyme mimics enables precise tuning of interfacial properties, enhancing LC sensor sensitivity and supporting their application in biochemical sensing, environmental monitoring, and diagnostics. These findings offer new insights into LC-based sensing systems adaptable to diverse substrates and enzyme–substrate interactions.

Keywords: Liquid Crystals, Emulsions, Enzyme Mimics, Hydrolysis, Response.

ÖZ

YENİ NESİL SENSÖR UYGULAMALARINA YÖNELİK TAM SENTETİK ENZİM-SIVI KRİSTAL PLATFORMLARININ GELİŞTİRİLMESİ

Karaman, Deniz
Yüksek Lisans, Kimya Mühendisliği
Tez Yöneticisi: Doç. Dr. Emre Büküşoğlu
Ortak Tez Yöneticisi: Doç. Dr. Salih Özçubukçu

Ağustos 2025, 127 sayfa

Sıvı kristal (LC)–sulu yumuşak arayüzey sensörleri, reaksiyonlarının takibi de dahil olmak üzere çok çeşitli analitlerin takibi için potansiyel gösterir. Bu sensörler, enzimatik aktivitelerin incelenmesinde umut verici sonuçlar vermiş olmasına rağmen, kullanımları büyük ölçüde doğal enzimlerle sınırlı kalmıştır. Bu tezde, enzim taklitleriyle olan etkileşimler aracılığıyla moleküler türlerin tespitine yönelik tamamen sentetik bir yaklaşım sunuyoruz. Yüksek stabiliteye sahip fulleren-bazlı sentetik enzim taklitlerini kullanarak, LC–sulu arayüzeylerin yapısal ve tepki özelliklerini karakterize ettik ve nematik 4-pentil-4′-siyanobifenil (5CB) damlacıklarıyla temas eden çözeltilerde *p*-nitrofenil asetatın (*p*NPA) katalitik hidrolizini izledik. Bu yaklaşıma dayanarak, LC-sulu arayüzlerin enzim taklitlerinin kimyasına bağlı tepki özelliklerini keşfetmek için bu enzim taklitlerine kimyasal modifikasyonlar uyguladık. Hidroliz sırasında 5CB damlacıklarının zamansal konfigürasyon değişikliklerini izlemek için polarize ışık mikroskobu kullandık; arayüzey gerilimi ölçümleri ve UV-Vis spektrofotometrisi ise adsorpsiyon karakteristikleri, arayüzey yapılanması ve reaksiyon kinetikleri hakkında bilgi sağladı. Bulgularımız iki farklı arayüzey yapılanmasını ortaya koydu: enzim

taklitlerinin immobilize olduğu arayüzeyler ve sıvı kristallerin reaksiyon kinetiği üzerinde hiçbir etkisi olmadığı, enzim taklitlerinin dinamik adsorpsiyon-desorpsiyon dengesiyle karakterize edilen arayüzeyler. LC damlacıklarının anlık yanıtlarının, yığın fazda gerçekleşen enzim taklidi–substrat etkileşimlerinden kaynaklandığını ve geri dönüş sürelerinin yığın fazın kompozisyonu tarafından belirlendiğini gösterdik. Enzim taklitlerinin özelleştirilmiş modifikasyonları, LC damlacıklarının enzimatik pNPA hidrolizine tepkisini güçlü bir şekilde etkiledi. Genel olarak, fulleren-bazlı enzim taklitlerinin tasarım esnekliği, arayüzey özelliklerinin hassas bir şekilde ayarlanmasını sağlayarak LC sensör hassasiyetini artırmakta ve biyokimyasal algılama, çevresel izleme ve teşhis uygulamalarını desteklemektedir. Bu bulgular, çeşitli substratlar ve enzim–substrat etkileşimlerine uyarlanabilen LC tabanlı sensör sistemlerine dair yeni bir perspektif sunuyor.

Anahtar Kelimeler: Sıvı Kristaller, Emülsiyonlar, Enzim Taklitleri, Hidroliz, Tepki.

To all my loved ones

ACKNOWLEDGMENTS

I am deeply appreciative of my advisor, Assoc. Prof. Emre Büküşoğlu, whose exceptional guidance, inspiring vision, and unwavering support have greatly shaped this thesis and my academic growth. His insightful feedback, patience, and inspiration gave me the confidence to overcome challenges and refine my scientific thinking. I also warmly acknowledge my co-supervisor, Assoc. Prof. Salih Özçubukçu, for his valuable suggestions and continuous motivation. I extend my appreciation to Aytül Saylam for her support and guidance during this work, and to Elif Akar for her significant contributions to this research.

I would like to express my deepest gratitude to my family: my mother, Özlem Karaman, my father, İbrahim Karaman, and my siblings, Mine and Umut Karaman, for their endless love, support, and sacrifices. I am especially thankful to the youngest and sweetest member of our family, Badem, whose playful nature and boundless energy kept me motivated during the most challenging moments. I would also like to sincerely thank Barış Dereli; your unconditional support, love, and encouragement, along with your patience and understanding, gave me the strength to continue through difficult times, and your presence made this accomplishment truly meaningful. I am so grateful to have shared this journey with you.

I would like to sincerely thank the alumni and current members of the Soft and Functional Materials Research Group. I am especially grateful to Cansu Erdil, İrem Özen, and Cansu Dedeoğlu for their invaluable friendship and for sharing this academic journey with me, not only in the laboratory but throughout our university years. I will truly miss the times we spent together. I am also thankful to Gülce İlhan and Ayşe Nurcan Özşahin Işılak for the pleasure of working with you and for sharing this journey. I extend my gratitude to Aslı Karausta, Özge Batır, and Ali Akman for their invaluable guidance and support. I would like to thank Yiğit Bora Öztürk, Pouriya Esmaeilzadeh, and Akrema; it was a pleasure to work with you.

This work was funded by The Scientific and Technological Research Council of Turkey (TÜBİTAK) through grant number 222Z147.

TABLE OF CONTENTS

LIST OF TABLES

TABLES

LIST OF FIGURES

FIGURES

CHAPTER 1

INTRODUCTION

Liquid crystals (LC) are a unique state of matter with properties that lie between a crystalline solid and an isotropic liquid. They exhibit both long-range orientational ordering, similar to crystalline solids, and the ability to flow when stress is applied, similar to isotropic liquids.[1,2] When temperature alone controls the phase behavior of LCs, they are classified as thermotropic, remaining thermodynamically stable within a certain temperature range, as represented in Figure 1.1a. Thermotropic LCs exhibit increased mobility but a loss of long-range orientational order as the temperature rises, and their phase changes to isotropic. Within the class of thermotropic LCs, the nematic phase is the most extensively studied LC phase. For example, 4-cyano-4'-pentylbiphenyl (5CB) is an oily compound that exhibits nematic phase behavior at room temperature. It is one of the most commonly used thermotropic nematic LCs, and its molecular structure is presented in Figure 1.1b. Its constituent rod-shaped LC molecules are known as mesogens.[3] In nematic phases, mesogens exhibit orientational order along the uniform director (denoted as n in Figure 1.1c) extending up to 100 μm in length, but they lack long-range positional order. The long-range arrangement of mesogens, relative to the molecular scale, gives LCs both anisotropic mechanical characteristics and optical birefringence. The mesogenic molecules can experience two different refractive indices, which are extraordinary (n_e) and ordinary (n_o), as shown in Figure 1.1c. Birefringence ($\Delta n = n_e - n_o$) is the difference between these direction-dependent refractive indices, and it allows mesogen orientation characterization using polarized optical microscopy.[4,5] This property also facilitates the easy tracking of orientational changes in confined geometries or in response to external stimuli.

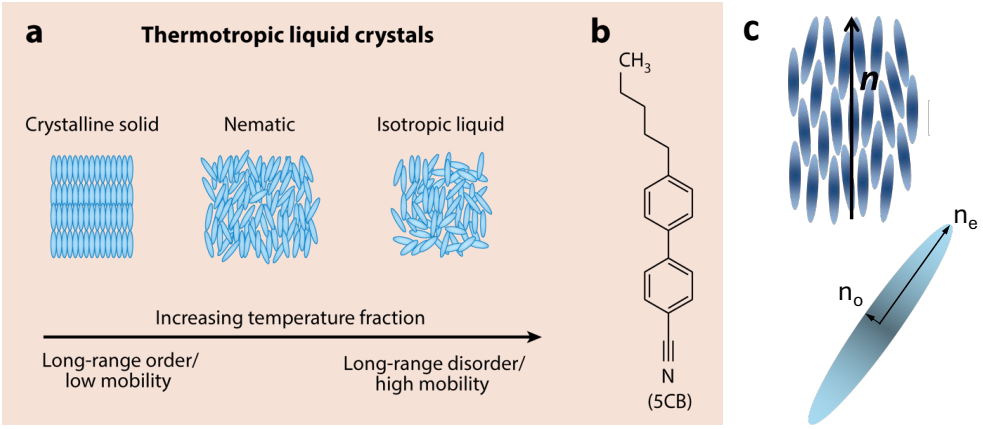

Figure 1.1. The schematic illustration of (a) the temperature-dependent phase behavior of thermotropic LCs, (b) molecular structure of 4-cyano-4'-pentylbiphenyl (5CB), exhibiting the nematic phase behavior at room temperature (Reprinted with permission.[1]), (c) ordering of nematic LCs, with n_e and n_o representing the two refractive indices of the liquid crystal mesogen.

The anisotropic optical properties of LCs offer significant advantages for their use in optical, photonic, electronic, and other applications.[6–9] Over the past decades, research on LC sensors has been developed for sensitive and selective detection of various molecular-scale substances, including gases, lipids, surfactants, polymers, proteins, peptides, DNA, and more.[4,10–15] These studies have shown that highly sensitive systems that can detect concentrations as low as pg/mL can be developed due to the configurations that arise from confining LCs in droplet geometries.[6] In addition to their molecular sensing capabilities, LC-based sensors can also track the various reactions of these molecules.[16–20] Enzymatic reactions are one of the most notable systems developed for biological applications in these studies.[16,17] These investigations, however, have mostly utilized natural enzymes. The catalytic function of natural enzymes depends on their complex architectures, which must be precisely developed to support appropriate function under certain solution conditions.[21,22] Additionally, the protein adsorption at oil-water interfaces can result in unfolding and denaturation.[23,24] Thus, the stability of natural enzymes and their functionality may be compromised at LC-aqueous interfaces, which have high interfacial energy (with interfacial tensions of ~30 mN/m).[25] Synthetic enzyme

mimics, on the other hand, have been of interest as possible substitutes to natural enzymes, as recent studies demonstrated that they accomplish promising catalytic activity and are shown to be less sensitive to environmental conditions.[26–30] However, enzyme mimics formed through secondary interactions may not be convenient for long-term use under some conditions. Among these enzyme mimic studies, the fullerene-based derivatives offer a robust platform due to their covalently bonded, well-structured frameworks.[30] They are synthesized to mimic esterase activity, where amino acids are immobilized on the fullerenol structure, enabling strong and stable catalytic sites. Compared to their equivalent alternatives in the literature, enzyme mimics synthesized in monad, diad, and triad compositions have been shown to possess higher activation and stability. For example, the representative molecular structures of Fullerenol-Histidine (F-His), Fullerenol-Serine (F-Ser), and Fullerenol-Histidine-Serine (F-HS) enzyme mimics are illustrated in Figure 1.2. Additionally, fullerene-based enzyme mimics serve as single-unit catalysts, facilitating straightforward chemical modifications at interfaces. The functional group modification capabilities enable them to create a highly flexible system that can be tailored to target molecules and interactions.[30–33] Due to these characteristics, the assemblies formed by fullerene-based enzyme mimics and LCs offer highly promising potential for rapid, sensitive, and stable diagnostic systems.

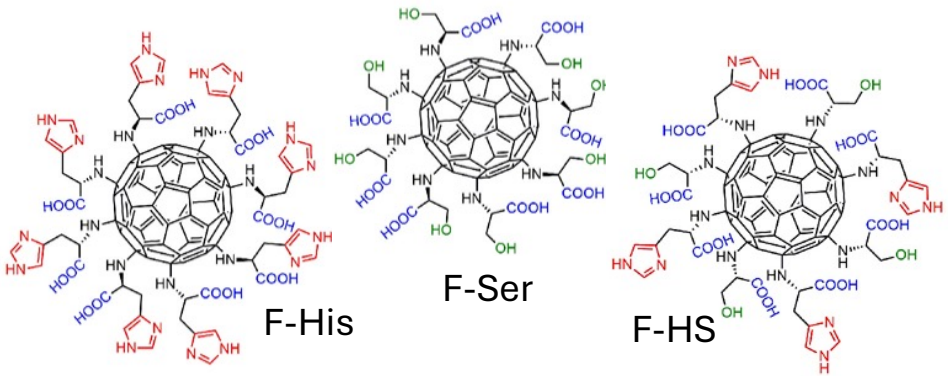

Figure 1.2. Molecular structures of fullerene-based enzyme mimics functionalized with histidine (F-His), serine (F-Ser), and histidine-serine (F-HS) amino acids

immobilized on fullerene scaffolds.[30] Reproduced with permission from Gülseren, G., Saylam, A., Marion, A., Özçubukçu, S. (2021). Fullerene-Based Mimics of Biocatalysts Show Remarkable Activity and Modularity. ACS Applied Materials & Interfaces, 13(38), 45854–45863. Copyright (2021) American Chemical Society.

In this thesis, we sought to develop a platform for the detection of analytes in aqueous media through leveraging the enzyme mimic-substrate interactions at the LC-aqueous interfaces. We utilized emulsion systems by dispersing nematic LC droplets in aqueous phases and investigated their response to fullerene-based enzyme mimics. We tracked the temporal changes in the configuration distributions of the LC droplets upon interactions between the fullerene-based enzyme mimics and the model substrate using polarized optical microscopy. Additionally, we chemically modified the fullerene-based enzyme mimics to examine the effects of these modifications on dynamic droplet configurations during hydrolysis of *p*-nitrophenyl acetate (*p*NPA). Our results demonstrated that the LC droplet responses are strongly dependent on the chemical properties of the enzyme mimics, leading to two different interaction mechanisms: one is an "enzyme immobilized interface", the second is an interface that facilitates a reversible adsorption of enzyme mimics with no influence of LCs on the reaction kinetics. Both mechanisms demonstrate the adaptability and promise of the whole synthetic enzyme-LC platform, which possesses a significant quality that enables the diversification of functional materials to be developed in the future.

CHAPTER 2

LITERATURE REVIEW

Rapid, sensitive, and cost-effective biological diagnostic and detection applications are becoming increasingly important due to their potential for quick responses and widespread use. The development of biological diagnostic systems usually involves monitoring changes in conductivity, color, or charge that arise from the interaction of target molecules with enzymes or biomaterials (such as aptamers or antibodies) immobilized on solid substrates.[34–36] In contrast to solid interfaces, which frequently require complex surface modifications for effective molecular functionality, liquid-liquid soft interfaces offer significant engineering opportunities because they allow easy chemical exchange and significant molecular mobility in physiological conditions.[37–39] The dynamic adaptability of soft interfaces facilitates their use in biological interactions, and they become beneficial for important applications such as sensing and targeted delivery.[38] Because of their capacity to facilitate dynamic molecular interactions while possessing optical responses to these changes at their interfaces, the design based on soft interfaces formed by intersecting the LCs and aqueous phases is a transformative path for biomolecular sensing.[1,4,7,13,14,16,40] Thus, in comparison to systems based on solid material platforms, those built on soft material platforms can provide notable benefits for automation and practical application.

LCs are soft materials, and it has been demonstrated that their orientation change according to the size, shape, and surface properties of their surrounding environments.[41] This responsiveness originates from three key concepts unique to LCs, which distinguish them from isotropic liquids.[1,2,42] These concepts are surface-induced ordering, also known as surface anchoring, elasticity, and topological

defects. Surface anchoring stems from the intermolecular interactions between LCs and their contacting surfaces. In the absence of external fields, mesogens adopt a preferred orientation, which is called the easy axis, defined as the lowest free energy orientation of the LC director. When an external field acts on an LC in contact with a surface, the director of the LC may shift away from the easy axis, leading to an increase in free energy of the interface. The interfacial free energy is proportional to the $\sim WL^2$, where W is the anchoring energy ($\sim 10^{-5}$-10^{-6} J/m^2), and L is the characteristic length.

The second key concept, elasticity, results from the long-range orientational ordering of LC mesogens. Elasticity induces a free energy penalty arising from the strain caused by the confinement of molecules into specific geometries, which is called elastic free energy. The three example modes of strain are known as twist, bend, and splay; however, not all modes of strain can be observed for all LCs. With the one elastic constant approximation, the simplest calculation of elastic free energy scales with ~ KL, where K represents the elastic constant of the LCs in the order of 10^{-11} N. The characteristic length estimated with $WL^2/KL=L$ at which the competition between the anchoring energy and elastic energy is observed is between 1 to 10 micrometers, and this size range is important for adjusting the sensor response and sensitivity.[41,42]

The final key concept is the topological defects. When LC is confined within certain geometries, the continuous strain of the LC director cannot maintain the interfacial anchoring conditions, leading to local melting in the regions of LC where the strain is high enough. Although these regions represent macroscopic singularities in the LC ordering profile, on the microscopic scale, the cores of singular defects are nanoscopic areas of LC without orientational ordering. When melting the core has a lower free energy cost than straining the LC inside the core's volume, the process of local melting takes place, and typically, the core size of defects is 10 nm.

Guided by these three key concepts of LCs, the orientation of LC molecules is strongly dependent on the geometry of the confining volume (due to elasticity) and the chemical properties of their contacting interfaces (due to interfacial

anchoring). These concepts are frequently utilized in the design of LC-based sensors to adjust their sensitivity and develop different strategies. In this study, we also designed our systems by leveraging these fundamental principles.

LCs are being developed as soft interface sensor platforms that are energy-efficient, inexpensive, and sensitive. For a variety of analytes, such as lipids, surfactants, peptides, proteins, viruses, nanoparticles, and polymers, thermotropic LC-based sensor systems have been modified.[1,9] These studies were designed based on the ordering transitions of LCs, which result from their interactions with contacting surfaces and depend on the structure and concentration of the analytes at these interfaces. These transitions can be easily captured by simple polarized optical microscopy due to the birefringence of LCs.[4,5] The LC-based sensors possess surfaces that are highly sensitive to even weak external stimuli, often referred to as stimuli-responsive surfaces.[1] For example, the ordering transitions of LC and their corresponding optical images observed under a microscope are shown in Figure 2.1. Homeotropic anchoring is the alignment of the LC molecules perpendicular to the surface. When the alignment of molecules is parallel to the surface, it is called planar anchoring, as shown in Figure 2.1a. If the orientation of LC changes from homeotropic to planar anchoring due to external stimuli, their corresponding optical images under crossed polarizers (two linear polarizers that are 90° apart from one another) change from dark to bright (Figure 2.1b). The optical changes observed between these two surface anchoring results from the light polarization differences based on the orientation of the LC molecules.[1] Because of these characteristics, LCs can be thought of as sensor systems that ”optically amplify” the molecular interactions at their interfaces.

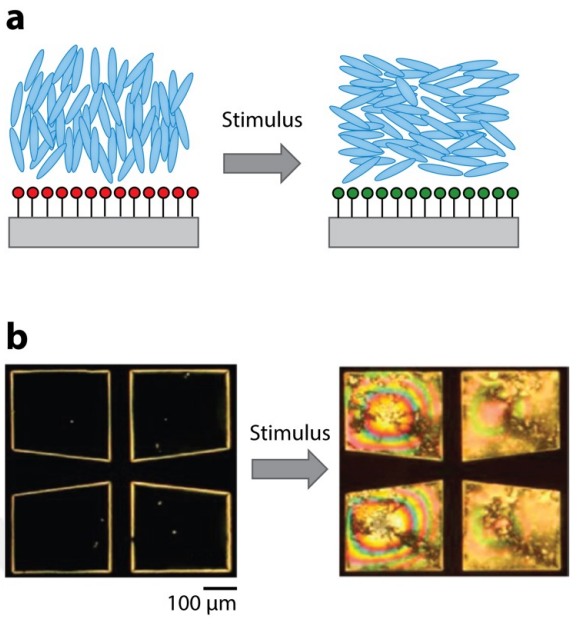

Figure 2.1. (a) A schematic illustration of a stimuli-responsive interface that induces a transition in LC orientation from homeotropic to planar anchoring. (b) The optical appearance of LC corresponding to the homeotropic to planar anchoring change under crossed polarizers. (Reprinted with permission.[1])

LC-based sensors can be created with different designs, and each of them possesses unique benefits for particular applications. For example, in the literature, there are designs of LCs confined between two functioning solid surfaces, usually glass.[43–46] In these studies, generally, the surface that is in contact with the LC is coated with the target analyte molecules, such as dipeptide molecules and their mixtures, DNA molecules, viruses, and proteins. Although the contacting surfaces can offer excellent selectivity, these sensors can respond to analytes within a minimum of a few hours, since they usually require multiple steps for the preparation of functional surfaces.[44,47,48] Among such studies, Schwartz et al. utilized LCs to investigate the characteristics of DNA molecules on solid surfaces. They studied the LC alignment changes when the single and double-stranded DNA (ssDNA and dsDNA) molecules were in contact with the LC.[44] They observed that LC molecules were aligned in the extension direction by single-stranded DNA molecules, and at a tilted angle by double-stranded DNA molecules. Thus, they characterized the DNA

based on the optical images obtained at the LC-solid interface. In the study, established techniques were employed, such as surface modification, DNA purification, and LC cell assembly.

Another LC-based sensor design type involves LCs with a surface in contact with a fluid, generally gas or water.[10,13] For instance, Brake et al. used this type of experimental system. They firstly coated the glass with octadecyltrichlorosilane (OTS) to obtain homeotropic anchoring of LC.[10] Following the placement of copper specimen grids on the glass slides coated with OTS, a tiny amount of 5CB was confined in the grid system. Then the optical cell was immersed in an aqueous solution to investigate the 5CB orientation at the interface contacting with water. This experimental procedure is common for stagnant LC-based systems to ensure that the LC orientation at the interface is affected only by the substances in the aqueous phase. In the study, they investigated how the molecular structure of the surfactants affects the orientation at the LC-aqueous interface. They found that the surfactants with bolaform structure cause the planar anchoring at the interface due to looped conformation; however, classical surfactants such as SDS and C_nTABs (n>8) result in homeotropic anchoring. Additionally, they observed that the LC orientation depends on the aliphatic chain length; with smaller ones (e.g., C_8TAB) causing planar anchoring at lower concentrations.

LC-based sensors can also be designed as LC droplets dispersed in a liquid.[6,41,49–52] When LC is confined in a spherical geometry, the defect formation occurs due to the competition between elastic energy and interfacial anchoring energy. This competition leads to various LC droplet configurations, including bipolar (a), axial (b-c), preradial (d), escaped radial (e), and radial (f), based on the defect location and the LC mesogen alignment in the confined LC medium.[41,49] Because of the LC characteristics, these configurations of LC droplets can be easily distinguished under polarized light, and the corresponding schematic illustrations, bright field, and polarized light micrographs are represented in Figure 2.2. Gupta et al. investigated the formation of different LC droplet configurations by tuning the interfacial anchoring of LCs through the adsorption of the surfactant sodium dodecyl

sulfate (SDS) at the LC-water interface. They demonstrated that varying SDS concentrations dynamically alter the LC interfacial anchoring, leading to changes in defect locations and corresponding changes in droplet configurations.[49] When there is no SDS molecule (0 mM) in the LC-dispersed aqueous phase, the LC droplets exhibit a bipolar configuration, characterized by tangential orientation of LC molecules at the interface and have two point defects positioned at the two opposite poles of the droplet, as shown in Figure 2.2a. Upon increasing the SDS concentration to 1 mM, the LC droplet configuration changes to radial, with LC directors aligned normal to the interface, with a central point defect producing a symmetrical four-petal optical appearance under polarized light as presented in Figure 2.2f. At an SDS concentration of approximately 0.6 mM, the preradial LC droplet configuration is stabilized by a tilted interfacial LC alignment. This configuration is characterized by a single point defect located at the droplet interface, resulting in a specific optical appearance as shown in Figure 2.2d. Between the bipolar and preradial configuration, the axial droplet configuration was exhibited, where the tangential anchoring weakens but remains predominant. A continuous disclination line surrounding the droplet, which is frequently seen as an equatorial ring in polarized light, characterizes this configuration (Figure 2.2b-c). Additionally, before LC droplets adopt the radial configuration, indicative of strong homeotropic anchoring, an escaped radial configuration may appear. In this configuration, the point defect is positioned between the center and interface of the droplet (Figure 2.2e).[2] The LC droplets are easily integrated into complicated aqueous environments, allowing for direct and localized chemical analysis through the formation of particular droplet configurations that depend on analyte concentration. Therefore, analyte concentrations in the liquid environment can be sensitively and quantitatively analyzed by defining these LC droplet configurations using optical microscopy. The surface anchoring energy and elastic free energy inherent to LCs scale with the size of the LC droplets.[1,41] For a nematic LC droplet with radius R, the size range where these two energies compete lies between 1 and 10 μm. This size range plays a crucial role in determining the sensitivity of LC droplets. While droplets smaller than this

range adopt a uniform, strain-free director alignment, larger droplets exhibit configurations to satisfy the surface anchoring conditions at the interface.

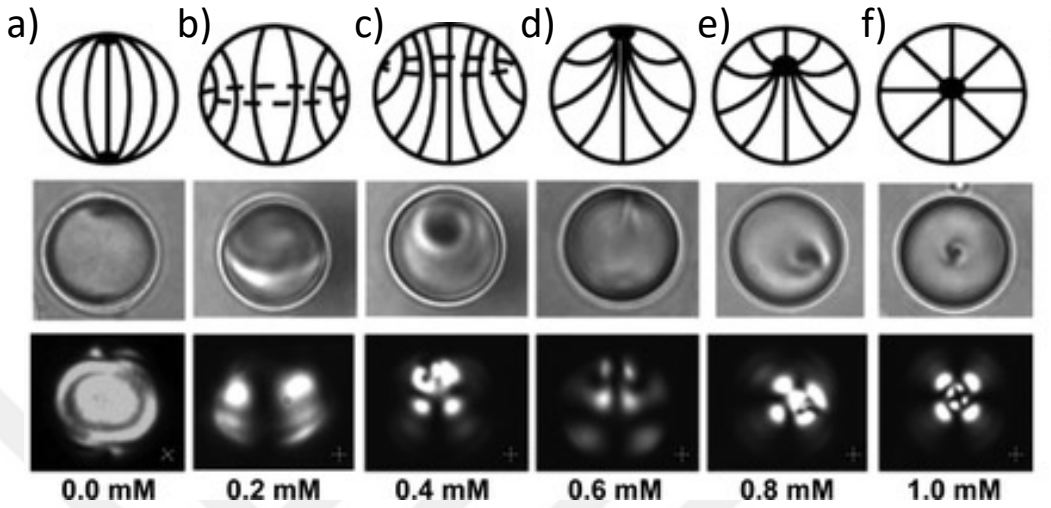

Figure 2.2. Configurations of 5CB LC droplets dispersed in aqueous solutions at varying SDS concentrations, exhibiting bipolar (a), axial (b, c), preradial (d), escaped radial (e), and radial (f) configurations. Top row: schematic illustration of the LC alignment within the droplet, middle row: bright field microscopy images of the LC droplets, bottom row: polarized light microscopy images of the LC droplets.[49] Reproduced with permission from Gupta, J. K., Zimmerman, J. S., de Pablo, J. J., Caruso, F., Abbott, N. L. (2009). Characterization of Adsorbate-Induced Ordering Transitions of Liquid Crystals within Monodisperse Droplets. Langmuir, 25(16), 9016–9024. Copyright (2009) American Chemical Society.

As another example of LC droplet studies, Lin et al. used the micrometer-sized LC droplets dispersed in water to examine how the ordering transition triggered by concentrations of the endotoxin at picogram per milliliter (pg/mL). They hypothesize that at low concentrations, endotoxin triggers LC droplet ordering transitions not by altering anchoring energy (as with lipids like 1,2-dilauroyl-sn-glycero-3-phosphatidylcholine (DLPC) and 1,2-dioleoyl-sn-glycero-3-phosphatidylcholine (DOPC)) but through localized interactions of endotoxin at defect sites of the LC droplets.[6] Thus, when compared with the planar film geometry,

LC droplets are highly sensitive because they can change the LC orientation when the interface concentration is six orders of magnitude lower. Their high sensitivity is one of the key features that distinguishes LC droplet systems. In another LC droplet study, it was investigated that the distinct configuration changes in LC droplets due to the nanoparticle adsorption with different surface functionalities.[52] Sengul et al. utilized the changes in droplet configurations to provide information regarding the physicochemical properties of nanoparticles at the LC droplet interface. They demonstrated the potential of LC droplets for the sensitive detection of nanomaterials and the synthesis of complex anisotropic composite particles. In parallel with these studies, rapid and high-throughput quantification methods for LC droplet systems have been developed. For example, Hamlington et al. utilized a microfluidic flow-focusing system to generate LC droplets with precisely controlled size and uniformity in a silicone oil continuous phase.[53] They investigated how flow rates, channel surface properties, and temperature influence the LC droplet formation. These approaches allow scalable production of LC droplets while maintaining internal defect structures. Additionally, Miller et al. demonstrated that flow cytometry can analyze up to 10,000 LC droplet configurations per second.[54] The variations of the light scattering patterns that arise from the radial and bipolar LC droplet configurations enable their accurate distinction. This method provides fast, quantitative, and statistically robust droplet configuration analysis compared to traditional optical microscopy. Together, these techniques greatly improve the efficiency and analytical power of LC droplet-based sensors.

LC-based sensors can also be designed with the confinement of LC in microcapillaries, as an alternative to the LC thin film systems.[55,56] Additionally, the LC can be confined in microwells in a variety of geometries to investigate the defect position and formation.[57]

When examining these different LC-based sensor designs, LC-aqueous interface systems offer advantages that distinguish them from other designs, such as LC-solid interface systems. Their soft and deformable nature allows for dynamic tuning of LC responses. Additionally, these interfaces enable rapid transport of

molecules to and from the interface and provide enhanced molecular mobility, facilitating interfacial reorganization.[40] As a result, LC-aqueous interfaces are appropriate and useful soft material platforms for quick diagnostics. In our study, we utilized LC droplets dispersed in an aqueous phase due to their suitability for statistical data collection and enhanced diagnostic sensitivity.[6]

LC-aqueous interfaces can be thought of as structured oil-aqueous interfaces. However, the molecular structures adsorbed at these interfaces differ significantly from isotropic oil-aqueous interfaces due to the elasticity of the LC.[58] For example, depending on their concentrations in pure water, traditional, water-soluble surfactants like cetyltrimethyl ammonium bromide (CTAB) and SDS cause a uniform tilt angle at the LC-water interface.[10,59] On the other hand, water-insoluble surfactants with a higher hydrophilic-lipophilic balance (HLB), such as lipids (found in vesicular or micellar forms), cause concentration-dependent clustering and lead to the formation of unique patterns at the interface.[58] These different behaviors are explained with three examples in Figures 2.3, 2.4, and 2.5.

Lockwood et al. investigated how different concentrations of SDS influence the 5CB orientation at the 5CB-aqueous interface by confining the LC in a thin film geometry using a gold grid. They observed that when the SDS concentration increases in the bulk, the birefringence colors of 5CB films homogeneously change, indicating the uniform change in 5CB orientation at the 5CB-aqueous interface, as can be seen in Figure 2.3a.[40] Additionally, they measured the tilt angle of the 5CB at the 5CB-aqueous interface, containing a 0-1 mM SDS range in the bulk. As represented in Figure 2.3b, the 5CB orientation at the 5CB-aqueous interface, which is 90° (planar anchoring) in the absence of surfactant (0 mM), steadily decreases with increasing surfactant concentration, reaching 0° (homeotropic anchoring) at approximately 1 mM SDS. The surfactant concentration-dependent uniform change in the tilt angle of 5CB is attributed to the high solubility of water-soluble SDS molecules in the aqueous phase. This leads to a dynamic adsorption-desorption equilibrium between the adsorbed SDS molecules at the 5CB-water interface and those in the bulk solution.

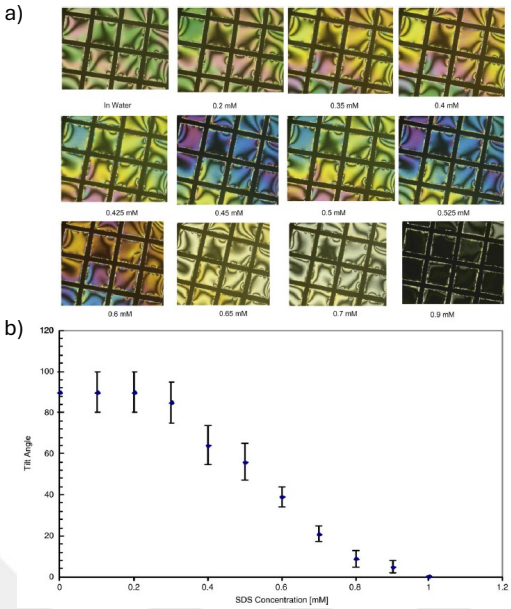

Figure 2.3. (a) Optical appearance of 5CB confined in a thin film geometry within a gold grid and equilibrated with aqueous SDS solutions in the 0-1 mM range, investigated under crossed polarizers. (b) Tilt angle of 5CB at the aqueous–5CB interface, measured relative to the interface normal, as a function of the indicated SDS concentrations in the bulk aqueous phase.[40] Reprinted from Surface Science Reports, 63(6), Lockwood, N. A., Gupta, J. K., Abbott, N. L., Self-assembly of amphiphiles, polymers and proteins at interfaces between thermotropic liquid crystals and aqueous phases, 255–293, Copyright (2008), with permission from Elsevier.

In another study, Gupta et al. worked on the adsorption of DLPC, which is a synthetic phospholipid and has limited solubility in water, at the interface between the nematic LC 5CB and an aqueous phase using thin film geometry. They obtained the optical appearance of DLPC adsorbed at the 5CB-aqueous interface using both polarized light microscopy under crossed polarizers and fluorescence microscopy, as shown in Figure 2.4a and Figure 2.4b.[58] When DLPC adsorbed at the 5CB-aqueous interface, the bright regions in Figure 2.4a represent the lipid-lean domains, and the dark regions represent the lipid-rich regions. The coexistence of these leads to the patterned orientation of the 5CB. Additionally, the corresponding fluorescent

images supported the observation with the polarized light, with the fluorescently tagged DLPC at the 5CB-aqueous interface appearing bright, and lipid-lean regions appearing dark, as represented in Figure 2.4b. In Figure 2.4e, they illustrated the patterned orientation of 5CB, where the DLPC adsorbed interfaces exhibit homeotropic anchoring, and the lipid lean interfaces exhibit planar anchoring at the 5CB-aqueous interface. When they heated the system up to the nematic-isotropic transition temperature, both the birefringence and the lipid lean domains disappeared, as can be seen in Figure 2.4c and Figure 2.4d. The phase diagram of the adsorbed DLPC phase at the 5CB-aqueous interface as a function of temperature and surface fraction is represented in Figure 2.4f. Thus, it has been shown that when DLPC concentrations are lower than those required to complete a monolayer, the adsorption of DLPC leads to the emergence of patterns at the interface due to the existence of a nematic phase. These patterns arise from the phase separation of lipid molecules at the interface, propelled by interactions resulting from LC elasticity.

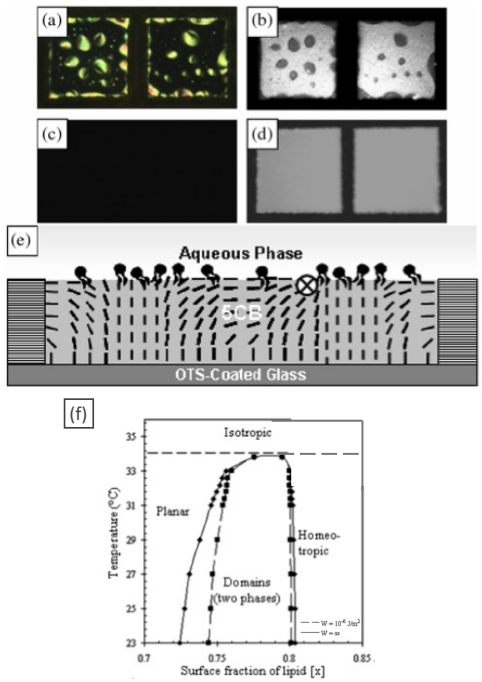

Figure 2.4. (a) Optical images of the 5CB-aqueous interface obtained in the presence of DLPC in the aqueous phase using polarized optical microscopy under crossed

polarizers. (b) The corresponding fluorescent images of the DLPC decorated 5CB-aqueous interface. (c), (d) Optical images of (a) and (b) when the system was heated up to 34°C and equilibrated for two hours, respectively. (e) Illustration of patterned 5CB orientation and lateral distribution of DLPC at the 5CB-aqueous interface corresponding to (a) and (b). (f) The phase diagram of DLPC at the 5CB-aqueous interface as a function of surface fraction of DLPC, and temperature, in both the cases of strong ($W=\infty$) and weak anchoring ($W=10^{-6}J/m^2$). Reprinted with permission from Ref. 58. Permission conveyed through Scientific Publishing and Remittance Integration Services, Inc.

As illustrated in Figures 2.3 and 2.4, the optical responses of LC-aqueous interfaces depend on the structures of the adsorbed molecules at the interface, their interactions with the contacting phases, and their solubilities. The two investigated structures are not limited to these systems and molecules. For example, Gupta and Abbott studied the effect of the electrolyte sodium bromide (NaBr) in the aqueous phase on the adsorption and lateral organization of dodecyltrimethylammonium bromide (DTAB, a cationic, water-soluble surfactant) at the nematic LC-aqueous interface, using micrometer-thick LC films. Figure 2.5b-f presents the polarized light optical images obtained with increasing DTAB concentrations with fixed NaBr solution (1 mM) in the aqueous phase.[59] When there are no surfactant molecules in the aqueous phase, the optical appearance of the 5CB-aqueous interface appears bright, indicating 5CB molecules exhibit planar anchoring at the interface (Figure 2.5b). When the low concentration of 0.01 mM DTAB is equilibrated in the aqueous phase, no significant difference was observed between the non-surfactant case (Figure 2.5c). However, the domain formation is observed at a bulk concentration of 0.04 mM DTAB, and the increase to 0.1 mM DTAB resulted in uniform dark optical appearances (Figure 2.5d-f). From other studies, it was known that when the interface is saturated with surfactant, 5CB exhibits homeotropic anchoring at the 5CB-aqueous interface.[10,40,60] Thus, the observed dark regions at higher bulk DTAB concentrations indicate the areas that have a high interfacial concentration of DTAB, and the bright areas indicate the low interfacial concentration of DTAB. As shown

in Figure 2.5a, a schematic illustration of the experimental system depicts the lateral organization of surfactants at the 5CB-aqueous interface, which is in dynamic equilibrium with the bulk aqueous phase, and the patterned orientation of 5CB corresponding to Figure 2.5d. The phase separation of the surfactant molecules at the 5CB-aqueous interface results from the screening of the electrostatic interaction between their head groups due to the presence of salt in the aqueous phase, and the dominant effect of elastic energy induced by the 5CB film. In this context, the behavior and adsorption mechanisms of fullerene-based enzyme mimics at the 5CB–aqueous interface are unknown due to their structure, which lies between molecular and nanoparticle sizes. Interfacial characterization studies at the 5CB-aqueous interface are an essential aspect of our research.

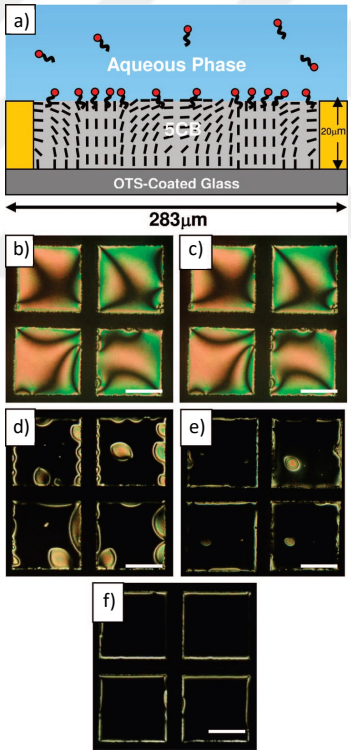

Figure 2.5. (a) Schematic depiction of the experimental setup employed to investigate surfactant adsorption at the aqueous-LC interface. The illustration in (a) depicts the lateral distribution of surfactant and the patterned orientation of 5CB, corresponding to (d). (b-f) Cross-polarized light micrographs of nematic 5CB confined in a 20 μm thick gold grid and equilibrated with aqueous solutions of DTAB

at concentrations of 0, 0.01, 0.04, 0.06, and 0.10 mM, respectively, with each solution containing 1 M NaBr. The scale bar is 150 μm.[59] Reproduced with permission from Gupta, J. K.; Abbott, N. L. (2009). Principles for Manipulation of the Lateral Organization of Aqueous-Soluble Surface-Active Molecules at the Liquid Crystal-Aqueous Interface. Langmuir, 25(4), 2026–2033. Copyright (2009) American Chemical Society.

To date, LC-aqueous interfaced systems have been shown as tools for sensitive and selective detection of chemical species that also include their specific interactions. In addition to explaining surfactants and lipid studies, the wide range of examples includes high precision detection of pollutants such as heavy metals, pesticides in environmental samples, proteins, peptides, DNA, and polymers available in aqueous environments.[4,6,8,9,14,15] Specifically, LC-aqueous interfaces can be designed to facilitate biological applications such as protein recognition and enzymatic assays, allowing for selective detection even in challenging aqueous conditions.[61,62] The versatility of these interfaces for biosensing applications is further demonstrated in recent studies. Also, LC-aqueous interfaces were shown to respond to dynamic chemical changes, providing additional insights into complex catalytic mechanisms.[16–20] Among these studies, the systems involved in enzymatic reactions become notable.[16,17] As an example, Brake et al. have demonstrated the effectiveness of such interfaces in monitoring the enzymatic interactions. The injection of L-α-dilauroyl phosphatidylcholine (L-DLPC) vesicles induces spontaneous monolayer formation at the LC-aqueous interface, resulting in a planar-to-homeotropic ordering transition in the LC. Under polarized light microscopy, this transition is observable as a change in optical appearance from bright to dark, as seen in Figure 2.6a–c.[63] When the natural enzyme, phospholipase A_2 (PLA_2), is introduced into the aqueous solution that contains a lipid monolayer at the LC-aqueous interface, it hydrolyzes the L-DLPC monolayer stereoselectively, producing lysophospholipids and fatty acids that desorb from the interface (Figure 2.6d-e).[16,17,64] The disruption of the lipid monolayer with the enzymatic activity induces a reverse homeotropic-to-planar transition in the LC at the LC-aqueous interface,

observable as bright or patterned optical appearances (Figure 2.6f-h). The characterization of enzyme-substrate interaction kinetics and lipid-protein interactions can be performed with the resulting optically detectable LC transitions, underscoring the potential of LC-aqueous interfaces for label-free biosensing applications. Additionally, as seen in studies presented in Figures 2.4 and 2.5, the enzymatic degradation of phospholipids led to phase separation at the LC-aqueous interface in this study. Depending on the type of phospholipid, if the hydrolysis products desorb from the interface as illustrated in Figure 2.6d-h, the phase separation is temporary. It occurs during enzymatic hydrolysis, ultimately resulting in a homogeneous transition to a planar LC alignment upon completion. However, the chemical structure of the intermediates can influence their accumulation at the interface; this accumulation may be persistent and lead to stable heterogeneous patterns at the LC-aqueous interface that do not result in a homogeneous appearance.[16,17]

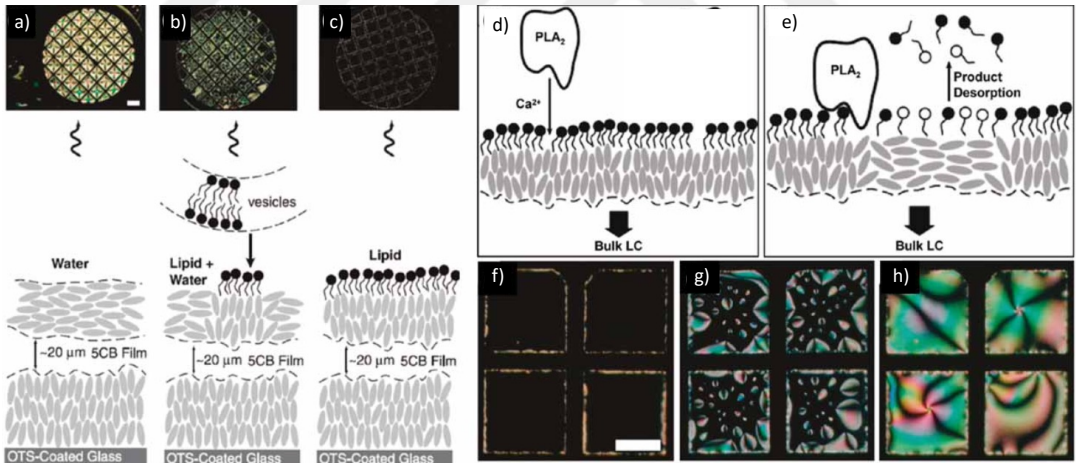

Figure 2.6. (a-c) Optical micrographs (under crossed polarizers) illustrating the spontaneous formation of an L-α-dilauroyl phosphatidylcholine (L-DLPC) monolayer following the injection of 0.1 mM L-DLPC vesicles in tris-buffered saline (TBS), (a) Immediately after injection, (b) ~10–20 minutes post-injection, (c) 2 hours post-injection. (d–h) Enzymatic hydrolysis of the L-DLPC monolayer upon addition of phospholipase A_2 (PLA_2), catalyzing the production of lysophospholipids and fatty acids that desorb from the interface.[16] Brake, J. M., Daschner, M. K., Luk,

Y.-Y., & Abbott, N. L. (2003). Biomolecular interactions at phospholipid-decorated surfaces of liquid crystals. Science, 302(5653), 2094–2097. Reprinted with permission from AAAS.

The findings of the study described in Figure 2.6 have inspired research on dynamic chemical reactions at LC-aqueous interfaces, where interfacial dynamics are revealed by modulating LC alignment with well-defined intermediates, as those from phospholipid hydrolysis.[16–18] For example, Hartono et al. designed an air-supported LC-based system in order to track the real-time enzymatic hydrolysis of L-DLPC monolayers by phospholipases such as PLA_2, phospholipase C (PLC), and phospholipase D (PLD) at the LC-aqueous interface caused by the orientational change of LC induced by molecular interaction.[18] In another study, Hussain et al. monitored lipase activity using phospholipid DOPC at the LC-aqueous interface. DOPC vesicles spontaneously form a monolayer at the LC-aqueous interface, resulting in homeotropic anchoring of the LC molecules at the interface.[65] When lipases, which are natural enzymes that hydrolyze lipids, are present in the system, the lipid monolayer is disturbed and destroyed. The disruption of the lipid monolayer creates local chemical gradients that cause LC ordering transitions at the LC-aqueous interface, which can be observed as a change in optical appearance. Thus, they can directly determine lipase activity, but their LC-based sensor is limited to single use since the hydrolysis products accumulate and remain at the LC-aqueous interface.

In addition to studies on the enzymatic hydrolysis of lipids at the LC-aqueous interface, the enzymatic activities of various enzymes have been investigated forming surfactant-based monolayers at these interfaces.[66–68] For example, Wang et al. utilize the surfactant dodecyl β-d-glucopyranoside, which forms a monolayer at the LC-aqueous interface and induces homeotropic anchoring of LC molecules at the interface. When cellulase is introduced into the system, the orientation of LC molecules at the interface changes from homeotropic to planar due to enzymatic hydrolysis, which can be observable as a shift from dark to bright optical images.[67] As presented in Figure 2.7a, they investigated the enzymatic hydrolysis of 0.1 mM

dodecyl β-d-glucopyranoside with different cellulase concentrations and collected time-dependent optical images after the cellulase was introduced to the surfactant-decorated LC-aqueous interface. After adding 0.1 mg/mL cellulase, the bright regions gradually spread and fully covered the square area within 30 minutes. Lower concentrations of cellulase required more time for the complete transition to bright optical appearance, consistent with the slower enzymatic hydrolysis. Additionally, they calculated the coverage ratio of bright area, Br, as a function of time with different cellulase concentrations using the optical images, and observed that enzymatic hydrolysis was not detectable at lower than 0.001 mg/mL cellulase (Figure 2.7b).

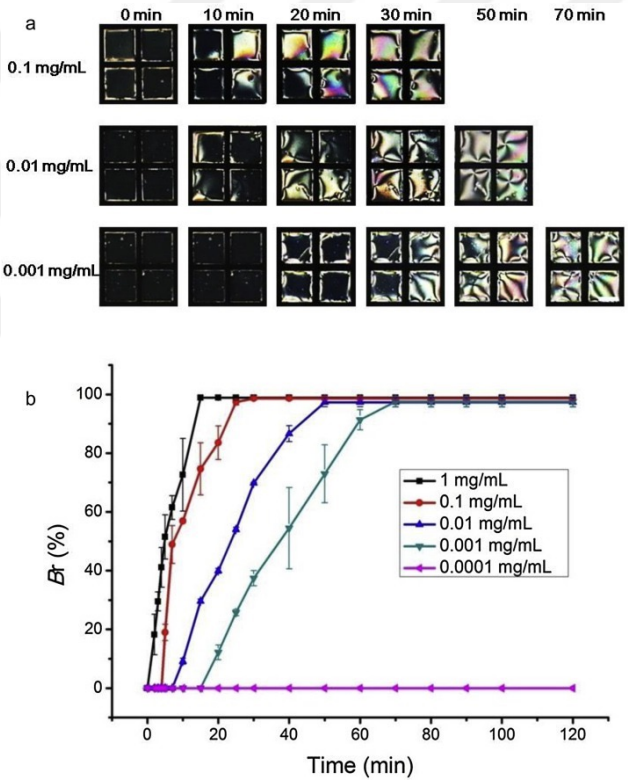

Figure 2.7. (a) The time-dependent optical images of the LC-aqueous interface decorated with 0.1 mM dodecyl β-d-glucopyranoside after introducing 0.1 mg/mL, 0.01 mg/mL, and 0.001 mg/mL cellulase. (b) The coverage ratio of bright regions (Br (%)) based on time-dependent optical images of the LC-aqueous interface after addition of various concentrations of cellulase (n=3). The initial optical images' Br

value was taken as zero due to the dark optical appearance of the LC-aqueous interface decorated with surfactant monolayer.[67] Reprinted from Colloids and Surfaces B: Biointerfaces, 147, Wang, Y., Hu, Q., Tian, T., Gao, Y., Yu, L., A liquid crystal-based sensor for the simple and sensitive detection of cellulase and cysteine, 100–105, Copyright (2016), with permission from Elsevier.

In another study, Sun et al. investigated the enzymatic hydrolysis of non-ionic surfactant dodecyl α-d-glucopyranoside (DDG) by α-glucosidase (AGLU) at the LC-aqueous interface. DDG forms a self-assembled monolayer at the LC-aqueous interface, causing the LC molecules to align perpendicularly at the interface, resulting in a dark optical appearance.[66] However, when a mixture of AGLU and DDG is introduced to the system, the bright optical appearance is observed since the enzymatic hydrolysis of DDG disrupts the DDG monolayer at the LC-aqueous interface, and LC molecules exhibit planar or tilted orientation at the interface. In a study by Lu et al, synthesized surfactant is utilized to form a monolayer at the LC-aqueous interface, and the interaction with the H_2O_2 and surfactant changes the orientation of LC molecules at the LC-aqueous interface from homeotropic to planar. However, the addition of catalase consumes H_2O_2, preventing the LC orientation changes, enabling the detection of catalase activity.[68]

In light of the studies described, systems developed for monitoring enzymatic activity using LCs have been made possible through the adsorption of substrates that can cause orientation changes of LC molecules at the LC interfaces, followed by the degradation of pre-adsorbed interfacial molecules by enzymes transferred from the aqueous phase.[16–18,65–68] With the enzymatic hydrolysis, the degradation of these molecules from the interface is observed, resulting in detectable orientation changes of LC molecules. In contrast, there are limited studies in the literature that are designed to identify and examine the interactions of substrates that do not cause ordering transitions of the LC molecules.[69] However, many target compounds do not cause any orientation change upon adsorption at the LC-aqueous interface. Enzymatically active, soft, tunable, and adaptable LC-aqueous interfaces are necessary for the creation of ready-to-use kits that can be used in a single step for

target molecule detection. These interfaces also enable the development of sensors capable of detecting analytes that do not inherently trigger orientation changes at LC-aqueous interfaces. Such systems will provide significant benefits in target applications for the creation of quick diagnostic kits, systems, and techniques. The study presented in this thesis introduces an LC-based sensor designed to track enzymatic hydrolysis for such analytes.

In a related study, Hu and Jang developed an LC-based sensor to detect urease activity at the LC-aqueous interface using ultraviolet (UV)-treated 5CB. A variety of reaction products were produced when nematic 5CB was subjected to UV light, while 4-cyano-4'-biphenylcarboxylic acid (CBA) served as the main product of the photochemical degradation, which maintains planar anchoring at the aqueous interface (Figure 2.8a).[69] Due to its carboxylic acid group, CBA is highly sensitive to pH and electrolyte concentration in the aqueous phase. As shown in Figure 2.8a, when ammonia is present in the aqueous phase, the resulting hydroxide and ammonium ions cause the UV-treated 5CB alignment to shift from planar to homeotropic, changing the optical appearance from bright to dark. This orientation transition of LC molecules is attributed to the amphiphilic character of deprotonated CBA, which self-assembles at the LC–aqueous interface. They also investigated the urease activity with the system of UV-treated 5CB confined within TEM grids. The UV-treated 5CB exhibits planar anchoring at the LC-aqueous interface when in contact with the DI Water, 100 nM urease, and 0.5 M urea, causing bright appearances, as shown in Figure 2.8b. However, a mixture of 100 nM urease and 0.5 M urea, which are pre-incubated for 30 minutes at room temperature, resulted in a shift of the LC alignment at the LC-aqueous interface from planar to homeotropic, as detectable with the appearance of optical images changing from bright to dark (Figure 2.8b). Since the enzymatic reaction between the urease and urea produces ammonia, it induces the LC orientation as in Figure 2.8a. Therefore, although the substrate urea does not inherently induce any ordering transition in the LC, its enzymatic hydrolysis by urease can be monitored through the orientation change triggered by the hydrolysis reaction product at the LC–aqueous interface.

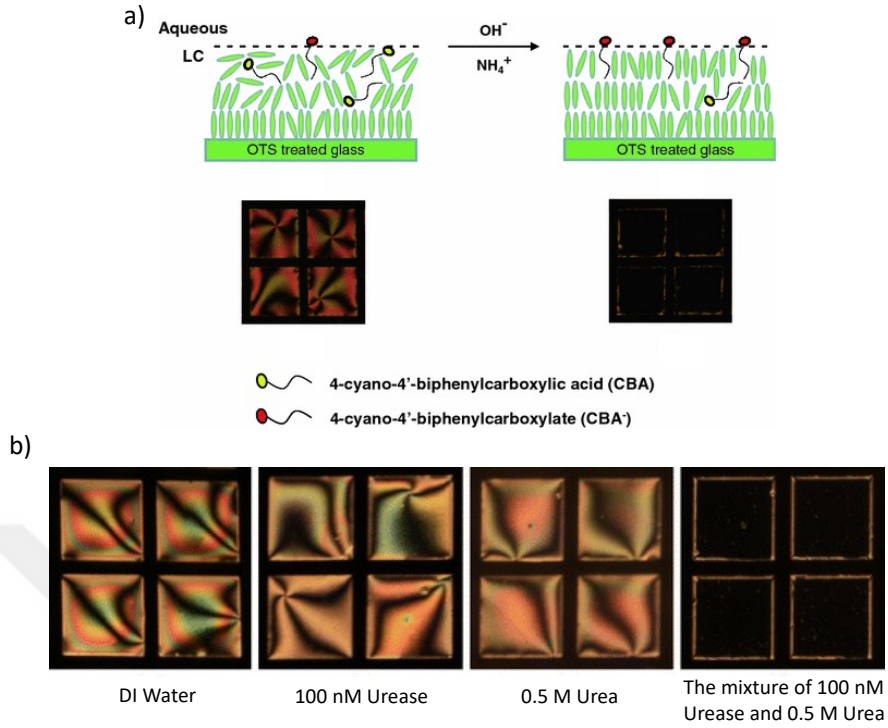

Figure 2.8. (a) An illustration and polarized light optical images showing the orientational change of UV-treated 5CB from planar to homeotropic alignment, initially exhibiting planar alignment in contact with DI water, and transitioning to homeotropic alignment upon exposure to 0.5 M ammonia. (b) Polarized light optical images of the UV-treated 5CB confined in a TEM grid, when in contact with DI water, 100 nM urease, 0.5 M urea, and the pre-incubated mixture of 100 nM urease and 0.5 M urea.[69] Reproduced with permission from Springer Nature: Hu, Q.-Z., Jang, C.-H. (2012). Using liquid crystals for the real-time detection of urease at aqueous/liquid crystal interfaces. Journal of Materials Science, 47(2), 969–975. Copyright (2012) Springer Nature.

These studies have demonstrated that LC–aqueous interfaces can be engineered as highly sensitive platforms for probing enzymatic activities through changes in LC ordering. Although various enzymatic activities have been monitored at these interfaces, most studies have been limited to natural enzymes, and notably, all of the previously discussed LC-based sensor studies for monitoring enzymatic activity exclusively utilize natural enzymes.[16–18,65–69] Despite their versatility, the

macromolecular enzyme immobilization at LC-water interfaces remains challenging due to the high interfacial energy (with interfacial tensions of ~30 mN/m), which can compromise enzyme stability and catalytic efficiency, especially upon dynamically changing environmental conditions and in long-time use.[14,25,70–72] Natural enzymes possess complex architectures that are essential for their catalytic function, requiring the precise formation of the critical structures to facilitate proper function at specific solution conditions.[21,22] Protein adsorption at oil-water interfaces, such as those formed by LC-aqueous interfaces, often leads to unfolding and denaturation, compromising the stability and functionality of natural enzymes at the LC-aqueous interface.[23,24] As a result, although these studies involve natural enzymes, the immobilization of enzymes in an active form at LC–aqueous interfaces has not been observed.

Building upon the insights gained from enzymatic activity detection at LC–aqueous interfaces, these strategies have also been adapted to catalytic systems involving solid–LC interfaces.[73,74] One example is the utilization of stearic acid-doped 5CB droplet patterns on solid surfaces treated with OTS, where LC ordering is triggered by the production of ammonia from urease activity.[73] Similarly, peptide fragments produced with the hydrolysis of casein by proteases alter the appearance of LC patterns at the solid interface.[74] These LC-based sensor systems enable sensitive, label-free tracking of enzymatic activities through dynamic changes in LC orientation. A variety of LC geometries, such as droplets and thin films, can be employed to monitor enzymatic activity, depending on the sensing environment.[75] The scope of LC-based biosensing was further expanded by research demonstrating that protein-coated nanoparticles disrupt phospholipid monolayers at LC-aqueous interfaces, causing homeotropic to planar LC transitions that are observable as dark to bright optical changes.[19]

These insights have evolved into sophisticated photocatalytic systems at LC-solid interfaces, enabling real-time tracking of photocatalytic reactions.[20] Tripathi et al. developed an LC-based system utilizing a thin film of 4′-n-pentyl-4-biphenylcarbonitrile (5CB) supported on anatase TiO_2 (101) surfaces, tested under

synthetic air with a relative humidity of 80% at room temperature. As shown in Figure 2.9a (t=0), before the UV light exposure, optical images under crossed polarizers reveal a bright appearance of the 5CB-anatase (101) interface, indicating planar anchoring of 5CB molecules at the interface with a tilt angle of 85 ± 4° relative to the surface normal. When exposed to 365 nm UV light with an intensity of 1.35 ± 0.05 mW/cm², the anatase (101) surface becomes photoactive, catalyzing the photo-oxidation of 5CB into 4′-cyano-4-biphenylcarboxylic acid (CBCA). This photocatalytic reaction induces a continuous orientational change of 5CB molecules at the interface from planar to homeotropic, observed as a shift from bright to dark optical images within 30 minutes (Figure 2.9a). The calculated tilt angle of 5CB molecules at the 5CB-anatase (101) interface is approximately 0° 30 minutes after UV light exposure, confirming the vertical alignment of the 5CB molecules at the interface. The schematic illustration of the LC-based system before and after exposure to 365 nm UV light is shown in Figure 2.9b. They also showed that the system is highly sensitive to the formation of CBCA by the photocatalytic reaction, 0.09 monolayer surface coverage of it is sufficient for 5CB molecules to exhibit homeotropic anchoring at the 5CB-anatase interface. Using various UV light intensities, Tripathi et al. investigated the dynamic response of 5CB molecules on anatase (101) interface, revealing that lower UV light intensities resulted in a slower 5CB orientation transition, which is consistent with a photocatalytic process driving the transformation (Figure 2.9c).[20]

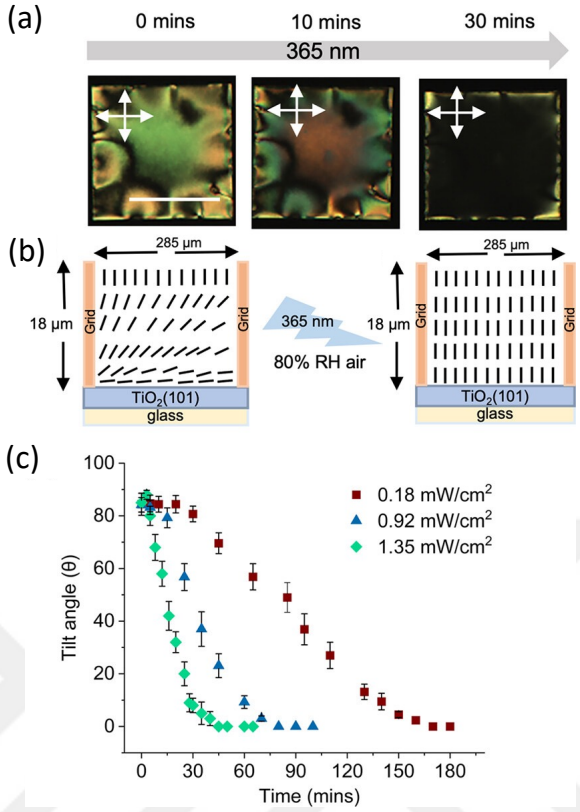

Figure 2.9. (a) Polarized light optical images (crossed polarizers) of 5CB confined in TEM grids supported on anatase TiO_2 (101) surface, captured at 0, 10, and 30 minutes following exposure to 365 nm UV light with an intensity of 1.35 mW/cm^2. Scale bar: 200 µm. (b) An illustration of 5CB molecules alignment at the 5CB-anatase interface at t=0 min (planar) and t=30 min (homeotropic) of UV light exposure. (c) Time-dependent tilt angle of 5CB molecules at the 5CB-anatase interface under 365 nm UV light with various intensities of 0.18 mW/cm^2, 0.92 mW/cm^2, and 1.35 mW/cm^2.[20] Reproduced with permission from Tripathi, A., Wolter, T. J., Twieg, R. J., Mavrikakis, M., Abbott, N. L. (2025). Responsive Liquid Crystalline Materials Based on Interfacial Photocatalytic Processes. Chemistry of Materials, 37(9), 3221–3235. Copyright (2025) American Chemical Society.

Enzymes are highly efficient natural catalysts that have evolved to function with remarkable specificity and activity. Their finely tuned structures and mechanisms have inspired extensive research aiming to understand their catalytic principles and to reproduce their function through synthetic approaches. Among

these efforts, synthetic enzyme mimics have gained considerable attention as promising alternatives to natural enzymes, since recent studies have shown that they can also exhibit significant catalytic performance.[26–29] In these studies, different strategies have been explored to mimic enzymatic activity using simplified, minimalist systems that do not rely on the complex tertiary structures typical of natural enzymes. Figure 2.10 presents some examples of enzyme mimic studies. For instance, Nothling et al. made ester hydrolysis possible using a straightforward yet efficient spatial arrangement of active sites by introducing catalytic triads immobilized on resin surfaces (Figure 2.10a).[28] Al-Garawi et al. described the design of peptides that self-assemble into amyloid-like fibrils, and these fibrils coordinate zinc ions to form catalytically active structures. They can mimic the activity of esterase enzymes (Figure 2.10b).[27] Similarly, Zaramella et al. developed catalytic peptides that self-assemble through electrostatic interactions on the surface of gold nanoparticles. The formed system is capable of catalyzing transesterification reactions (Figure 2.10c).[26] Additionally, Gulseren et al. demonstrated that supramolecular peptide nanostructures can self-assemble through hydrogen bonding and secondary structure formation in the nanostructures. These nanostructures catalyze ester hydrolysis, providing minimalist enzyme-like catalytic function (Figure 2.10d).[29] The versatility of enzyme mimics built through secondary interactions has made them useful alternatives for enzymatic activity replication, but their long-term stability and catalytic efficiency at high-energy LC-aqueous interfaces may remain limited, similar to natural enzymes because of dynamic environmental conditions.

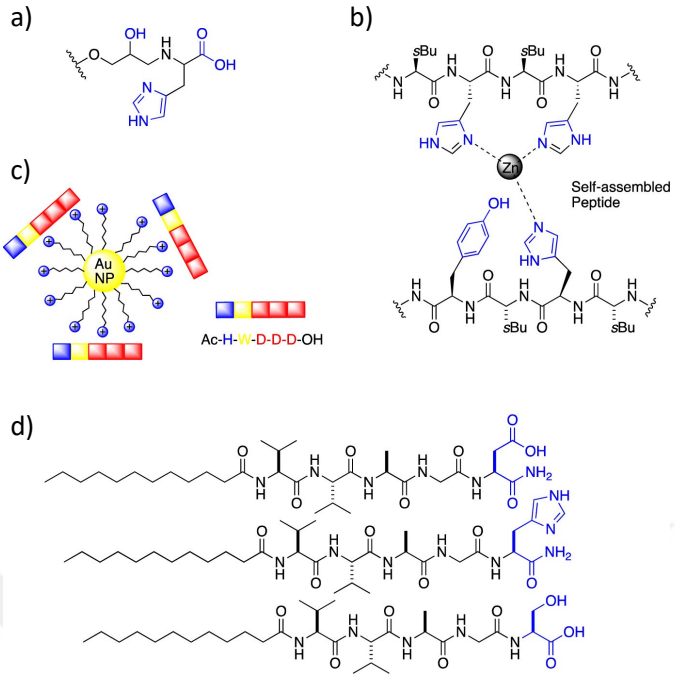

Figure 2.10. Various synthetic enzyme mimic strategies based on amino acids and peptides reported in the literature: (a) catalytic triads immobilized on resin surfaces, (b) amyloid-like fibrils coordinated with zinc ions, (c) peptides conjugated to gold nanoparticles, and (d) supramolecular peptide nanostructures used for synthetic enzyme design. (Reprinted with permission.[26–29])

In addition to these synthetic enzyme mimic studies, a promising subset of synthetic enzyme mimics research involves fullerene-based enzyme mimics, which offer a robust platform due to their covalently bonded, well-structured frameworks.[30–33] Gülseren et al. synthesized the fullerene-based nanocatalyst to mimic the enzymatic activity, particularly hydrolases. To synthesize the nanocatalyst, they first synthesized fullerenol molecules, which have approximately 26-28 hydroxyl groups. These hydroxyl groups were then activated to allow conjugation with amino acids and related compounds to obtain catalytically active fullerene-based structures that mimic enzyme active sites. To create different hydrolase mimics, they functionalized the fullerenol scaffold with either single amino acids such as histidine (His), serine (Ser), and glycine (Gly), or small

molecules that carry key functional groups found in the catalytic site of the target natural enzyme, such as ethanolamine (EA) and histamine (HA), or combinations of them.[30] The molecular structures and synthetic routes of the enzyme mimics are presented in Figure 2.11. The nanocatalysts were prepared in monad, diad, and triad compositions, enabling tailored catalytic functionality. They investigated the kinetic activities of these enzyme mimics with p-nitrophenyl acetate (*p*NPA) substrate, confirming adherence to Michaelis-Menten kinetics, with fullerenol-histidine-serine (F-HS) achieving an early saturation profile, suggesting high catalytic efficiency. Although the fullerene-based enzyme mimics are metal-free catalysts, their catalytic activities are comparable to or even higher than those of metal-containing catalysts reported in the literature. Additionally, the reusability tests demonstrated that the enzyme mimics maintained activity over four consecutive runs without loss, highlighting their exceptional chemical and thermal stability and reusability.

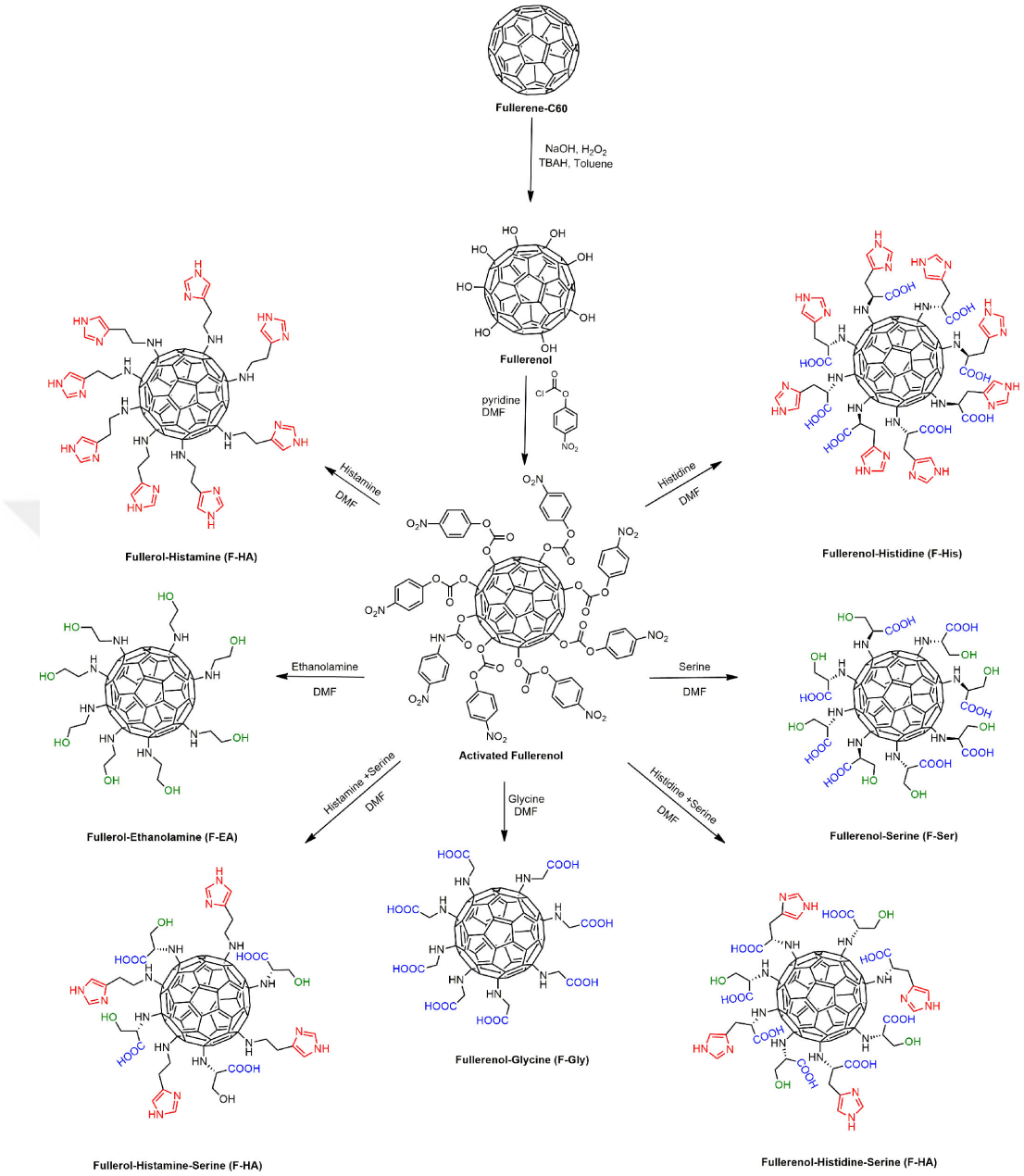

Figure 2.11. Molecular structures and synthesis pathways of fullerene-based enzyme mimics.[30] Reproduced with permission from Gülseren, G., Saylam, A., Marion, A., Özçubukçu, S. (2021). Fullerene-Based Mimics of Biocatalysts Show Remarkable Activity and Modularity. ACS Applied Materials & Interfaces, 13(38), 45854–45863. Copyright (2021) American Chemical Society.

Fullerene-based mimics not only function as single-unit catalysts but also provide a chemically versatile platform that can be readily tailored for specific

molecular interactions at interfaces. Their modular architecture allows for systematic modifications to introduce functional groups capable of recognizing target analytes.[30–33] In a study by Soylemez et al., a fullerene-based catalyst containing serine and histidine (F-HS) was further functionalized with nickel ions to enhance esterase-like activity. This system was employed in the electrochemical detection of acetylcholine (ACh), a biomarker associated with Alzheimer's disease.[31] The resulting interface exhibited both high electroactivity and operational stability, demonstrating the potential of fullerene-based enzyme mimics in biosensing applications that require selective and robust signal generation.

Beyond esterase-like activity, fullerene-based enzyme mimics have also demonstrated phosphatase-like catalytic properties and the ability to promote osteogenic processes.[33] Yeniterzi et al. showed that metal-free fullerene nanostructures catalyze phosphomonoester hydrolysis with higher selectivity and also hydrolyze phosphodiesters using a model substrate, *p*-nitrophenyl phosphate (*p*NPP). Additionally, fullerene-based enzyme mimics induce biomineralization and support bone regeneration in stem cells.[33] In a complementary study, Demirsoy and Gülseren reported that these enzyme mimics also exhibited carbonic anhydrase-like (CA-like) activity by catalyzing the hydration of CO_2 into carbonic acid. This activity was particularly enhanced when the catalysts were modified with histidine and hydroxyl-containing amino acids such as threonine (HT), which structurally resemble the active site of natural CA enzymes.[32] These findings further support the versatility of fullerene-based systems in mimicking different enzymatic functions through surface functionalization. Therefore, fullerene-based synthetic enzymes are highly promising for LC-aqueous interfaces due to their adjustable structure, strong catalytic activity, excellent chemical stability, and rigid framework. Unlike enzyme mimics that rely on weak secondary interactions, their covalently bonded designs ensure consistent and reliable performance, making them ideal for LC-based sensing platforms that require stable and responsive behavior.

In this thesis, we aim to leverage the LC soft material platform, which is well-established in current sensor research, to develop a fully synthetic, stable, tunable,

and adaptable sensor platform. To this end, we investigated LC-synthetic enzyme-based sensors, which are not present in the current literature. Herein, we present materials, techniques, and systems for monitoring enzyme mimic-substrate interactions at LC-aqueous interfaces equilibrated with fullerene-based synthetic enzyme mimics, which have not been previously investigated. By doing so, we aim to overcome the possible challenges in designing and operating an LC-based droplet system for enzymatic interactions. We utilized the responsive and optical properties of the LC medium. Consequently, we report critical findings for sensor technologies that enable the design of rapid, sensitive, tunable, and selective diagnostic and detection applications.

CHAPTER 3

MATERIALS AND EXPERIMENTAL SECTION

3.1 Materials

4-Cyano-4'-pentylbiphenyl (5CB, a room-temperature nematic LC) was purchased from HCCH Jiangsu Hecheng Chemical Materials Co. Ltd. (Nanjing, China). Dimethyl sulfoxide (DMSO) and phosphate-buffered saline (PBS) tablets (pH of 7.4) were obtained from Sigma-Aldrich (St. Louis). 4-Nitrophenyl acetate (*p*NPA) was acquired from EMS (Hatfield, PA). 4-Nitrophenol (*p*NP) was provided by Riedel-de Haën (Seelze, Germany). L-Serine, L-Histidine, m-PEG_5-NH_2, and 4-nitrophenyl chloroformate were obtained from BLD Pharmatech Ltd. (Shanghai, China). Tetrabutylammonium hydroxide (TBAH), 4-Dimethylaminopyridine (DMAP), and dodecyl amine were supplied from Acros Organics (Geel, Belgium). Triethylamine was sourced from Sigma-Aldrich (St. Louis, MO, USA). Fullerene C_{60} (99.5%) was supplied from Nanografi. Co (Ankara, Turkiye). Dichloromethane (DCM) was purchased from Carlo Erba (Milano, Italy). *N,N*-dimethylformamide (DMF), diethyl ether, isopropanol, methanol, ethanol, pyridine, hydrogen peroxide, toluene, sodium hydroxide (NaOH), and deuterated solvents were obtained from Merck (Darmstadt, Germany). All reagents used in experiments and in the synthesis of enzyme mimics were commercially available and used without further purification. Dry solvents used in reactions were directly obtained from the Mbraun MBSPS5 solvent drying system. Heal Force water purification system (Shanghai, China) was used in the experiments to produce deionized water with a resistance of 18.2 MΩ·cm. Glass slides and coverslips were purchased from Marienfeld GmbH (Lauda-Königshofen, Germany). Interfacial tension measurements and UV-Vis spectrophotometric measurements were performed using a 3.5 mL quartz cell, and UV-Vis experiments were conducted using 96-well plates. KUDOS HP Series

53kHz high-frequency ultrasonic cleaner was used for sonication. Nuclear magnetic resonance (NMR) spectra of the compounds were recorded on a Bruker Avance DPX 400 MHz spectrometer.

3.2 Synthesis and Characterization of Enzyme Mimics

3.2.1 Synthesis of Fullerenol

80 mg of fullerene was dissolved in 50 mL of toluene. To this solution, 2 mL of NaOH (1 g/mL), 5-6 drops of 30% hydrogen peroxide, and tetrabutylammonium hydroxide (40 wt%) were added sequentially. The reaction mixture was stirred vigorously at room temperature for five days. Over time, the toluene solution became colorless, and the aqueous phase turned brown, indicating the attachment of hydroxyl groups to fullerene. After the removal of toluene, ethanol was added to the aqueous phase, causing fullerenol to precipitate as a dark brown solid. The solid was filtered and washed several times with ethanol to remove any excess reagents. Thermogravimetric analysis was first carried out for fullerene (Appendix A, Figure A. 1). Subsequently, the number of hydroxyl groups substituted on the fullerenol core was calculated to be 26 based on its thermogravimetric analysis (Appendix B, Figure B. 1).

3.2.2 Synthesis of Activated Fullerenol

80 mg of fullerenol was suspended in anhydrous N,N-dimethylformamide (DMF), and the mixture was sonicated for 1 hour to obtain a homogeneous suspension. To this suspension, 400 mg of p-nitrophenyl chloroformate, 2 mL of anhydrous pyridine, and 20 mg of N,N-dimethylaminopyridine were added while maintaining the temperature at 0°C. The reaction mixture was stirred under a nitrogen atmosphere at room temperature for 48 hours, with sonication applied for 1 hour every 8 hours. As the reaction progressed, solubility increased, and the solution

became clear, indicating the formation of activated fullerenol. After completion of the reaction, the activated fullerenol was precipitated by adding diethyl ether to the reaction mixture. The resulting solid was washed repeatedly with diethyl ether, dichloromethane, and isopropyl alcohol. Successful product formation was confirmed by the presence of aromatic doublets at 6.9 and 8.1 ppm in proton NMR spectroscopy (Appendix C, Figure C. 1).

3.2.3 Synthesis of Fullerenol-Histidine-Serine (F-HS)

100 mg of crude activated fullerenol was dissolved in anhydrous DMF and sonicated under nitrogen for 30 minutes. To attach the amino acids, 152 mg of L-histidine was added to the reaction mixture first, followed by 108 mg of L-serine, both at room temperature. The resulting dark solution was stirred under nitrogen for 30 hours, with 1-hour sonication every 8 hours. A dark precipitate formed upon the addition of diethyl ether. The precipitate was washed twice with diethyl ether and 1-2 drops of methanol in dichloromethane. The final dark solid was isolated and dried under vacuum. The presence of amino acid-modified fullerenol species was confirmed by ^{1}H NMR.

The number of histidine and serine residues attached to fullerenol was determined by ^{1}H NMR using DMF as an internal standard. The integration of the DMF aldehyde proton peak was chosen as the reference and compared with the peaks corresponding to histidine and serine residues. Based on the comparison, the number of histidine and serine residues was calculated to be 4 each (Appendix D, Figure D. 1).

3.2.4 Synthesis of Fullerenol-Serine (F-S)

Activated fullerenol (60 mg, 0.030 mmol) was dissolved in 20 mL of anhydrous DMF and sonicated for 1 hour. L-Serine (0.13 g, 1.2 mmol) was then added to the solution, and the reaction mixture was stirred under N_2 atmosphere for

2 days. Sonication was applied twice daily for 1 hour. Upon completion of the reaction, diethyl ether was added to the mixture to precipitate the product. The precipitate was collected by centrifugation, then washed with dichloromethane containing a few drops of methanol, followed by diethyl ether. ^{1}H NMR spectroscopy was used for characterization; spectra are shown in Appendix E, Figure E. 1. and Appendix E, Figure E. 2.

3.2.5 Synthesis of Fullerenol-Serine-PEG$_5$ (F-S-PEG)

Activated fullerenol (75 mg, 0.038 mmol) was dissolved in 30 mL of anhydrous DMF and sonicated for 1 hour. L-Serine (79 mg, 0.75 mmol) was then added to the solution with the addition of triethyl amine (0.10 mL, 0.75 mmol) and m-PEG$_5$-NH$_2$ (0.40 mL, 1.5 mmol). The reaction mixture was stirred under a nitrogen atmosphere for 2 days. Sonication was applied twice daily for 1 hour. After completion of the reaction, diethyl ether was added to the mixture, and the precipitate was collected by centrifugation. The resulting residue was washed sequentially with dichloromethane containing a few drops of methanol, followed by diethyl ether. ^{1}H NMR spectroscopy was used for characterization; spectra are shown in Appendix F, Figure F. 1. and Appendix F, Figure F. 2.

3.2.6 Synthesis of Fullerenol-Serine-Dodecyl Amine (F-S-C12)

Activated fullerenol (75 mg, 0.038 mmol) was dissolved in 30 mL of anhydrous DMF and sonicated for 1 hour. L-Serine (79 mg, 0.75 mmol) and dodecyl amine (0.28 g, 1.5 mmol) were added to the solution. The reaction mixture was stirred under a nitrogen atmosphere for 2 days. Sonication was applied twice daily for 1 hour. After completion of the reaction, diethyl ether was added to the mixture, and the precipitate was collected by centrifugation. The resulting residue was first washed with dichloromethane containing a few drops of methanol, then with diethyl

ether. ^{1}H NMR spectroscopy was used for characterization; spectra are shown in Appendix G, Figure G. 1. and Appendix G, Figure G. 2.

3.3 Preparation of LC Emulsions

F-HS (M_W:2068 g/mol) enzyme mimics were prepared in 1 mL of phosphate-buffered saline (PBS) at concentrations ranging from 0.02 to 1 mg/mL, while F-S (M_W:1690 g/mol), F-S-PEG (M_W:1550 g/mol), and F-S-C12 (M_W:2180 g/mol) enzyme mimics were prepared in 1 mL of PBS at varying concentrations (0.05–0.2 mg/mL). F-HS, F-S, and F-S-PEG samples were vortexed for 1 minute at 3000 rpm, then they were sonicated for 15 minutes in an ultrasonic bath. On the other hand, F-S-C12 enzyme mimic samples were subjected to 60 min of sonication in an ultrasonic bath and 80 min of tip-sonication, with a 1-minute vortexing at 3000 rpm every 20 min. *para*-Nitrophenyl acetate (*p*NPA) and *para*-Nitrophenol (*p*NP) stock solutions at 100 mM were prepared in dimethyl sulfoxide (DMSO) and diluted to the desired concentrations for experiments. To prepare emulsions, 1 mL of aqueous phase samples containing enzyme mimics, *p*NPA, *p*NP, fullerenol, or their combinations were mixed with 3 µL of 5CB. It was then dispersed for 10 seconds at 3000 rpm using a vortex mixer.

3.4 Optical Characterizations of Emulsions

Optical characterizations of LC (5CB) droplet configurations were carried out using a polarized optical microscope (Olympus BX53, Tokyo, Japan) equipped with crossed linear polarizers and a 50x long working distance objective lens. 100 µL of each sample was used for the droplet analysis, and at least 60 droplets were examined for each data point. The average results and standard deviations were obtained based on at least three independent experiments. The number of independent experiments (n) for each dataset is stated along with the experimental results, and the results are shown as the mean ± standard deviation. The size

measurements of the droplets performed using captured images were analyzed with Fiji ImageJ, an open-source image analysis software (NIH).

3.5 Interfacial Tension Measurements

The DataPhysics OCA 200 contact angle system (DataPhysics Instruments, Filderstadt, Germany) was used for interfacial tension measurements. For the measurements, a 3.5 mL quartz cell was used, and experiments were carried out using 30 µL droplets of 5CB. Firstly, the quartz cell was filled with 2 mL of phosphate-buffered saline (PBS) solution and left to equilibrate for 30 min, with data collection at 15-minute intervals. Enzyme mimic solutions were prepared and subjected to vortexing, ultrasonication, and tip sonication as appropriate to enzyme type, then added to PBS to reach a concentration of 0.1–1 mg/mL. After the addition of the enzyme mimic and mixing in the quartz cell, interfacial tension data were taken immediately at 15-minute intervals until stabilization was ensured. For dilution experiments, enzyme mimics were prepared as described above, stabilized for 150 min, and then diluted with fresh PBS to the desired concentrations. Measurement started instantly, and data were collected for an hour at 10-minute intervals after the dilution. Mean interfacial tension values and their standard deviations were obtained from n independent experiments, at least three independent experiments, with each time point averaged from at least five consecutive measurements and reported as the mean ± standard deviation.

3.6 Kinetic Measurement Studies

For enzyme mimic kinetics investigation, an Agilent BioTek Epoch 2 Microplate Spectrophotometer with Gen6 software and 96-well plates were utilized. F-HS (0.2 mg/mL and 0.5 mg/mL), F-S, and F-S-PEG (0.2 mg/mL) samples in PBS were prepared by 1-minute vortex mixing at 3000 rpm, followed by 15 min sonication in an ultrasonic bath, and 15 min of tip sonication. F-S-C12 (0.2 mg/mL)

samples were subjected to three steps of processing, which consisted of 60 min of sonication in an ultrasonic bath and subsequent 80 min tip sonication, as well as vortexing at 3000 rpm for 1 minute every 20 min. The *p*NPA stock solution of 100 mM concentration was diluted to prepare solutions ranging from 0.4 mM to 4 mM, which were added to enzyme mimic solutions. The enzyme mimic solutions were prepared with and without the presence of 5CB droplets. The 5CB emulsions were prepared in PBS by vortex mixing at 3000 rpm for 1 minute, followed by 15 minutes of ultrasonic bath sonication and tip sonication for 15 minutes. Absorbance measurements at 410 nm were taken immediately after *p*NPA was added to the enzyme mimics in order to monitor the *p*NP reaction product. The experiments took place at room temperature, while absorbance readings were taken for at least 2 hours. An extinction coefficient of 11580.4 M^{-1} cm^{-1} was utilized to calculate *p*NP concentrations and the initial reaction rates of F-HS, and the data were fitted to the Michaelis-Menten model after removing background hydrolysis to determine kinetic parameters precisely. The experiments were conducted in three independent runs, and the results are presented as the mean value with standard deviation.

3.7 UV-Vis Spectrophotometric Measurements

UV absorbance measurements were performed on a Shimadzu UV-Vis Spectrophotometer, model UV-2550, equipped with software UVProbe 2.71. Spectra have been recorded from 230 nm to 500 nm at an interval of 0.05 nm. Measurement was carried out using 3.5 mL quartz cells. The sample volume for these measurements is 3.0 mL. Experiments were carried out with 0.2 mg/mL F-HS, combined with either 0.4 mM *p*NP and 0.2 mM *p*NPA or 0.1 mM *p*NP and 0.1 mM *p*NPA, as well as their individual components.

CHAPTER 4

RESULTS AND DISCUSSION

The study presented in this thesis has two main parts. In the first part, we characterized the response mechanism of liquid crystal (LC) droplets as a sensing platform for fullerene-based enzyme mimic-substrate interactions in bulk aqueous phase reactions. This part involved the LC droplet response characterization to individual components of our system of interest (*p*NPA and F-HS), characterization of LC droplet interfaces interacting with fullerene-based enzyme mimic, tracking enzyme mimic-substrate interactions through time-dependent LC droplet configuration frequencies, and the investigation of the origin of the LC droplet response. In the second part, the chemistries of fullerene-based enzyme mimics were systematically modified, and the responses of LC droplets to these enzyme mimics were examined. Their interfacial structuration and catalytic features, as well as enzyme mimic–substrate interactions monitored through LC droplet configurations, were analyzed to reveal the effects of these modifications on droplet response characteristics.

4.1 Elucidating the Response Characteristics of Liquid Crystal Droplet-Based Sensing of Aqueous Phase Reactions Catalyzed by Synthetic Enzyme Mimics (F-HS)

4.1.1 System Components and Observed LC Droplet Configurations

Our system of interest consists of three principal components: (*i*) the thermotropic room-temperature nematic liquid crystal (LC) 4-pentyl-4′-cyanobiphenyl (5CB), (*ii*) the fullerene-based enzyme mimics, fullerenol-histidine-serine (F-HS), and (*iii*) the substrate *p*-nitrophenyl acetate (*p*NPA) as shown in

Figure 4.1a. The F-HS enzyme mimic was synthesized by immobilizing histidine and serine amino acids to the fullerenol structure (details in the Experimental Section). With such structures, the enzyme mimics were shown to catalyze the hydrolysis of the ester groups significantly, where in most cases, *p*NPA is used as the ester-group containing model substrate.[30] As illustrated in Figure 4.1b, 5CB droplets were dispersed in PBS containing the F-HS enzyme mimic. After equilibration with F-HS, substrate (*p*NPA) was added to initiate hydrolysis, producing hydrolyzed substrate.

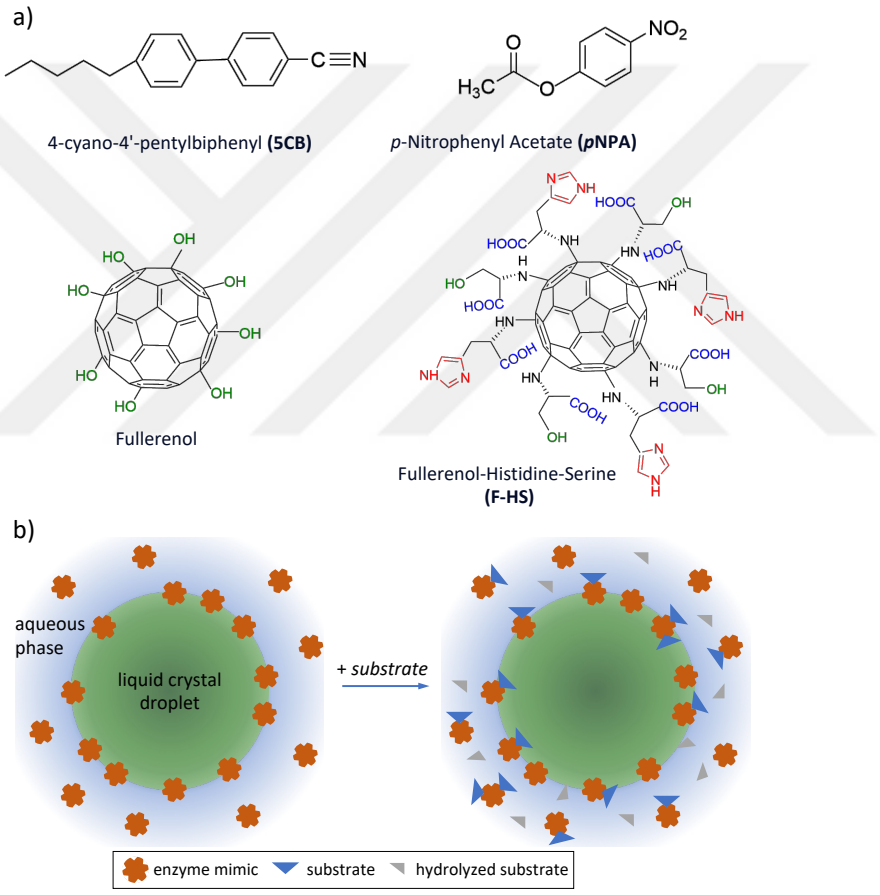

Figure 4.1. (a) Molecular structures of the chemicals used in this study (*For clarity, only a subset of the hydroxyl groups and amino acids on the fullerenol structures are depicted*.). (b) Schematic representation of the experimental system under investigation before and after substrate addition.

The dispersed 5CB droplets were in the 1 to 10 μm range of diameter, with a representative size distribution as shown in Figure 4.2a. This size range is determined as it has been shown previously that the competition between the anchoring energy and elasticity occurs within this size range to enhance the sensitivity of the droplets.[5,41]

The confinement of LCs in micrometer-sized droplets generates interfacial anchoring-dependent LC configurations, leading to unique optical signatures when observed under a simple crossed polarized microscope. In the experiments described in the first part of the thesis, we observed two distinct 5CB droplet configurations in the majority of the droplets: bipolar and preradial. When the LC orientation at the droplet interface is tangential (locally planar), the droplet exhibits two separated point defects located at the two opposite poles of the droplet and maintains the so-called "bipolar" droplet configuration, as the brightfield and polarized light microscopy images illustrated in Figure 4.2b. These two-point defects appear dark in a polarized light image. In regions where the LC orientation is uniform along the optical path and parallel to the polarizer or analyzer (of the crossed polarizers), the LC phase appears dark. In the rest of the droplet, the LC phase appears as bright birefringent colors. When the LC interfacial anchoring is tilted, the preradial configuration is maintained in a droplet, which possesses a single-point defect located at the interface of the droplet, thus resulting in a distinct optical appearance as shown in Figure 4.2b. Thus, polarized optical microscopy can be used to distinguish the interfacial orientation of the LCs *via* the configuration structures maintained in the emulsion droplets. Such droplet structures are common equilibrium configurations, and their formation mechanism, energetics, and optical signatures have previously been extensively investigated.[5,41] In this study, we dispersed the 5CB droplets in the aqueous phases where enzymatic hydrolysis of the model substrate *p*NPA occurs with F-HS and tracked their time-dependent configuration distributions.

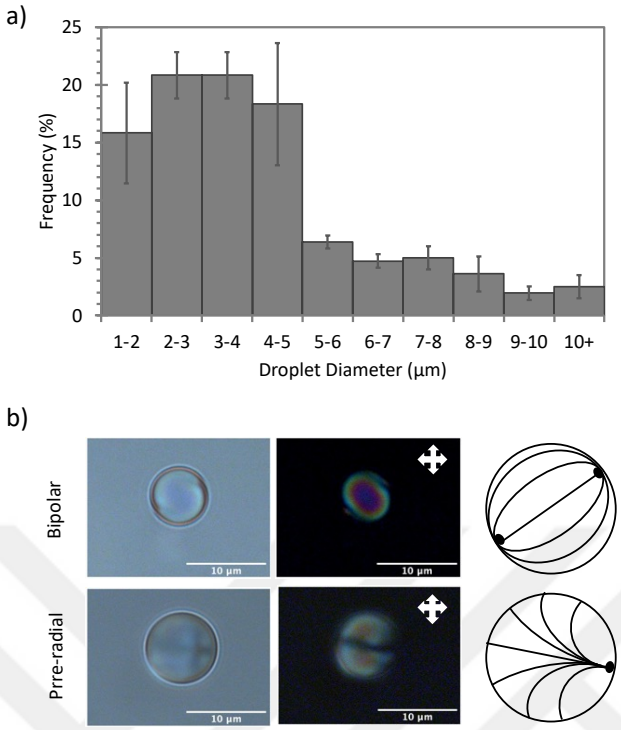

Figure 4.2. (a) Distribution of the size of the 5CB droplets in emulsions as determined from microscopy images (n=3). (b) The brightfield (left) and polarized light microscopy images (middle) of two 5CB droplets corresponding to the bipolar and preradial configurations, as illustrated (right).

4.1.2 Response of LC Droplets to Fullerene-Based Enzyme Mimic-Substrate Interactions

We first sought to explore how the interaction of the F-HS-equilibrated 5CB droplet interfaces with *p*NPA affects the time-dependent configuration frequency distribution of 5CB droplets. The F-HS solutions were initially prepared at a concentration of 1 mg/mL (details in the Experimental section), and 5CB was emulsified in it. As shown in Figure 4.3, "initial" data represents the configuration distribution of 5CB droplets collected in this F-HS solution, showing a preradial configuration distribution of 25.6 ± 1% (n=3). After the addition of 0.8 mM *p*NPA to the emulsion, time-dependent configuration measurements were performed, and

the initial data collected after *p*NPA addition is denoted as "0" in Figure 4.3. At this point, the preradial configuration frequency distribution was decreased to 13.9 ± 1% (n=3). We collected 5CB droplet configuration distributions at 20-minute intervals throughout 100 minutes. In the time-dependent configuration distributions, we observed that the preradial configuration gradually increased. It eventually returned to the configuration associated with the enzyme mimic alone, reaching a steady value of 25.0 ± 1.7% (n=3) for the preradial configuration, approximately 60 minutes after the addition of *p*NPA. We aimed to investigate the intriguing response of the 5CB droplets to the interaction between F-HS and *p*NPA in this complex system. To clarify the response characteristics, we first examined how the LC droplets individually responded to the substrate and the enzyme mimic.

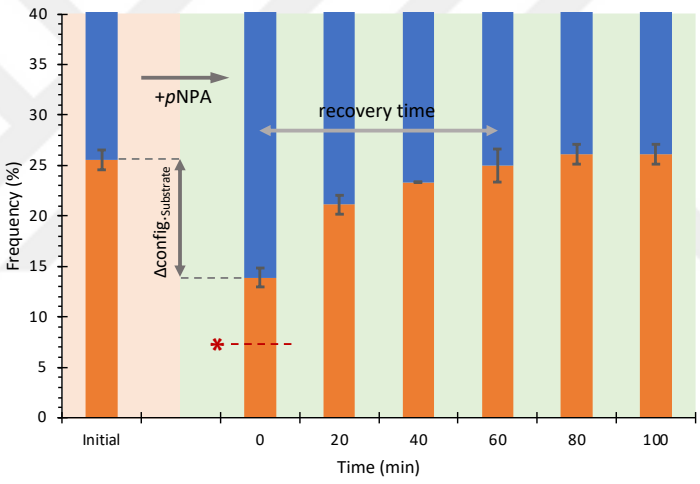

Figure 4.3. Configuration distribution of 5CB droplets dispersed in 1 mg/mL F-HS enzyme mimic, and the time-dependent changes in frequency monitored over 100 minutes following the addition of 0.8 mM *p*NPA. The data represent the averages and standard deviations from three independent experiments.

4.1.3 LC Droplet Response Characterization

4.1.3.1 Response to Substrate (*p*NPA)

We investigated the configurations of the 5CB droplets maintained in *p*NPA solutions. Figure 4.4a presents the droplet configuration frequencies maintained in the medium of PBS and PBS with 1 mM *p*NPA or 2 mM *p*NPA. The measurements were conducted immediately after dispersing 5CB droplets into the sample, as shown in the initial data, and after 1 hour and 2 hours of equilibration with 5CB droplets. The configuration frequency values showed no significant difference across the *p*NPA concentrations and PBS, indicating that *p*NPA did not induce a concentration- or time-dependent response. Similar to PBS alone (93.3 ± 1.9% (n=21)), *p*NPA led to a predominantly bipolar configuration, with 92.5 ± 2.4% (n=18) of the droplets exhibiting this configuration. Because the *p*NPA stock solution was prepared in DMSO, we conducted experiments identical to those in Figure 4.4a to examine the droplet response to DMSO, as shown in Figure 4.4b. These experiments used the same concentrations (1 mM and 2 mM) and time points (initial, 1 hour, and 2 hours) in PBS, with pure DMSO substituting the equivalent amount of *p*NPA. We confirmed that DMSO did not induce an ordering transition, resulting in a bipolar droplet configuration frequency of 92.7 ± 0.8% (n=18).

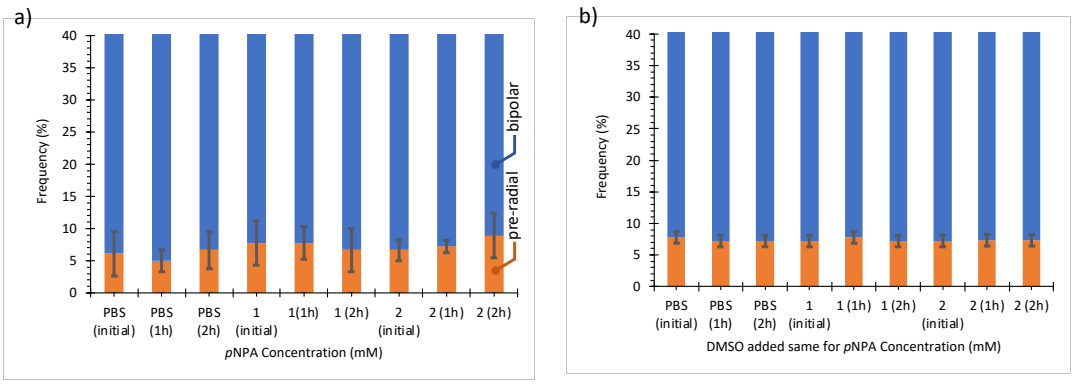

Figure 4.4. Configuration frequency distribution of 5CB droplets at initial, 1 hour, and 2 hours incubation times (n=3). (a) In PBS and in 1 mM and 2 mM *p*NPA

solutions. (b) In PBS and in PBS with DMSO equivalent to 1 mM and 2 mM *p*NPA concentrations.

4.1.3.2 Response to Fullerene-Based Enzyme Mimic (F-HS)

After investigating *p*NPA, we analyzed the 5CB droplet configuration distributions induced by the F-HS enzyme mimic. Figure 4.5a shows the time-dependent configuration frequencies maintained in the 5CB droplets in the presence of 1 mg/mL F-HS in PBS solution. The 0-hour data point in the figure represents the 5CB droplet configuration that was collected immediately after the addition of F-HS to the PBS-equilibrated 5CB droplets. The initially maintained 6.7 ± 1.9% (n=21) of preradial droplets in PBS solution was measured to be 25.6 ± 1% (n=3) within several seconds after 1 mg/mL F-HS was introduced into the solution, and the droplet configuration distribution remained time-invariant after. In addition to a 1 mg/mL F-HS response, Figure 4.5b displays configuration distributions obtained with 0.02, 0.06, 0.1, 0.2, 0.3, 0.4, and 0.5 mg/mL F-HS concentrations. As illustrated in Figure 4.5a, we defined the difference in the frequency of the preradial configuration maintained in PBS and in the F-HS solution as the Δconfig.$_{Enzyme}$. This difference was further measured as a function of F-HS concentration, with the results shown in Figure 4.5b. We observed that the Δconfig.$_{Enzyme}$ increased with F-HS concentration up to 0.5 mg/mL and did not change significantly at higher concentrations of F-HS (Figure 4.5c). This increase with concentration suggested that the enrichment of the droplet interfaces with F-HS as the bulk F-HS concentration was increased. Upon reaching 0.5 mg/mL F-HS, a configuration saturation was reached, indicating an interfacial saturation.

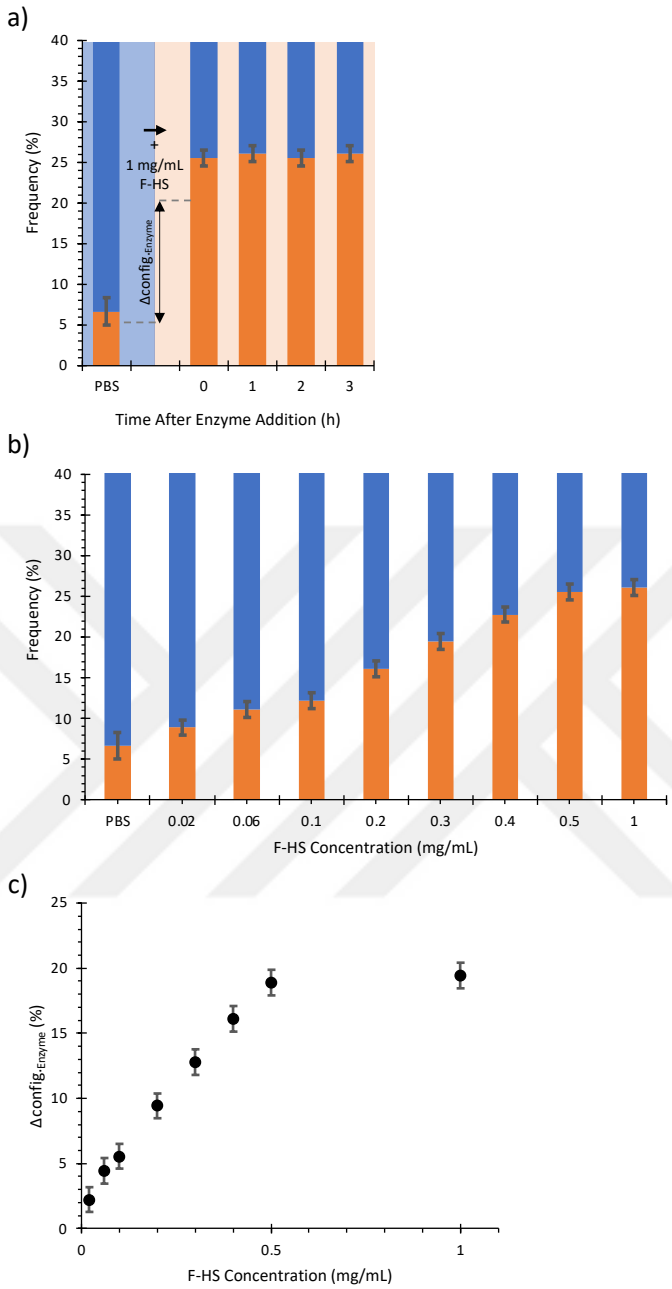

Figure 4.5. (a) Time-dependent configuration frequency distribution of 5CB droplets before and after the addition of 1 mg/mL F-HS (n=3). (b) Configuration frequency distributions of 5CB droplets in PBS and F-HS enzyme mimic concentrations ranging from 0.02–1 mg/mL (n=3). (c) Δconfig.$_{Enzyme}$ of 5CB droplets as a function of F-HS concentration in PBS, ranging from 0.02 mg/mL to 1 mg/mL F-HS (n=3).

4.1.4 LC Droplet Interfacial Characterization

To gain more insight into the F-HS-5CB interfacial interactions, we performed a dilution experiment to investigate the adsorption mechanism of F-HS at the 5CB droplet interface. We collected the configuration frequencies after dispersing 5CB droplets in 0.5 mg/mL F-HS solution. The sample was then diluted to a concentration of 0.1 mg/mL F-HS using a fresh PBS solution, and the droplet configuration distributions were collected. We measured the droplet configuration frequency of 24.9 ± 1.5% (n=3) preradial at 0.5 mg/mL F-HS in PBS to decrease to 12.8 ± 1% (n=3) preradial after dilution to 0.1 mg/mL F-HS, as presented in Figure 4.6. Such frequency maintained after dilution was statistically equivalent ($p>0.5$) to the configuration of 12.2 ± 1% (n=3) preradial configuration maintained in droplets directly equilibrated in 0.1 mg/mL F-HS solutions, as shown in Figure 4.5b. The observed alteration in droplet configuration indicates the reversible adsorption of F-HS at the interface.

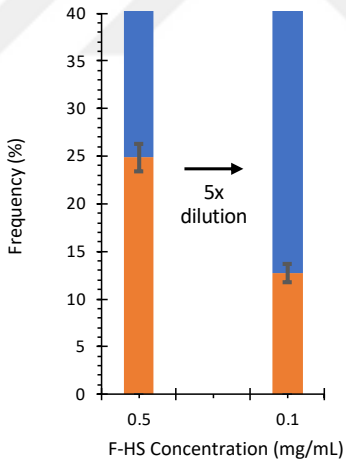

Figure 4.6. Configuration frequency distribution of 5CB droplets before and after dilution of F-HS solution from 0.5 mg/mL to 0.1 mg/mL F-HS concentration with fresh PBS solution (n=3).

To further characterize the 5CB droplet interfaces interacting with F-HS, we performed measurements on the interfacial tension of 5CB as a function of the bulk

concentrations of F-HS. We used the pendant drop method to measure the interfacial tension of 30 μL 5CB droplets in various samples. Initially, measurements were performed in 2 mL of PBS solution, allowing the system to stabilize for over 30 minutes, as shown in Figure 4.7a. The interfacial tension value at the LC-water (PBS) interface was determined to be 40.5 ± 0.3 mN/m (n=63) (Figure 4.7a). Subsequently, an F-HS solution was added to the PBS solution and thoroughly mixed. Interfacial tension measurements were taken for 2 hours following F-HS addition to ensure steady measurements for the interfacial tensions. The results revealed a progressive decrease in interfacial tension over the first ~30 minutes after the addition of F-HS, after which the values were stabilized. At higher concentrations of F-HS, the steady values of the interfacial tensions were decreased. For example, at an F-HS concentration of 0.1 mg/mL, the stabilized interfacial tension was 30.0 ± 0.8 mN/m (n=3), while at 0.5 mg/mL, it was decreased further to 23.7 ± 1 mN/m (n=3). For higher F-HS concentrations, the interfacial tension values were concentration-independent and measured as 23.7 ± 0.1 mN/m (n=3) and 23.8 ± 0.1 mN/m (n=3) for 0.8 mg/mL and 1 mg/mL of F-HS, respectively (Figure 4.7a). This measurement was correlated with the F-HS concentration-dependent measurements of the droplet configurations shown in Figure 4.5c, where the equilibrium droplet configuration was concentration-independent above 0.5 mg/mL F-HS. Thus, when we evaluated the results of the interfacial tension measurements with the droplet configuration results, we concluded that the interfacial adsorption of F-HS is reversible.

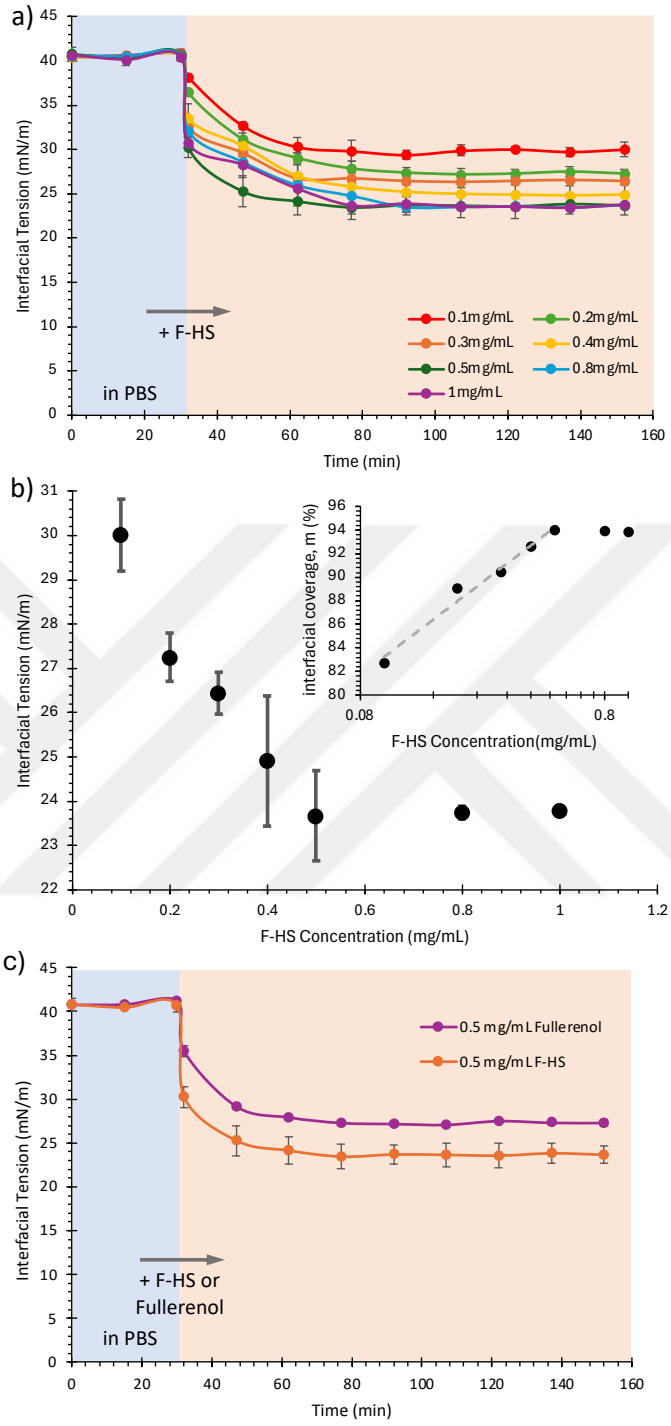

Figure 4.7. (a) Interfacial tension measurements of 5CB-aqueous interface obtained using the pendant drop technique, before and after F-HS addition, within the 0.1 mg/mL to 1 mg/mL F-HS concentration range. (b) Equilibrium interfacial tension

values as a function of F-HS concentration within the 0.1 mg/mL to 1 mg/mL range, along with calculated interfacial coverage (m, %) values based on the Gibbs monolayer model, assuming 94% maximum interfacial coverage, for the same enzyme mimic concentration range. (c) Interfacial tensions of the 5CB-aqueous interface determined using the pendant drop method before and after the addition of 0.5 mg/mL F-HS and 0.5 mg/mL fullerenol (n=3). The average interfacial tension values at the 5CB-aqueous interface and standard deviations were collected from three independent measurements. For each time point, the average was calculated from five individual measurements.

Equilibrium interfacial tension values obtained after a 2-hour stabilization period at F-HS concentrations ranging from 0.1 mg/mL to 1 mg/mL in PBS solution were used to construct the graph shown in Figure 4.7b. The results revealed that the reduction in interfacial tension persists up to a concentration of 0.5 mg/mL, beyond which further increases in F-HS concentration result in no significant changes. This observation is consistent with the saturation concentration identified in the droplet configuration experiments shown in Figure 4.5c, indicating that at 0.5 mg/mL, the enzyme mimic achieves a saturation interfacial coverage, corresponding to the formation of a nearly complete monolayer. The equilibrium interfacial tension measurements were further used to calculate the interfacial coverage (m) at the interface using Eqn. 1 below, based on the Gibbs monolayer adsorption model.[76]

$$\gamma - \gamma_0 = \Gamma_\infty RT\,[\ln(1-m)] - \frac{Km^2}{2} \quad \text{(Eqn. 1)}$$

In this model, R represents the gas constant (8.314 J/mol.K), T is the absolute temperature (K), m denotes the interfacial coverage ratio (relative to a complete monolayer), γ and γ_0 are the interfacial tensions at the 5CB-water interface in the presence and absence of F-HS (or surface-active substance), respectively. Γ_∞ represents the maximum interfacial concentration, and K is the cooperativity term. The interfacial tension in pure PBS solution was determined as γ_0 ~40.5 mN/m and used as a reference. The parameters were treated as constants in the model, with the cooperativity term (K) assumed to be 0. It was further assumed that at an enzyme

mimic concentration of 0.5 mg/mL, approximately 94% of the interface is covered, drawing an analogy to the interfacial adsorption characteristics of a common, water-soluble surfactant, for example, sodium dodecyl sulfate (SDS), which achieves 94% interfacial coverage at its critical micelle concentration.[77] Using these assumptions, a plot of m (interfacial coverage) vs F-HS concentration (mg/mL) was constructed, revealing a linear relationship comparable to that observed for SDS. These results indicate that F-HS exhibits a concentration-dependent adsorption at the interface, saturating at 0.5 mg/mL, and ~10% increase in the interfacial concentration results in a significant change in the droplet configuration distributions, as shown in Figure 4.5c (from 0.1 mg/mL to 1 mg/mL).

Moreover, using the same procedure described in Figure 4.7a, we conducted interfacial tension experiments with 0.5 mg/mL fullerenol, which has no conjugated amino acids. As represented in Figure 4.7c, results demonstrated that fullerenol was also surface-active, leading to a decrease in the interfacial tension. However, this decrease, though significant, was distinct from the reduction caused by F-HS at the same concentration, indicating the role of the chemical functionality in interfacial interactions.

4.1.5 Tracking Enzyme Mimic-Substrate Interactions with LC Droplets

We examined the time-dependent effects of the 1 mg/mL F-HS and 0.8 mM *p*NPA interaction on the configuration frequency distribution of 5CB droplets in Figure 4.3, where we found interesting results. Following the response and interfacial characterization studies of the 5CB-aqueous interface, we further investigated the interaction of the F-HS-equilibrated 5CB droplet interfaces with *p*NPA. Prior to beginning the in-depth experiments, we first defined the key parameters, which are displayed in Figure 4.3. As we explained, the "0 min" (t=0) data point, which displays a preradial configuration frequency of 13.9 ± 1% (n=3), is the droplet configuration data obtained just after adding *p*NPA to the F-HS solution. When compared with the preradial configuration frequency caused solely by *p*NPA

solutions, represented as 7.5 ± 2.4% (n=18) and marked with an asterisk (*) in Figure 4.3, the decrease at "t=0" did not fully reach this value. However, it showed a clear trend towards it, consistent with the configurations caused by the presence of the *p*NPA in the solution that are interacting with F-HS. We defined the difference in preradial configuration frequency maintained in the F-HS solution and the instance of the *p*NPA addition (referred to as "t=0") as the $\Delta config._{Substrate}$. Additionally, following the *p*NPA addition, the time required for the return to the "initial" configuration was defined as the "recovery time", which is indicated in Figure 4.3 for the example case of 0.8 mM *p*NPA. These parameters provided a consistent basis for interpreting the following analyses.

Besides the experiments with 0.8 mM *p*NPA, we performed experiments with varying [*p*NPA]/[F-HS] concentration ratios while keeping F-HS concentration constant at 1 mg/mL, following the experimental procedure in Figure 4.3. Figure 4.8 presents the results for *p*NPA concentrations of 0.05 mM (a), 0.1 mM (b), 0.2 mM (c), 0.4 mM (d), 0.5 mM (e), 1 mM (f), and 2 mM (g), monitored over 40, 40, 80, 80, 60, 105, and 120 minutes, respectively. Time-dependent droplet configuration data were collected starting at t=0 after adding *p*NPA to F-HS-equilibrated 5CB droplets. We did not use *p*NPA concentrations above 2 mM, as it dissolved within 5CB and induced a transition of 5CB droplets to the isotropic phase.

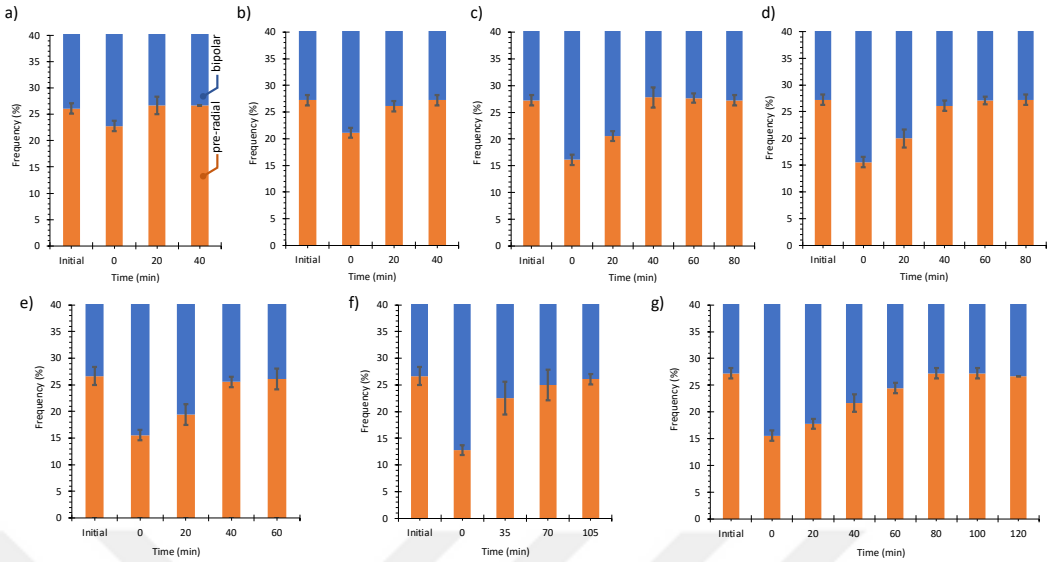

Figure 4.8. Configuration frequency distribution of 5CB droplets dispersed in 1 mg/mL F-HS, with time-dependent frequency changes monitored after addition of *p*NPA at varying concentrations (n=3). (a) 0.05 mM *p*NPA, monitored for 40 minutes. (b) 0.1 mM *p*NPA, monitored for 40 minutes. (c) 0.2 mM *p*NPA, monitored for 80 minutes. (d) 0.4 mM *p*NPA, monitored for 80 minutes. (e) 0.5 mM *p*NPA, monitored for 60 minutes. (f) 1 mM *p*NPA, monitored for 105 minutes. (g) 2 mM *p*NPA, monitored for 120 minutes.

Figure 4.9 presents the results of the Δconfig.$_{\text{Substrate}}$ and recovery time at different [*p*NPA]/[F-HS] ratios, based on the experimental data shown in Figure 4.8. Analysis of the data revealed that as the [*p*NPA]/[F-HS] ratio was increased, the Δconfig.$_{\text{Substrate}}$ also increased, reaching 11.9 ± 1.0% (n=18), at which it was stabilized. This increase was attributed to the higher concentration of *p*NPA, which promoted the bipolar configuration, leading to a more pronounced change in the Δconfig.$_{\text{Substrate}}$. The stabilization of the Δconfig.$_{\text{Substrate}}$ occurred once the [*p*NPA]/[F-HS] ratio reached ~0.4, indicating that the F-HS and *p*NPA had reached a state of saturation. The increase in the recovery time as a function of [*p*NPA]/[F-HS] even after 0.4 was also consistent with the presence of the increased amount of *p*NPA. In these experiments, we observed that the Δconfig.$_{\text{Substrate}}$ and recovery time were dependent on the [*p*NPA]/[F-HS] ratio.

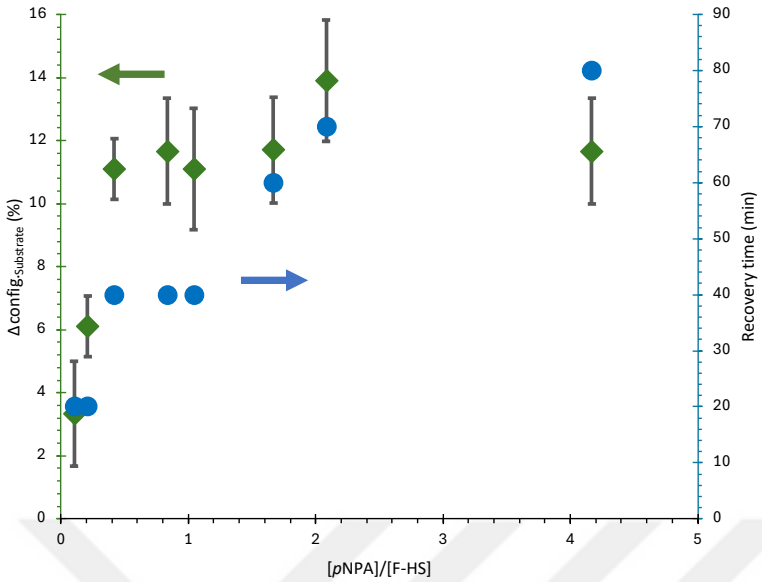

Figure 4.9. Δconfig.$_{\text{Substrate}}$ (%) (left, green) and recovery time (min) (right, blue) as functions of the molar ratio of *p*NPA to F-HS ([*p*NPA]/[F-HS]), with the F-HS concentration kept constant at 1 mg/mL. Data represent the mean values ± standard deviations from three independent measurements.

Since the *p*NPA stock solution was prepared in DMSO, we investigated whether DMSO influences the configuration frequency of 5CB droplets equilibrated with F-HS. We performed the experiments using 1 mg/mL (Figure 4.10a) and 0.5 mg/mL F-HS (Figure 4.10b) with an equivalent amount of DMSO as used to prepare 1 mM and 0.5 mM *p*NPA, respectively. Droplet configuration frequencies were monitored for 60 minutes at 20-minute intervals, with no time-dependent changes. These results confirmed that the interaction between F-HS and DMSO does not affect the configuration of 5CB droplets.

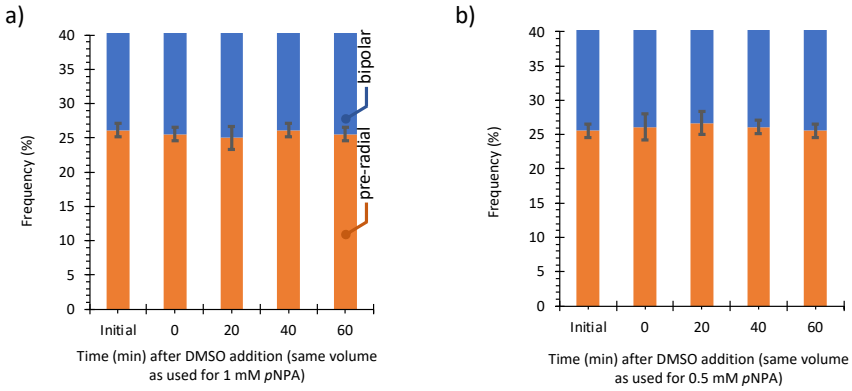

Figure 4.10. Time-dependent configuration distribution of 5CB droplets observed for 60 minutes in F-HS solutions containing DMSO at volumes corresponding to *p*NPA concentrations (n=3). (a) In 1 mg/mL F-HS with DMSO corresponding to the volume for 1 mM *p*NPA. (b) In 0.5 mg/mL F-HS with DMSO corresponding to the volume for 0.5 mM *p*NPA.

We performed a dilution experiment in the presence of both F-HS and *p*NPA to examine whether the reversible adsorption persists in the presence of *p*NPA. Figure 4.11a presents the droplet configuration frequency results for 0.5 mg/mL F-HS and 0.5 mM *p*NPA interactions, where the preradial configuration frequency decreased from 25.6 ± 1% (n=3) at the initial data to 9.4 ± 1% at t=0, with a recovery time of 60 minutes. Similarly, for 0.1 mg/mL F-HS with 0.1 mM *p*NPA, the preradial configuration frequency decreased from 12.2 ± 1% at the initial data to 10.6 ± 1% at t=0, with a recovery time of 20 minutes (Figure 4.11b). A dilution experiment starting from 0.5 mg/mL F-HS and 0.5 mM *p*NPA, diluted to 0.1 mg/mL F-HS and 0.1 mM *p*NPA, yielded configuration changes statistically identical to those of the directly prepared 0.1 mg/mL sample (Figure 4.11c). These results confirm that reversible adsorption also takes place in the presence of *p*NPA.

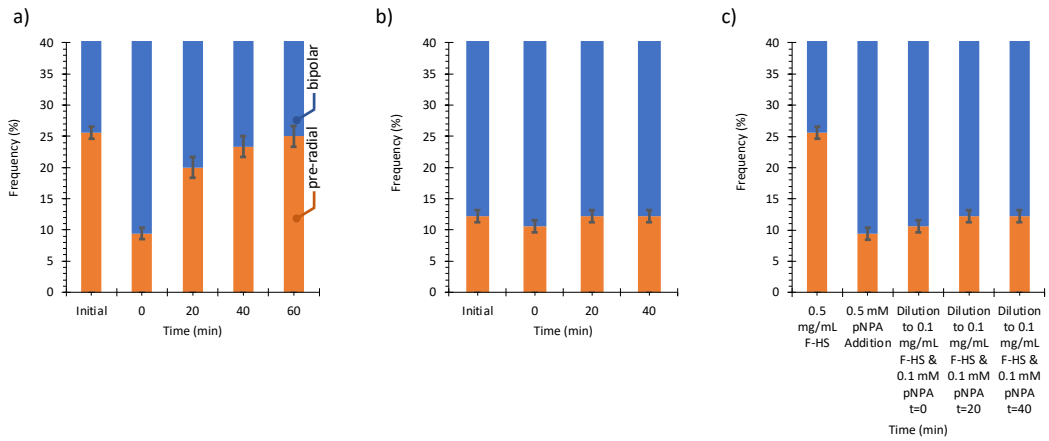

Figure 4.11. Configuration frequency distributions of 5CB droplets in F-HS solutions containing *p*NPA, measured over fixed time intervals (n=3). (a) In 0.5 mg/mL F-HS with 0.5 mM *p*NPA, measured over 60 minutes. (b) In 0.1 mg/mL F-HS with 0.1 mM *p*NPA, measured over 40 minutes. (c) In 0.5 mg/mL F-HS with 0.5 mM *p*NPA, diluted to 0.1 mg/mL F-HS and 0.1 mM *p*NPA, with configuration frequency measured for 40 minutes after dilution.

In addition to experiments with 1 mg/mL F-HS and *p*NPA concentrations ranging from 0.05 to 2 mM, as illustrated in Figure 4.8, we performed droplet configuration frequency experiments with 0.5 mg/mL F-HS over the same *p*NPA concentration range. The results for 0.5 mg/mL F-HS with *p*NPA concentrations of 0.05 mM (a), 0.1 mM (b), 0.2 mM (c), 0.4 mM (d), 0.5 mM (e), 0.8 mM (f), 1 mM (g), and 2 mM (h) are presented in Figure 4.12. Droplet configuration data were collected with 20-minute intervals over 40, 60, 80, 80, 60, 100, 120, and 160 minutes, respectively, after *p*NPA addition.

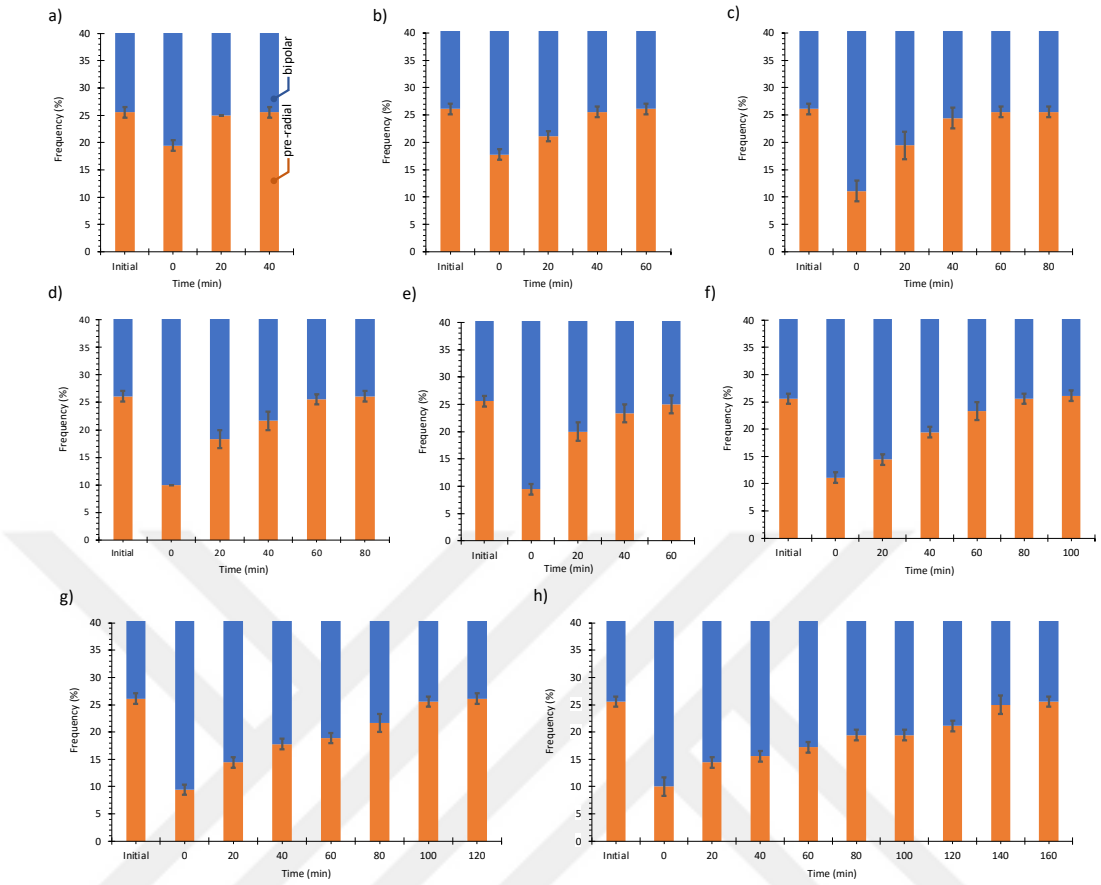

Figure 4.12. Configuration distribution of 5CB droplets dispersed in 0.5 mg/mL F-HS enzyme mimic, with time-dependent frequency changes monitored after the addition of pNPA at different concentrations (n=3). (a) 0.05 mM pNPA, monitored over 40 minutes. (b) 0.1 mM *p*NPA, monitored over 60 minutes. (c) 0.2 mM *p*NPA, monitored over 80 minutes. (d) 0.4 mM *p*NPA, monitored over 80 minutes. (e) 0.5 mM *p*NPA, monitored over 60 minutes. (f) 0.8 mM *p*NPA, monitored over 100 minutes. (g) 1 mM *p*NPA, monitored over 120 minutes. (h) 2 mM *p*NPA, monitored over 160 minutes.

Based on the experimental data shown in Figure 4.12, the Δconfig.$_{Substrate}$ and recovery times were calculated and are presented in Figure 4.13. Analysis of the results revealed that as the [*p*NPA]/[F-HS] ratio was increased, Δconfig.$_{Substrate}$ also increased, reaching stabilization at 15.7 ± 0.8 (n=18). Compared to experiments performed with 1 mg/mL F-HS, Δconfig.$_{Substrate}$ stabilized at a higher value of

[*p*NPA]/[F-HS] ratio with 0.5 mg/mL F-HS (~0.8). As previously established, the 5CB droplet interface reaches a saturation at 0.5 mg/mL F-HS, with the F-HS concentration at the interface remaining constant at higher bulk F-HS concentrations (Figure 4.7a). However, due to the reversible adsorption observed in our system, the interface remains highly sensitive to changes in the bulk environment. Although the interface is saturated at 0.5 mg/mL F-HS, the bulk contains less F-HS compared to 1 mg/mL F-HS, resulting in a higher [*p*NPA]/[F-HS] ratio in the bulk. This may lead to a more pronounced effect of *p*NPA at the 5CB interface, causing a higher value of $\Delta config._{Substrate}$. In contrast, at 1 mg/mL F-HS, the higher bulk enzyme concentration enhances particle-particle interactions, reducing the interaction with the interface and consequently yielding a lower $\Delta config._{Substrate}$. These factors collectively account for the consistent differences in $\Delta config._{Substrate}$ across the two enzyme mimic concentrations. Furthermore, recovery times in experiments with 0.5 mg/mL F-HS were longer than those with 1 mg/mL F-HS, indicating that faster bulk interactions at higher enzyme concentrations influence recovery times. These observations support the role of bulk enzyme dynamics in modulating interface responsiveness. Additionally, at 0.5 mg/mL F-HS, the [*p*NPA]/[F-HS] ratio at which stabilization occurs was observed to be 0.83, approximately doubling the ratio required for stabilization compared to 1 mg/mL F-HS (0.42). This increase is consistent with the halved enzyme mimic concentration, as maintaining the same *p*NPA concentration required for interface saturation necessitates a two-fold higher [*p*NPA]/[F-HS] ratio, further supporting the saturation of the 5CB interface at 0.5 mg/mL while highlighting the critical influence of bulk enzyme dynamics on the interface's responsiveness to *p*NPA.

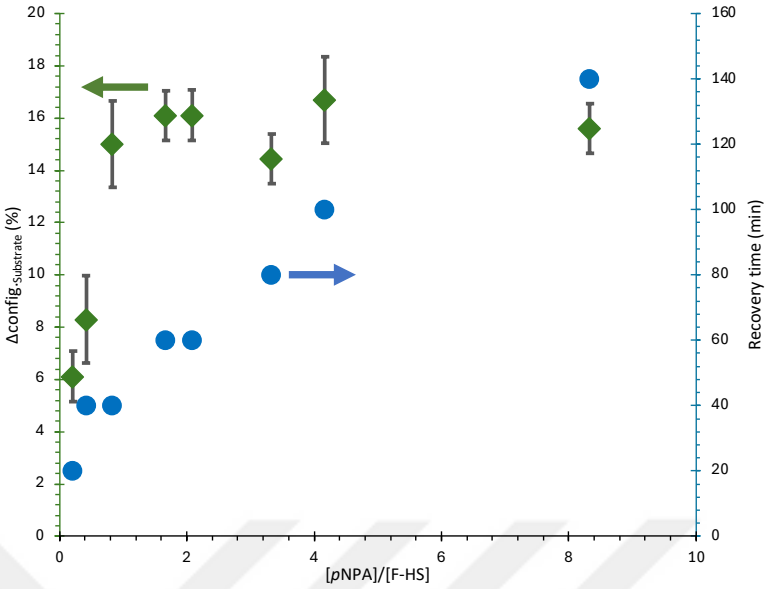

Figure 4.13. Δconfig.$_{\text{Substrate}}$ (%) (left, green) and recovery time (min) (right, blue) as a function of the molar ratio of *p*NPA to F-HS ([*p*NPA]/[F-HS]), with F-HS concentration set at 0.5 mg/mL. Results are mean values with standard deviations from three independent experiments.

4.1.6 Investigation of the Origin of LC Droplet Response

Next, we sought to understand the origin of the observed response by performing kinetic measurements of the hydrolysis of *p*NPA with F-HS using UV−Vis spectroscopy. These measurements were conducted with F-HS at a concentration of 0.5 mg/mL and *p*NPA concentrations ranging from 0.4 mM to 4 mM. To assess the effect of 5CB on the reaction kinetics, these experiments were conducted both in the presence and the absence of 5CB droplets in the medium. Immediately after mixing of F-HS and *p*NPA, kinetic measurements were initiated by monitoring the absorbance of the reaction product, *p*-nitrophenol (*p*NP), at 410 nm. Figure 4.14 shows the time-dependent absorbance values obtained for 0.5 mM *p*NPA in the presence of 0.5 mg/mL F-HS. Additionally, the self-hydrolysis of 0.5 mM *p*NPA solution is also reported in the figure. For each sample, the concentration

of *p*-nitrophenol (*p*NP) was calculated over a 2-hour period based on the absorbance data. The data shown in blue represent the corresponding *p*NP concentration values. Solid lines in Figure 4.14 represent samples containing 0.3% vol 5CB dispersed via tip sonication to maximize the 5CB-aqueous interface. Despite the increasing interfacial area, absorbance values and corresponding *p*NP concentrations in both the presence (solid lines) and absence (dashed lines) of 5CB droplets were indistinguishable, and both displayed a linear increase throughout the 2-hour observation period. This linear trend suggests that the reaction remained in the initial phase for the entire 2-hour investigation period.

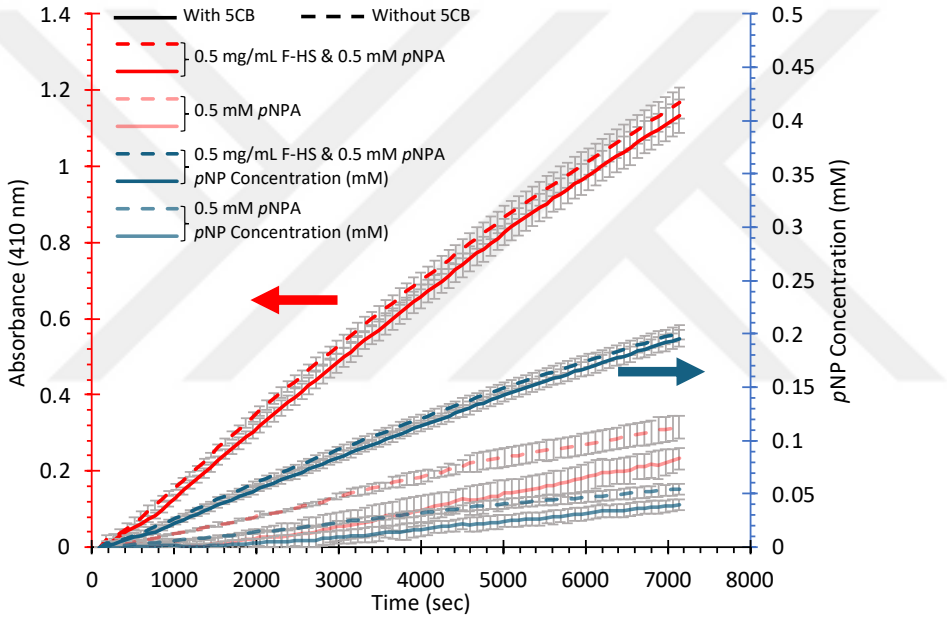

Figure 4.14. Time-dependent absorbance measurements and *p*NP Concentrations (mM) of 0.5 mg/mL F-HS with 0.5 mM *p*NPA, as well as the self-hydrolysis of 0.5 mM *p*NPA measured at wavelength of 410 nm, in the presence and absence of 5CB. The solid lines show the data with the presence of 5CB droplets, whereas the dashed lines show the data without the presence of 5CB droplets. The self-hydrolysis of 0.5 mM *p*NPA is represented with muted colors in the graph. The absorbance data is shown in the left axis, and the *p*NP concentration data is shown in the right axis.

Extending the analysis beyond the 0.5 mM *p*NPA case in Figure 4.14, we investigated the kinetics of 0.5 mg/mL F-HS with *p*NPA concentrations of 0.4 mM (a), 0.8 mM (b), 1.5 mM (c), 2.5 mM (d), and 4 mM (e), as shown in Figure 4.15. The time-dependent absorbance and associated *p*NP concentrations (mM) for these interactions were identical in the presence and absence of 5CB. The rate of absorbance increase was higher for the interaction between F-HS and higher *p*NPA concentrations compared to lower *p*NPA concentrations (Figure 4.15). Furthermore, the self-hydrolysis rates of *p*NPA at various concentrations (0.4 mM, 0.5 mM, 0.8 mM, 1.5 mM, 2.5 mM, and 4 mM) were slower than the rates observed in the presence of F-HS, with higher *p*NPA concentrations exhibiting faster self-hydrolysis rates than lower concentrations. As presented in Figure 4.12d–f, the recovery times for the 5CB droplet configurations in the presence of 0.5 mg/mL F-HS and 0.4 mM, 0.5 mM, and 0.8 mM *p*NPA were between 60 and 80 minutes. As shown in Figures 4.14, 4.15a, and 4.15b, no deviations from the linear increase in absorbance were observed within this time range. Even at the longest recovery times observed in measurements of the 5CB droplet responses, the absorbance continued to increase at a constant rate, indicating no measurable change in the hydrolysis rates. Although we initially considered that recovery times might be related to a response upon a change in the hydrolysis kinetics, the data indicate that these time scales do not correlate with the kinetics of the enzymatic hydrolysis of *p*NPA.

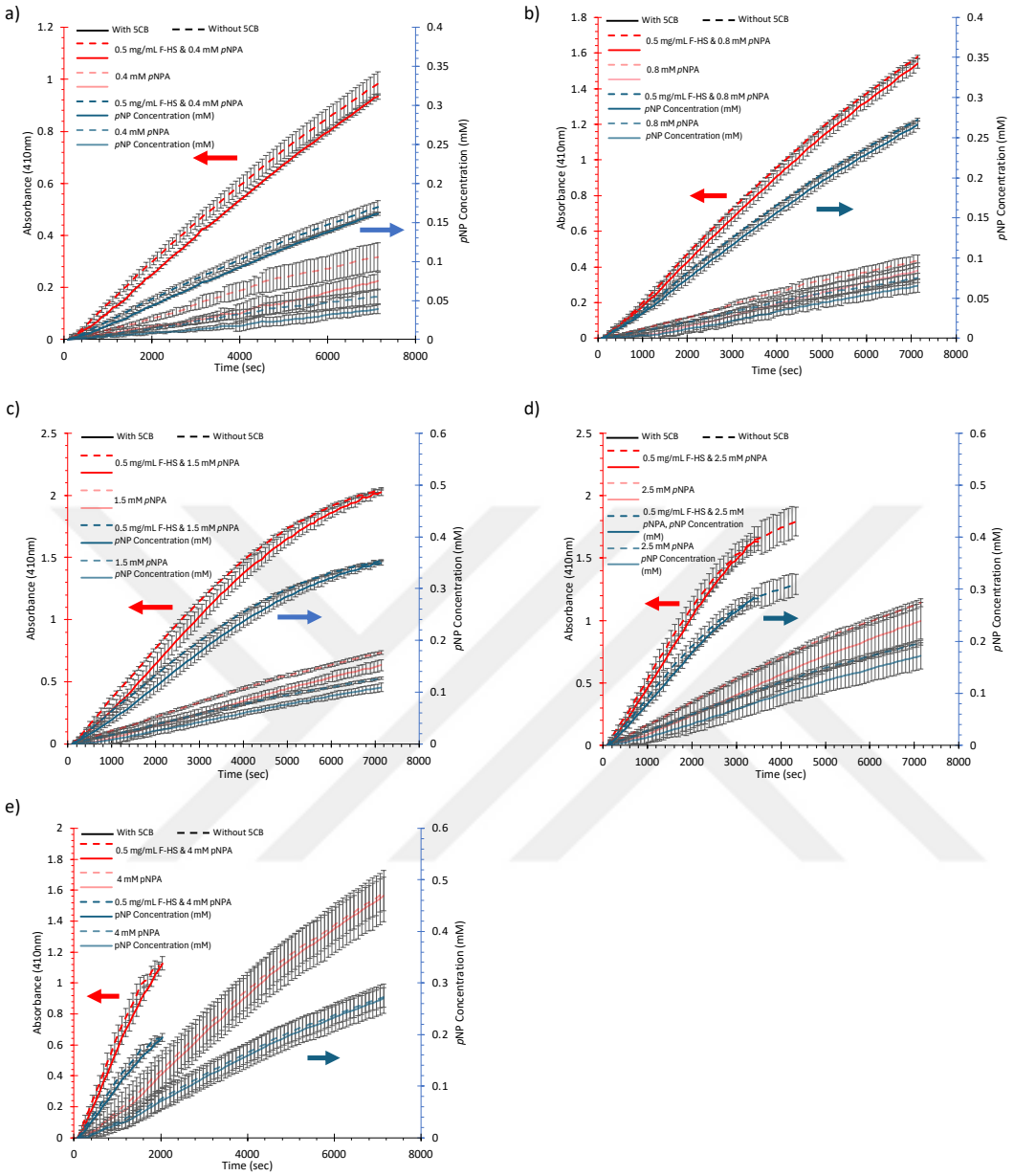

Figure 4.15. Time-dependent absorbance data collected at 410 nm and corresponding *p*NP concentration (mM) for 0.5 mg/mL F-HS, with varying concentrations of *p*NPA, as well as their self-hydrolysis (muted colors), both in the presence (solid lines) and absence of 5CB (dashed lines) (n=3). (a) 0.4 mM *p*NPA. (b) 0.8 mM *p*NPA. (c) 1.5 mM *p*NPA. (d) 2.5 mM *p*NPA. (e) 4 mM *p*NPA.

In addition to the hydrolysis kinetics measurements, the initial rate values as a function of *p*NPA concentration were calculated using time-dependent absorbance

data obtained with 0.5 mg/mL F-HS and *p*NPA concentrations ranging from 0.4 mM to 4 mM, and the results are shown in Figure 4.16. The kinetics followed the Michaelis−Menten equation, and the presence or absence of 5CB had no measurable effect on the kinetics. The enzyme mimic-substrate ratio remained the same both with and without 5CB, indicating that the presence of 5CB did not alter the reaction, and the reaction proceeded in the same way regardless of its presence. The calculated kinetic parameters, including V_{max} (M/s), K_M (mM), and k_{cat}/K_M ($M^{-1}s^{-1}$), are presented in Table 1, demonstrating significant hydrolytic activity.

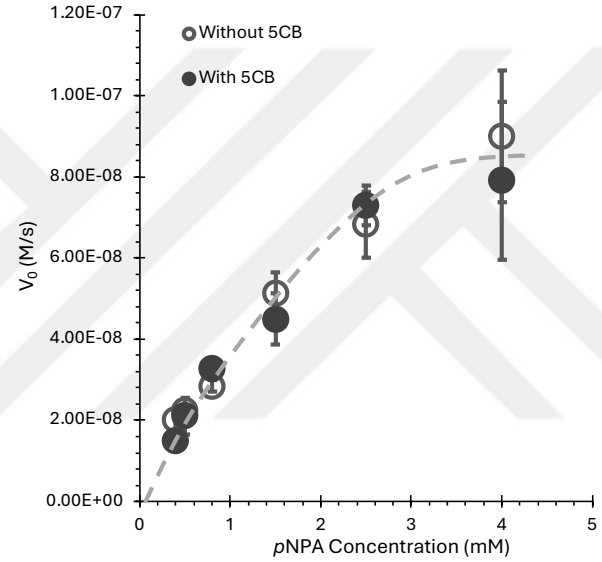

Figure 4.16. Initial rate values as a function of substrate concentration for the interaction of 0.5 mg/mL F-HS with 0.4 – 4 mM *p*NPA, in the presence and the absence of 5CB.

Table 1. Michaelis-Menten Parameters Obtained in the Presence and Absence of 5CB droplets

Sample Types	V_{max} (M/s) (x10^{-8})	K_M (mM)	k_{cat}/K_M ($M^{-1}s^{-1}$)
Without 5CB	12.9 ± 2.6	1.76 ± 0.21	0.30 ± 0.03
With 5CB	12.0 ± 2.3	1.73 ± 0.15	0.28 ± 0.03

Since the kinetics measurements of the substrate hydrolysis did not provide significant insights to the source of the 5CB droplet responses, we designed additional experiments to understand the origin of the observed response. In the result shown in Figure 4.17a, the interaction between 1 mg/mL F-HS and 0.8 mM *p*NPA was carried out differently from the standard procedure. Initially, the F-HS-*p*NPA mixture was prepared in PBS solutions, and immediately afterward, 5CB droplets were dispersed into the mixture. The configuration distribution measurements of the 5CB droplets were initiated immediately. The data represented by "time = 0" in the graph corresponds to the analysis collected immediately after the introduction of the 5CB droplets into the solution. Data were collected every 20 minutes for a total of 100 minutes, similar to the duration used in Figure 4.3. For each dataset, at least 60 droplet analyses were performed. The results are presented as the average and standard deviation from three independent experiments. At the time = 0 data point, the preradial configuration frequency was 13.3 ± 1.7% (n=3), while at the 60-minute data point, which corresponds to the recovery time, the pre-radial configuration frequency was 25.6 ± 1% (n=3). When compared to the results shown in Figure 4.3, the obtained 5CB configuration frequency distribution was statistically equivalent for each time point ($p>0.5$). These results show that the addition of *p*NPA while 5CB was dispersed within the F-HS solutions, or the addition of 5CB after forming the mixture of F-HS and *p*NPA in PBS, did not cause measurable changes in the obtained results.

Figure 4.17b presents the results of the 5CB configuration frequency distribution, where the “initial” data represents the data collected after 5CB droplets were dispersed in 0.5 mM *p*NPA, and the time point at “t=0” corresponds to the data collected after immediate addition of 0.5 mg/mL F-HS to the solution. In the usual procedure with these compositions of F-HS and *p*NPA, the initial data correspond to F-HS, with a preradial configuration frequency of 25.6 ± 1% (n=3). Following the addition of 0.5 mM *p*NPA, the preradial configuration frequency at t = 0 (9.4 ± 1% (n=3)) increased to 25.0 ± 1.7% (n=3) after a recovery period of 60 minutes (Figure 4.12e). In the experiment shown in Figure 4.17b, where the initial data included 0.5

mM *p*NPA, the preradial configuration frequency was 7.2 ± 1% (n=3), consistent with the results shown in Figure 4.4a. Upon the addition of F-HS, preradial configuration frequency at t = 0 was increased to 10.0 ± 0% (n=3) and reached to 25.0 ± 1.7% (n=3) after a 60 min recovery period. These results demonstrate that the order of addition, whether *p*NPA is added to the F-HS equilibrated-droplets or vice versa, did not result in statistically significant differences, and no measurable changes were observed in the measurements.

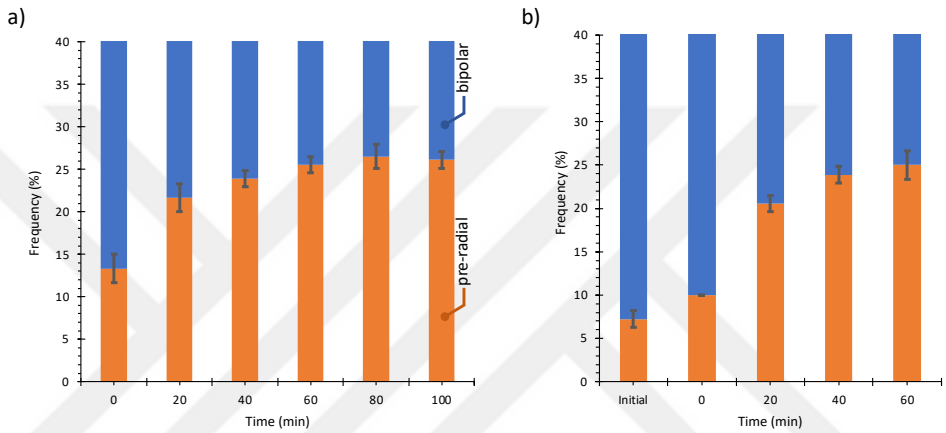

Figure 4.17. (a) Time-dependent configuration frequency distribution was obtained immediately after preparing the F-HS-*p*NPA mixture (1 mg/mL F-HS enzyme mimic with 0.8 mM *p*NPA), followed by the immediate dispersion of 5CB droplets into the mixture for analysis. (b) Configuration frequency distribution analysis was obtained using 0.5 mg/mL F-HS and 0.5 mM *p*NPA, where the F-HS was added to 5CB emulsions that were initially equilibrated in *p*NPA solutions.

Next, we conducted an additional experiment to investigate the origin of the observed response by introducing 5CB into the F-HS mixture at different time points and immediately collecting the response. The results are presented in Figure 4.18. Figure 4.18-*i* represents the immediate dispersion of 5CB into a mixture of 0.5 mg/mL F-HS and 0.5 mM *p*NPA, with the 5CB droplet configuration monitored over 60 minutes. The time-dependent configuration frequency distribution obtained is statistically indistinguishable ($p > 0.5$) from the results of the standard procedure, as

shown in Figure 4.12e. Figure 4.18-*ii* presents the experiment conducted at the same F-HS and *p*NPA concentrations; however, in this case, 5CB was dispersed into the mixture 20 minutes after the mixing of F-HS and *p*NPA solutions. Data collection began immediately and continued for 60 minutes. The preradial configuration frequency was found to be 20.0 ± 1.7% (n=3) at 20 minutes and increased to 25.0 ± 1.7% (n=3) at 60 minutes, which is statistically equivalent to the results presented in Figure 4.12e and Figure 4.18-*i*. Similarly, Figure 4.18-*iii* and *iv* correspond to the experiments where 5CB was introduced at 40 and 80 min after the mixing of F-HS and *p*NPA solutions, respectively. The preradial configuration values for 40 and 60 minutes were 23.3 ± 1.7% (n=3) and 25.0 ± 1.7% (n=3), respectively, which were statistically equivalent to those in Figure 4.12e and Figure 4.18-*i* at the same time points. In the experiments where 5CB was introduced at t=80 min, the obtained values remained time-invariant at 25.0 ± 1.7% (n=3), matching the preradial configuration frequency induced solely by F-HS.

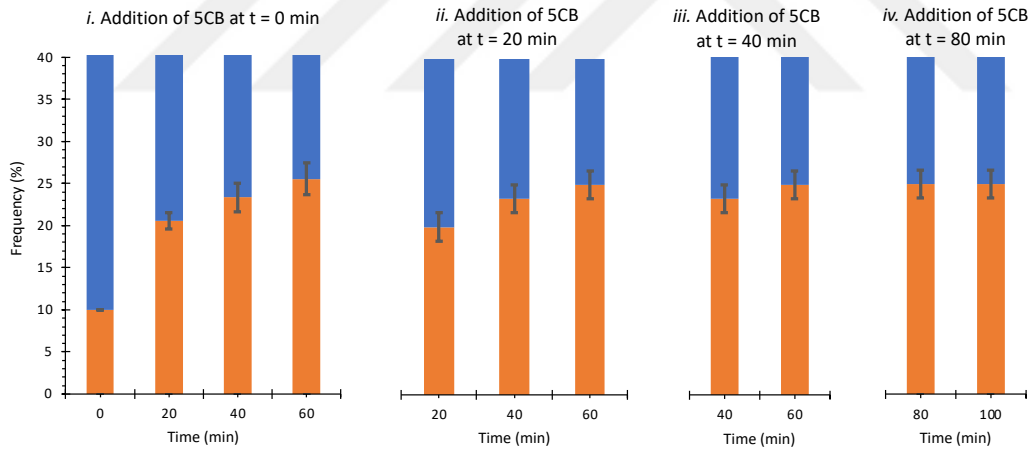

Figure 4.18. Time-dependent configuration distributions of 5CB droplets upon introducing 5CB into a mixture of 0.5 mg/mL F-HS and 0.5 mM *p*NPA at different time points indicated on the graphs.

We elaborate the major indicatives of the additional response measurements shown in Figures 4.14 - 4.18. Figures 4.14 – 4.16 demonstrated that the observed

response is independent of the kinetics of the *p*NPA hydrolysis. When 5CB was dispersed in *p*NPA and then F-HS solution was immediately introduced, as shown in Figure 4.17b, or when the F-HS-*p*NPA mixtures were prepared initially and droplet configuration distributions were collected after addition of the 5CB droplets in these mixtures (either immediately, as in Figure 4.17a, or after an incubation period), as in Figure 4.18, the results remained consistent at corresponding time points as following the original experimental procedure (Figure 4.12e). These measurements indicate three major outcomes. First, the hydrolysis kinetics were independent of the presence of 5CB droplets in the reaction medium. Second, the time scales of the droplet responses did not correlate with a measurable change in the kinetics or the substrate concentrations. Third, 5CB droplets provide an instantaneous measurement of the reaction occurring homogenously within the aqueous medium. We then interpret the characteristics of the droplet responses to the capturing of the complexation mechanism and reaction between the *p*NPA and F-HS in the aqueous medium.

To investigate the origin of recovery times, we examined the effect of the presence of the hydrolysis product, *p*NP, in the emulsion system. Figure 4.19a shows the results of the interaction between 0.2 mg/mL F-HS and 0.2 mM *p*NPA, performed using our usual procedure that revealed a 11.1 ± 1% (n=3) preradial configuration at t = 0 and a recovery time of 40 mins. In the experiment depicted in Figure 4.19b, the initial data reflect the droplet configuration distribution in the presence of 0.2 mg/mL F-HS. Subsequently, 0.2 mM *p*NPA was added to the system, and after recording the resulting configuration distribution, an excess of *p*NP (0.4 mM) was introduced to assess its impact. We observed that, the configurations were recovered almost instantaneously following *p*NP addition, revealing a recovery time of ~0 min. This suggests that the presence of *p*NP is influencing the recovery of the droplet configurations after the addition of *p*NPA.

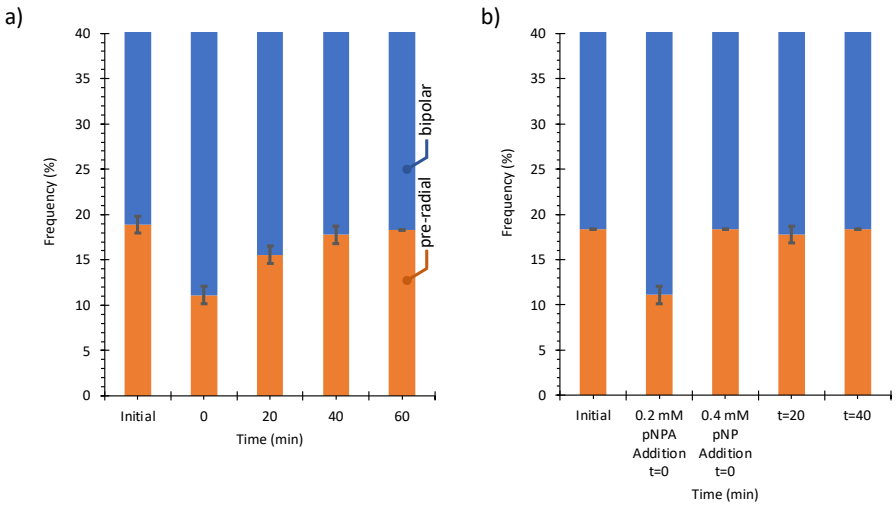

Figure 4.19. (a) Configuration distribution of 5CB droplets dispersed in 0.2 mg/mL F-HS and the time-dependent changes in configuration frequency over 60 minutes following the addition of 0.2 mM *p*NPA. (b) Configuration distribution of 5CB droplets after sequential addition of 0.2 mM *p*NPA and subsequently 0.4 mM *p*NP to 0.2 mg/mL F-HS.

To further explore the effect of *p*NP on the recovery of the droplet configurations, we reversed the order of addition in the experiment shown in Figure 4.20. In the experiments, *p*NP was added to the droplets in F-HS solution first, followed by the addition of *p*NPA. As seen in Figure 4.20a, *p*NPA was introduced at t = 60 min after *p*NP addition, but no configuration change was observed. In Figure 4.20b, we also performed a similar experiment where *p*NPA was added immediately after *p*NP addition that did not reveal a configuration change in droplets, indicating that the response is regardless of the waiting period.

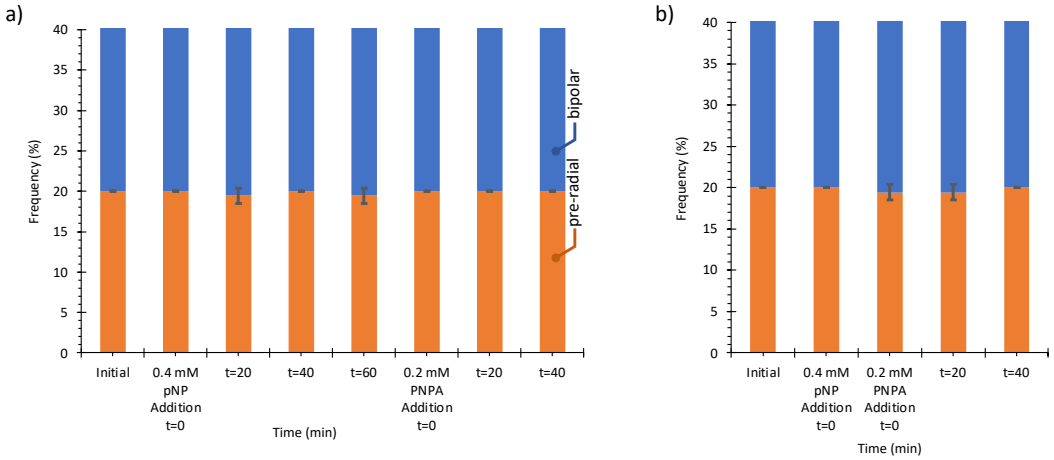

Figure 4.20. Configuration distribution of 5CB droplets after the addition of 0.4 mM *p*NP to 0.2 mg/mL F-HS, followed by 0.2 mM *p*NPA added (a) after a 60 min delay, or (b) immediately.

Additionally, neither 0.4 mM *p*NP alone nor a combination of 0.4 mM *p*NP and 0.2 mM *p*NPA altered the droplet configuration distributions (Figure 4.21a, b). UV spectroscopy experiments at these concentrations further revealed that the spectra of 0.4 mM *p*NP and 0.2 mM *p*NPA, whether measured separately and added or measured from their mixtures, were identical. It supports the absence of significant interactions between *p*NPA and *p*NP. Additionally, when 0.4 mM *p*NP, 0.2 mM *p*NPA, and 0.2 mg/mL F-HS were measured together or separately and their spectra summed, the resulting spectra were the same. It supports no significant interactions between *p*NPA, *p*NP, and the F-HS beyond the expected reaction. Furthermore, experiments conducted with 0.2 mg/mL F-HS, 0.1 mM *p*NPA, and 0.1 mM *p*NP yielded similar results, with no interactions observed between *p*NPA and *p*NP, or between *p*NPA, *p*NP, and F-HS, as the spectra obtained from individual and combined measurements were identical (Figure 4.21c, d).

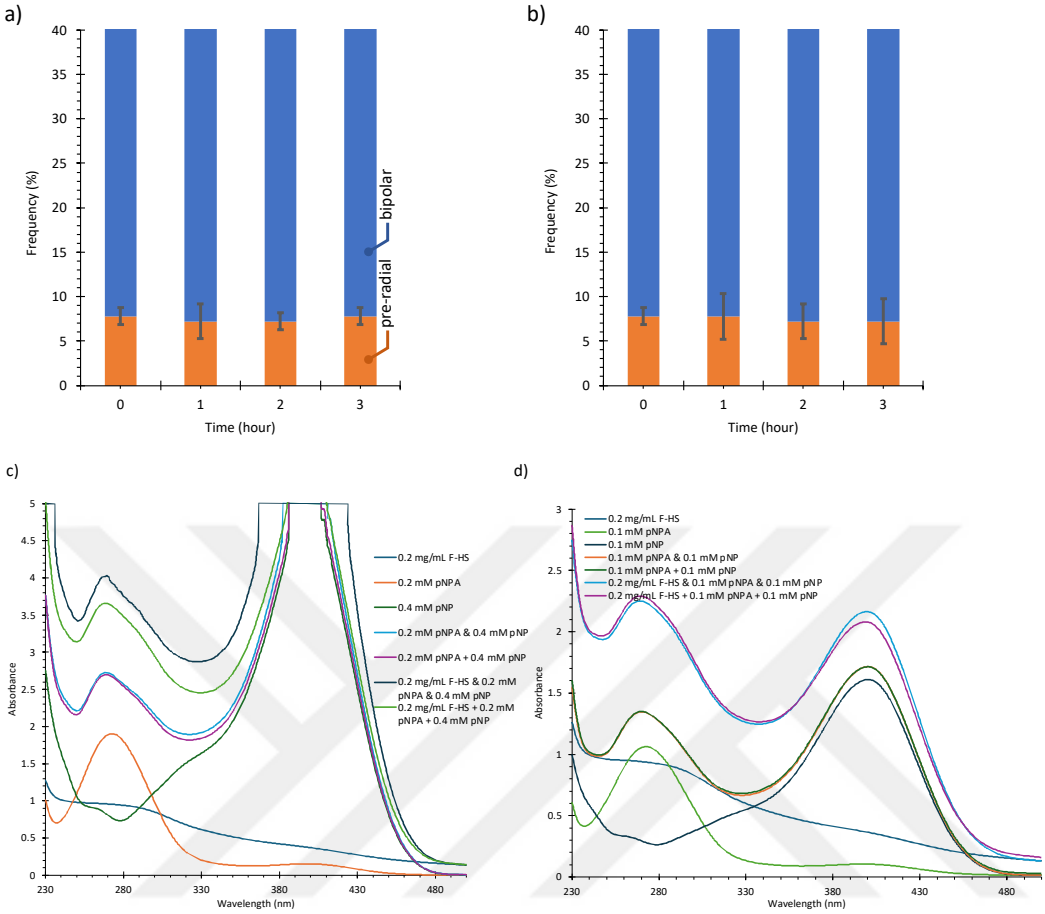

Figure 4.21. (a) Distribution of 5CB droplet configurations measured at time points 0, 1, 2, and 3 hours in the presence of (a) 0.4 mM *p*NP in PBS (n=3), or (b) 0.4 mM *p*NP and 0.2 mM *p*NPA in PBS (n=3). Absorbance spectra as a function of wavelength for (c) 0.2 mg/mL F-HS, 0.2 mM *p*NPA, 0.4 mM *p*NP, the immediate mixture of 0.2 mM *p*NPA and 0.4 mM *p*NP, the immediate mixture of 0.2 mg/mL F-HS with 0.2 mM *p*NPA and 0.4 mM *p*NP, and the sums of their individual spectra. (d) Same as (c), except with 0.1 mM *p*NPA and 0.1 mM *p*NP.

To probe the influence of the [*p*NPA]/[*p*NP] ratios on recovery time, we tested various ratios (1, 2, 4, 5, 9, and 24) using the procedure outlined in Figure 4.19b: *p*NPA was added to the emulsion in F-HS solution, followed by *p*NP, and time-dependent droplet configurations were monitored. We performed these

experiments using 0.5 mg/mL F-HS, and the obtained graphs are represented in Figure 4.22. *p*NPA and *pNP* were each prepared as stock solutions in DMSO, and both were present in the system during these experiments. The total amount of DMSO in the samples was within the limits tested in Figure 4.4b, where no significant effects of DMSO were observed.

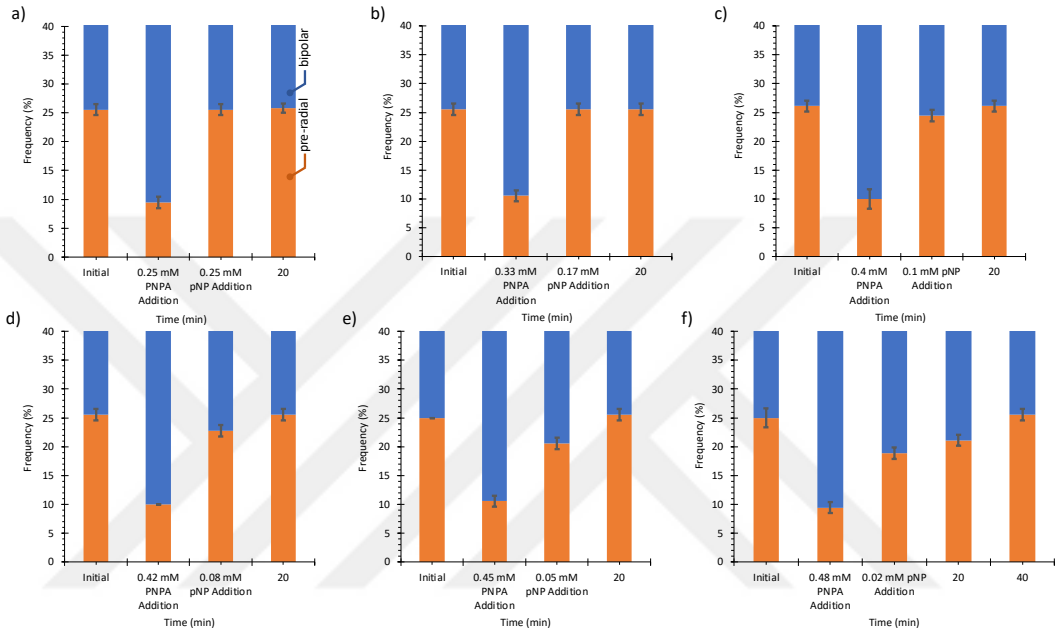

Figure 4.22. 5CB droplet configuration distribution dispersed in 0.5 mg/mL F-HS after sequential addition of *p*NPA and *p*NP at varying molar concentration ratios ([*p*NPA]/[*p*NP]) (n=3). (a) Ratio of 1. (b) Ratio of 2. (c) Ratio of 4. (d) Ratio of 5. (e) Ratio of 9. (f) Ratio of 24.

We defined Δconfig.$_{\text{Product}}$ as the difference between the preradial droplet configuration induced by *p*NP addition (after the addition of *p*NPA) and the F-HS-only configuration. Figure 4.23 presents the Δconfig.$_{\text{Product}}$ results for different [*p*NPA]/[*p*NP] ratios using the experiment's results in Figure 4.22. As seen in the plot, Δconfig.$_{\text{Product}}$ emerge at a [*p*NPA]/[*p*NP] ratio of 4, with its effect increasing at higher ratios. These findings indicate that recovery time is modulated by the

[*p*NPA]/[*p*NP] ratio in contact with the F-HS, with the LC droplet interfaces response being sensitive to bulk concentration changes.

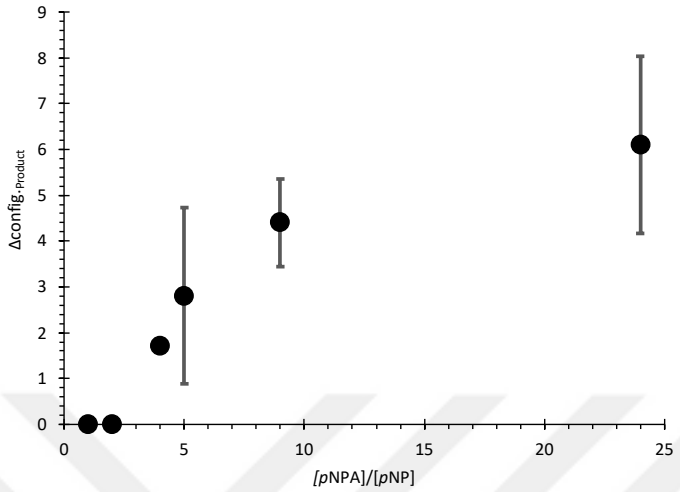

Figure 4.23. Δconfig.$_{Product}$ values obtained at various [*p*NPA]/[*p*NP], calculated as the difference between the preradial configuration frequency observed in the F-HS-only system and that observed immediately after *p*NP addition.

To elucidate the effect of the [*p*NPA]/[*p*NP] ratio on recovery time, we analyzed the results obtained from UV measurements presented in Figure 4.14, Figure 4.15a, b. Absorbance values and the corresponding time-dependent *p*NP concentrations are shown in Figure 4.14 (0.5 mg/mL F-HS, 0.5 mM *p*NPA), Figure 4.15a (0.5 mg/mL F-HS, 0.4 mM *p*NPA), and Figure 4.15b (0.5 mg/mL F-HS, 0.8 mM *p*NPA). The recovery times for 0.4 mM, 0.5 mM, and 0.8 mM *p*NPA were previously determined to be in the range 60 to 80 minutes (Figure 4.12d-f). However, the 20-minute measurement intervals create a broad window between consecutive time points, limiting precision. While we initially reported single recovery time values, we sought to conduct a more detailed analysis of the [*p*NPA]/[*p*NP] ratio. Therefore, we evaluated the recovery times for the interactions of 0.4 mM, 0.5 mM, and 0.8 mM pNPA as ranges: 40–60 minutes, 40–60 minutes, and 60–80 minutes, respectively. We calculated the [*p*NPA]/[*p*NP] ratios for each time range to interpret their impact. For the interaction of the enzyme with 0.4 mM *p*NPA, the

[*p*NPA]/[*p*NP] ratios at 40 and 60 minutes were 6.5 and 3.9, respectively. For 0.5 mM *p*NPA, the ratios at 40 and 60 minutes were 6.6 and 4, respectively. For 0.8 mM *p*NPA, the ratios at 60 and 80 minutes were 4.7 and 3.3, respectively. Taking the averages of these ratios yields values of 5.2, 5.5, and 4 for 0.4 mM, 0.5 mM, and 0.8 mM *p*NPA, respectively. When compared with the trends observed in Figure 4.23, these results correlate, suggesting that the [*p*NPA]/[*p*NP] ratio at the F-HS interface is a key determinant of the observed recovery times. However, while UV measurements provide [*p*NPA]/[*p*NP] ratios for the total system, the recovery time is likely governed by the interfacial [*p*NPA]/[*p*NP] ratio, which may remain relatively stable despite *p*NP accumulation in the bulk. The slight decline in these ratios with 0.8 mM *p*NPA may result from greater *p*NP accumulation in the bulk.

4.2 Engineering Fullerene-Based Enzyme Mimics for Enhanced Sensing of Aqueous Phase Reactions using Liquid Crystals

We modified the chemistries of fullerene-based enzyme mimics to investigate their interfacial and catalytic features, resulting in changes in the response characteristics of the LC droplets. Our system consists of three essential components dispersed in PBS solutions:

1) the thermotropic room-temperature nematic LC, 4-pentyl-4'-cyanobiphenyl (5CB),
2) fullerene-based enzyme mimics, which include the previously reported F-HS,[30,31] and newly used fullerenol-serine (F-S), and synthesized fullerenol-serine-polyethylene glycol (F-S-PEG) and fullerenol-serine-dodecyl amine (F-S-C12) in this section,
3) the substrate *para*-nitrophenyl acetate (*p*NPA).

In F-HS, histidine and serine amino acids were immobilized on the fullerenol scaffold, whereas F-S has only serine; F-S-PEG includes polyethylene glycol for increased hydrophilicity, and F-S-C12 has dodecyl chains to introduce

hydrophobicity in addition to the serine amino acids, as shown with representative structures in Figure 4.24a. These modifications enabled us to probe their influences on ester hydrolysis reactions using the model substrate *p*NPA and the response of 5CB droplets against their interaction with the LC (structured oil)-aqueous interfaces during this hydrolysis activity. The 5CB droplets with sizes within the 1 to 10 μm diameters range were dispersed in enzyme mimic solutions prepared in PBS solution. This size range was selected to allow competition between LC interfacial anchoring and elastic energies.[41,42]

The formation of distinct nematic 5CB droplet configurations through changes in interfacial anchoring enables the detection of molecular interactions at LC-aqueous interfaces. In the experimental results below, we report the response of the LC droplets as the configuration distributions maintained within a population of droplets in the specific medium, with three major configurations shown in Figure 4.24b. The bipolar configuration exhibits tangential LC orientation with two distinct point defects (boojums) located at opposite poles that produce a dark appearance under crossed polarizers, while the surrounding LC regions display bright birefringent colors. The preradial configuration results from tilted interfacial LC alignment, which creates a single point defect at the droplet surface, resulting in a specific optical appearance. The radial configuration involves LC directors aligned normal to the interface, with a central point defect producing a symmetrical four-petal optical appearance under polarized light. We note that these droplet configurations were previously characterized for multiple different systems, and the details of the configurations and their energetics can be found elsewhere.[1,41]

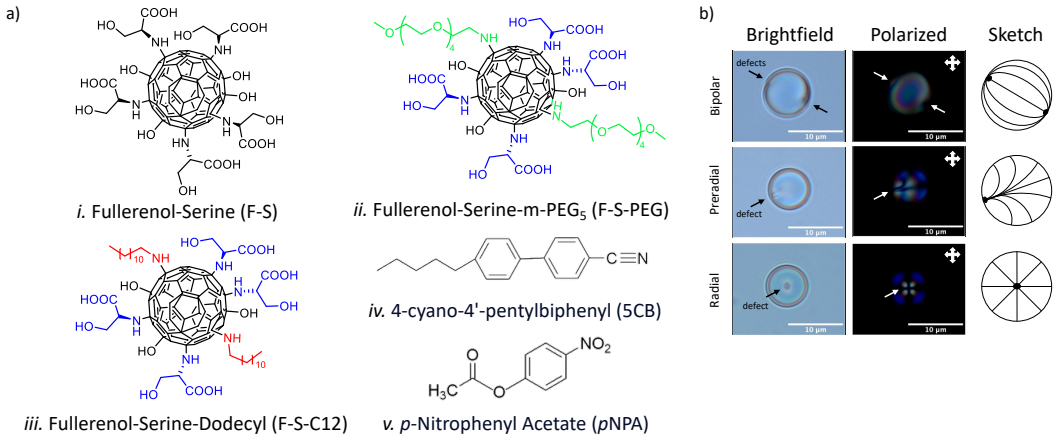

Figure 4.24. (a) Molecular structures of the enzyme mimics and substrate used in this section: *i.* Fullerenol-Serine (F-S), *ii.* Fullerenol-Serine-m-PEG$_5$ (F-S-PEG), *iii.* Fullerenol-Serine-Dodecyl Amine (F-S-C12), *iv.* 4-cyano-4'-pentylbiphenyl (5CB), *v.* *p*-Nitrophenyl Acetate (*p*NPA). (b) Brightfield (left) and polarized light microscopy (middle) images of three 5CB droplets, depicting bipolar, preradial, and radial configurations, as shown in the sketch (right).

We showed that the baseline configuration distribution of the 5CB droplets dispersed in PBS solutions were 6.7% ± 1.7% preradial (n=3) and the rest was bipolar, which was in line with the Figure 4.4 (Figure 4.26a). Droplets dispersed in solutions of 1 mg/mL fullerenol (no conjugated amino acids) resulted in statistically equivalent results (7.2% ± 1.0% preradial, n=3), indicating its insignificant effect on 5CB droplet configurations as shown in Figure 4.25. 5CB droplets dispersed in 1 mg/mL solutions of F-HS and F-S enzyme mimics resulted in their configuration distributions that depend on their amino acid content, as shown by the strong dependency of the maintained droplet configuration distributions on the chemical structures of the enzyme mimics (Figure 4.25). Figure 4.26a shows the configuration distributions of 5CB droplets induced by the four enzyme mimics (F-HS, F-S, F-S-PEG, and F-S-C12) at 0.2 mg/mL concentrations. We note that these configuration distributions were time invariant and assumed soon after dispersing the droplets in solutions. As shown, F-HS resulted in bipolar and preradial configurations with a preradial frequency of 18.9% ± 1% (n=3) while droplets incubated in solutions of F-

S and F-S-PEG resulted in preradial frequencies of 21.1% ± 1% (n=3), and 32.2% ± 1% (n=3), respectively, where the rest were bipolar. As presented in Figure 4.26a, 5CB droplets dispersed in solutions of 0.4 mM *p*NPA resulted in 7.2% ± 1.0% (n=3) preradial configuration, and the rest was bipolar, which was statistically indistinguishable from that obtained in PBS ($p>0.5$). We also measured the interfacial tension of 5CB-aqueous interfaces equilibrated with 0.2 mg/mL solutions of F-HS, F-S, and F-S-PEG (Figure 4.27, Appendix H, Figure H. 1), which showed a significant reduction in the interfacial tensions after addition of the enzyme mimics, supporting their interactions with the 5CB-aqueous interfaces. These results revealed that the F-HS, F-S, and F-S-PEG caused tilted interfacial anchoring of mesogens at aqueous interfaces.

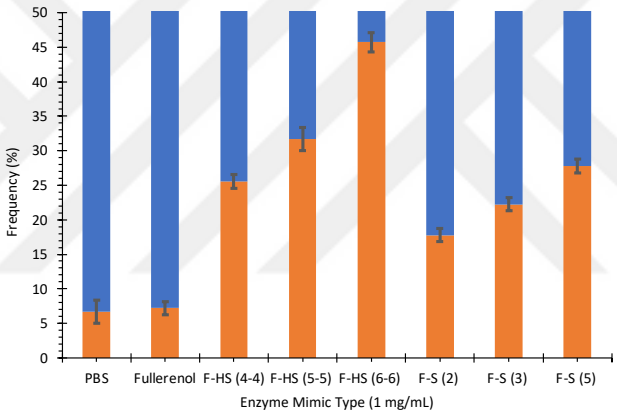

Figure 4.25. Configuration frequency distribution of 5CB droplets in PBS and with 1 mg/mL fullerenol, F-HS (4H 4S, 5H 5S, 6H 6S), and F-S (2S, 3S, 5S), varying in histidine and serine content (n=3).

5CB droplets dispersed in 0.2 mg/mL solution of F-S-C12 yielded 88.9% ± 1% radial and 11.1% ± 1% preradial configurations (n=3) (Figure 4.26a). This difference was significant when compared to the equivalent results with F-S, F-HS, or F-S-PEG enzyme mimics causing preradial and bipolar configuration. The alkyl-tailed surfactants SDS, CTAB, and DTAB are known to induce homeotropic interfacial anchoring in 5CB droplets, resulting in radial droplet configurations.[10,40] Thus, this result was reasoned to be due to the alkyl-tailed structure of the F-S-C12

that promoted homeotropic LC anchoring at the aqueous interface, similar to the surfactants.

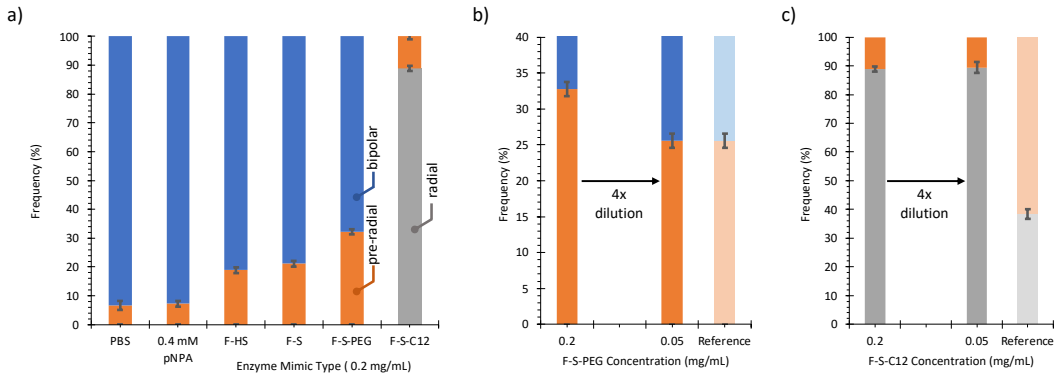

Figure 4.26. (a) Configuration distribution of 5CB droplets dispersed in PBS, 0.4 mM *p*NPA solution, and 0.2 mg/mL solutions of F-HS, F-S, F-S-PEG, and F-S-C12 enzyme mimics (n=3). (b) Configuration distribution of 5CB droplets dispersed in 0.2 mg/mL of F-S-PEG solutions before and after dilution to 0.05 mg/mL with PBS solution (n=3). Reference data reflects the configuration frequency distribution of the 5CB droplets dispersed directly in 0.05 mg/mL F-S-PEG solution (n=3). (c) Configuration distribution of 5CB droplets dispersed in 0.2 mg/mL of F-S-C12 solutions before and after dilution to 0.05 mg/mL with PBS solution (n=3). Reference data reflects the configuration frequency distribution of the 5CB droplets dispersed directly in 0.05 mg/mL F-S-C12 solution (n=3).

To provide more insight into the interfacial structures of the chemically modified F-S-PEG and F-S-C12 enzyme mimics at the 5CB-aqueous interface, we conducted reversibility experiments to evaluate the changes in configurations and interfacial tensions. As shown in Figure 4.26b, the preradial configurations of the droplets dispersed in 0.2 mg/mL of F-S-PEG (32.8% ± 1% (n=3)) were reduced to 25.6% ± 1% (n=3) upon four-fold dilution to 0.05 mg/mL with fresh PBS solution. This value was statistically equivalent ($p>0.5$) to the direct measurements at 0.05 mg/mL F-S-PEG as presented as the 'reference' data shown in Figure 4.26b. The results demonstrated that F-S-PEG underwent a reversible adsorption to the 5CB-

aqueous interfaces. Supporting this observation, the recovery of the interfacial tension of 5CB-aqueous phases following the dilution of the aqueous medium of F-S and F-S-PEG solutions demonstrated the effect of reversibility, as shown in Figure 4.27. Conversely, experiments with 5CB droplets dispersed in 0.2 mg/mL of F-S-C12 (88.9% ± 1% radial, n=3) did not reveal a measurable change upon dilution to 0.05 mg/mL (89.4% ± 1.9% radial, n=3, Figure 4.26c). The values deviated substantially from the direct measurements of droplet configurations in 0.05 mg/mL F-S-C12 solution as shown in the "reference" data in Figure 4.26c (n=3). In addition, we did not observe a change in the interfacial tension of 5CB-aqueous interface upon dilution of F-S-C12 solutions from 0.2 mg/mL to 0.1 mg/mL, collectively suggesting their irreversible adsorption to the 5CB-aqueous interface (Figure 4.27). We reasoned that the alkyl tail terminated structure of F-S-C12 enzyme mimic promoted the hydrophobic interactions between the LC medium and the enzyme mimics to result in irreversible accumulation of the enzyme mimics at the LC-aqueous interfaces. We demonstrated that chemical modifications to the enzyme mimics bring considerable impact on their adsorption mechanisms, highlighting the crucial function of alkyl chain hydrophobicity in adjusting adsorption characteristics at the 5CB-aqueous interface. Such effects revealed two distinct systems: the first is an interface facilitating a reversible adsorption of enzyme mimics (for F-HS, F-S, or F-S-PEG), whereas the second is an enzyme mimic-immobilized interface (for F-S-C12).

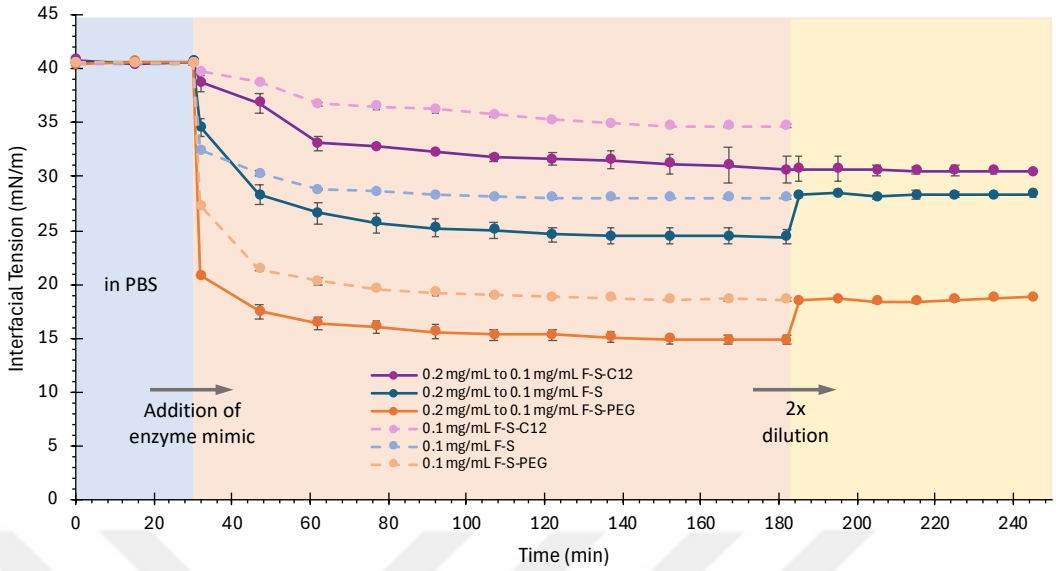

Figure 4.27. Time-dependent interfacial tension measurements of 5CB-aqueous interfaces equilibrated with solutions of fullerene-based enzyme mimics, F-S-C12, F-S, and F-S-PEG using the pendant drop technique. The data shown as solid lines were obtained at initial enzyme mimic concentrations of 0.2 mg/mL in PBS was followed by their dilution to 0.1 mg/mL using fresh PBS after 150 min of incubation. The data shown with dashed lines were obtained at enzyme mimic concentrations of 0.1 mg/mL in PBS. The data were collected every 15 minutes before dilution and every 10 minutes after dilution. Experiments were performed in three independent measurements, reported as mean ± standard deviation.

After the characterization of the 5CB droplet responses and the interfacial structures in solutions of enzyme mimics, we investigated the time-dependent configuration distributions of 5CB droplets equilibrated with 0.2 mg/mL solutions of F-HS, F-S, F-S-PEG, and F-S-C12 enzyme mimics upon the addition of *p*NPA substrate. The results for droplets in 0.2 mg/mL F-HS after the addition of 0.4 mM *p*NPA are presented in Figure 4.28a, and data were collected at 20-minute intervals for 80 minutes. The "initial" data for the 5CB droplet configuration distributions in the presence of the enzyme mimic in PBS solution alone showed a preradial configuration of 19.4% ± 1% (n=3). The initial data, "t=0", which is the 5CB droplet

configurations at the time of *p*NPA addition, exhibited a reduction in preradial configuration frequency to 11.7% ± 0% (n=3). The preradial configuration frequency generated by *p*NPA alone, marked with an asterisk (*) in Figure 4.28a, was found to be 7.2% ± 1.0%. We note that the reduction at t=0 did not completely reach this value; however, it exhibited a definite trend towards the *p*NPA-only induced configuration distribution, reflecting interactions between F-HS and *p*NPA at the interface. The recovery time, defined as the duration required for the configuration distribution to return to its initial state, was found to be 60 minutes for the medium of 0.2 mg/mL F-HS and 0.4 mM *p*NPA. The temporal configuration distributions of droplets incubated in 0.2 mg/mL F-S after the addition of 0.4 mM *p*NPA are presented in Figure 4.28b. The droplet configuration distributions in the presence of the F-S enzyme mimic alone showed a preradial configuration of 22.2% ± 1% (n=3), which was reduced to a preradial configuration frequency of 12.8% ± 1% (n=3) after the addition of *p*NPA. In this case, the recovery time was found to be 100 mins. Figure 4.28c presents droplet configuration distributions over time for droplets incubated in 0.2 mg/mL F-S-PEG solutions after the addition of 0.4 mM *p*NPA. The initial data of preradial configuration of 32.8% ± 1% (n=3), was decreased to 23.9% ± 1% (n=3) at t=0 following *p*NPA addition. The recovery time for this interaction was 80 minutes. Figure 4.28d presents the time-dependent frequency distributions of droplet configurations incubated in 0.2 mg/mL F-S-C12 solutions upon addition of 0.4 mM *p*NPA. The initial data revealed a radial configuration frequency of 88.9% ± 1% (n=3), which was decreased to 72.2% ± 2.5% (n=3) at t=0 with the addition of *p*NPA. Recovery time was found to be 140 minutes.

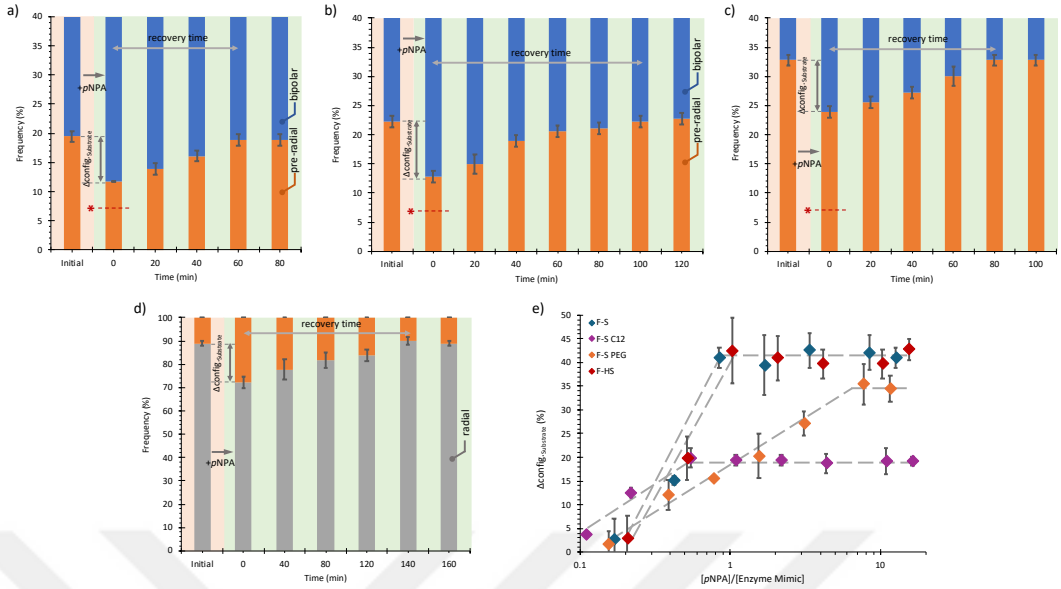

Figure 4.28. Configuration distributions of 5CB droplets incubated in 0.2 mg/mL solutions of (a) F-HS, (b) F-S, (c) F-S-PEG, (d) F-S-C12, and time-dependent changes in configuration distributions after adding 0.4 mM *p*NPA (n=3). The single-asterisk (*) in (a–c) denotes the preradial configuration frequency induced solely by the *p*NPA solution. (e) Normalized Δconfig.$_{\text{Substrate}}$ as a function of molar ratios of *p*NPA to enzyme mimic ([*p*NPA]/[Enzyme Mimic]) for F-HS, F-S, F-S-PEG, and F-S-C12, with enzyme mimic concentrations kept constant at 0.2 mg/mL. Δconfig.$_{\text{Substrate}}$ data are normalized to the configuration frequencies induced by each enzyme mimic. For F-HS, F-S and F-S-PEG, Δconfig.$_{\text{Substrate}}$ represents the normalized change in preradial configuration frequency induced by *p*NPA in the presence of the enzyme mimic, while for F-S-C12, it represents the normalized change in radial configuration frequency induced by *p*NPA in the presence of the enzyme mimic. Data represent averages and standard deviations from three independent measurements (n=3).

To investigate the interaction between *p*NPA and enzyme mimic further, we conducted experiments on droplet configuration distributions with constant concentration of enzyme mimic at 0.2 mg/mL with varied concentrations of *p*NPA. For F-HS, F-S, and F-S-PEG, the concentrations of *p*NPA varied from 0.02 to 1.5

mM, and the obtained results are presented in Appendix İ, Figure İ. 1, Appendix J, Figure J. 1, and Appendix K, Figure K. 1. For F-S-C12, the concentration of *p*NPA was also changed from 0.01 to 1.5 mM, and the results are displayed in Appendix L, Figure L. 1. We defined the $\Delta config._{Substrate}$ to compare the changes in the droplet configurations upon addition of *p*NPA at t=0. For F-HS, F-S, and F-S-PEG, $\Delta config._{Substrate}$ is the difference between preradial configuration frequency induced by the enzyme mimic alone and that obtained just after *p*NPA addition (t=0 min), as displayed in Figure 4.28a-c. For F-S-C12, as shown in Figure 4.28d, $\Delta config._{Substrate}$ is the difference in radial configuration frequency between the enzyme alone state and that just after *p*NPA addition. Due to the variation in the distribution of configurations induced by various enzyme mimics, we normalized the $\Delta config._{Substrate}$ values relative to the enzyme-only configuration to allow direct comparisons, and the data obtained are plotted in Figure 4.28e with respect to the *p*NPA concentration and also to the ratio of *p*NPA concentration to enzyme mimic concentration ([*p*NPA]/[Enzyme Mimic]). Analysis indicated that $\Delta config._{Substrate}$ plateaued at 41.1% ± 1.5% for F-HS, 41.2% ± 1.2% for F-S, 34.9% ± 0.7% for F-S-PEG, and 19.3% ± 0.4% for F-S-C12. [*p*NPA]/[Enzyme Mimic] ratios at saturation were found to be 1.0 for F-HS, 0.8 for F-S, 7.8 for F-S-PEG, and 0.5 for F-S-C12. In comparing F-S and F-S-PEG, we hypothesize that the hydrophilic modification of F-S-PEG results in reduced interactions between the hydrophobic *p*NPA substrate at the enzyme mimic interface. The attached PEG chains may also facilitate steric hindrance, thus further preventing the contact of *p*NPA with the interface of the enzyme mimic.[78,79] These factors are expected to hinder the partitioning of *p*NPA at the interface, thus necessitating a significantly higher [*p*NPA]/[Enzyme Mimic] ratio for the attainment of saturation of $\Delta config._{Substrate}$. The $\Delta config._{Substrate}$ stabilization value, being slightly lower for F-S-PEG compared to F-S, can also be due to reduced enzyme-*p*NPA complex formation at the interface owing to the hydrophilic nature and steric hindrance of the PEG chains. For F-HS and F-S, $\Delta config._{Substrate}$ stabilization values were statistically equivalent, with similar [*p*NPA]/[Enzyme Mimic] ratios at stabilization. Considering the analogous chemical structures of F-

HS and F-S, their similar interactions with *p*NPA are consistent with expected outcomes.

The results of the F-S-C12 enzyme mimic indicated that it accomplishes the stabilization of $\Delta config._{Substrate}$ at a much lower value than the other enzyme mimics. We hypothesize that this outcome was due to the collective impact of a number of factors. F-S-C12, in contrast to other enzyme mimics, possesses a structure of an alkyl tail that facilitates strong anchoring at the 5CB-aqueous interface, leading to a high frequency of radial configuration and irreversible adsorption, as demonstrated in Figure 4.26a and c. We propose that this strong anchoring implies that *p*NPA is comparatively less prone to change the interfacial structure compared to the interfaces formed by other enzyme mimics, and therefore, it is difficult to influence this configuration. Consistent with the longer recovery times shown in Figure 4.28d, irreversible adsorption of F-S-C12 indicated it to be submerged significantly within the 5CB phase, and this would hinder access and thereby lower the effect of *p*NPA on the interaction of F-S-C12 with 5CB. We propose that steric hindrance imparted by the C12 tails may prevent the partitioning of *p*NPA to the interface of the enzyme mimic. Together, these factors act to reduce the stabilized value of $\Delta config._{Substrate}$. The ratio of [*p*NPA]/[Enzyme Mimic] at which $\Delta config._{Substrate}$ saturated for F-S-C12 was also lower compared to other enzyme mimics. This showed that the saturation of the F-S-C12 interfaces with *p*NPA occurred at low concentrations of *p*NPA, consistent with its enhanced hydrophobic characteristics.

In our experiments on the interactions of F-S-C12 and *p*NPA, we still observed a response with a recovery time of 20 minutes at the lowest *p*NPA concentration which was measured at 0.01 mM (Appendix L, Figure L. 1a). For the other enzyme mimics studied—F-HS (Appendix İ, Figure İ. 1b), F-S (Appendix J, Figure J. 1b), and F-S-PEG (Appendix K, Figure K. 1b)—the minimum *p*NPA concentration at which we observed a response was 0.05 mM. This is potentially due to the enhanced hydrophobicity of F-S-C12, leading to detectable interactions at significantly lower *p*NPA concentrations, thus enhancing the sensitivity of our system. Figure 4.29

displays the recovery times of droplet configurations in 0.2 mg/mL F-HS, F-S, F-S-PEG upon addition of 0.02–1.5 mM *p*NPA, and F-S-C12 upon addition of 0.01–1.5 mM *p*NPA as a function of [*p*NPA]/[Enzyme Mimic]. The enzyme mimics follow similar trends, with the recovery times rising with higher [*p*NPA]/[Enzyme Mimic] ratios in agreement with the *p*NPA concentrations. Further, this observation was also in agreement with the interaction of 0.2 mg/mL enzyme mimics (F-HS, F-S, F-S-PEG, F-S-C12) with 0.4 mM *p*NPA, as indicated in Figure 4.28a-d, the recovery times at similar [*p*NPA]/[Enzyme Mimic] ratios follow the order from shortest to longest: F-HS, F-S-PEG, F-S, and F-S-C12. Experiments on enzyme mimic-*p*NPA interactions indicate that the hydrophilic (F-S-PEG) and hydrophobic (F-S-C12) modifications, in contrast to F-HS and F-S, impart distinct interaction dynamics with *p*NPA, thereby tuning the response of the LCs.

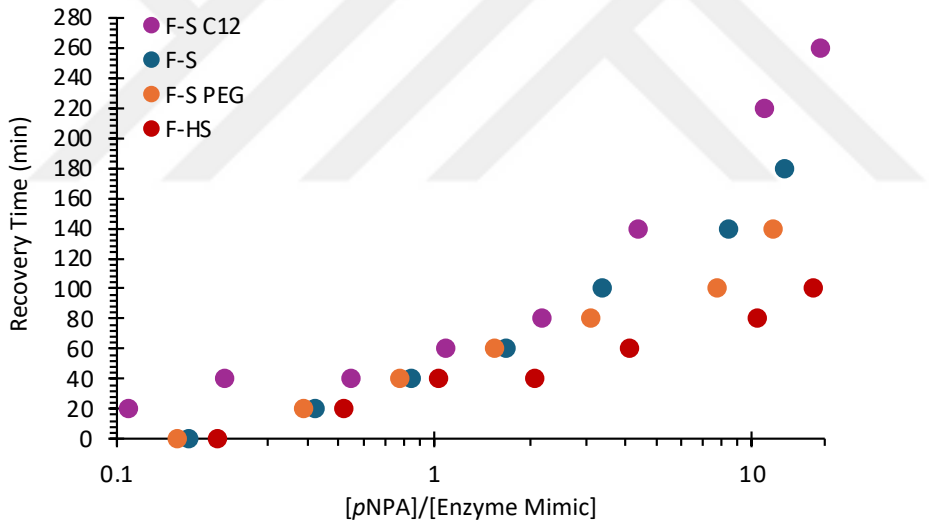

Figure 4.29. The configuration distribution recovery time of the droplets as a function of concentration ratios of *p*NPA to enzyme mimic ([*p*NPA]/[Enzyme Mimic]) for F-HS, F-S, and F-S PEG (0.02–1.5 mM *p*NPA) and F-S C12 (0.01–1.5 mM *p*NPA) at 0.2 mg/mL.

The catalytic activities of 0.2 mg/mL enzyme mimics (F-HS, F-S, F-S-C12, F-S-PEG) at the experimental conditions with (0.3% vol) and without the presence

of the dispersed 5CB droplets were determined by measuring *p*NPA hydrolysis. We used UV-vis spectrophotometry to track the formation of *p*NP. Figure 4.30 is a plot of time-dependent absorbance (left, red axis) and corresponding *p*NP concentrations (right, blue axis) of the 0.4 mM *p*NPA interactions with F-HS (Figure 4.30a), F-S (Figure 4.30b), F-S-PEG (Figure 4.30c), and F-S-C12 (Figure 4.30d) enzyme mimics. Results from samples containing 5CB are indicated with solid lines, and those without 5CB are indicated with dashed lines. Experiments investigating droplet configurations with 0.2 mg/mL enzyme mimics and 0.4 mM *p*NPA revealed recovery times of 60 minutes for F-HS, 100 minutes for F-S, 80 minutes for F-S-PEG, and 140 minutes for F-S-C12 (Figure 4.28). To calculate *p*NP concentrations more accurately, we analyzed recovery times as time ranges: 40–60 minutes for F-HS, 80–100 minutes for F-S, 60–80 minutes for F-S-PEG, and 120–140 minutes for F-S-C12 (Table 2). The *p*NP concentrations corresponding to these are shown as dark dots (•) on the plots in the presence of 5CB, with the average *p*NP concentration for these ranges indicated with a plus (+) sign. The absorbance and concentrations of *p*NP were linearly incremented within the ranges of recovery times, without showing a noticeable change, which we also explained in more detail in Figures 4.14 and 4.15. Thus, the response measured by the configuration changes within the droplets were not due to a change in the kinetic activity of the enzyme mimics.

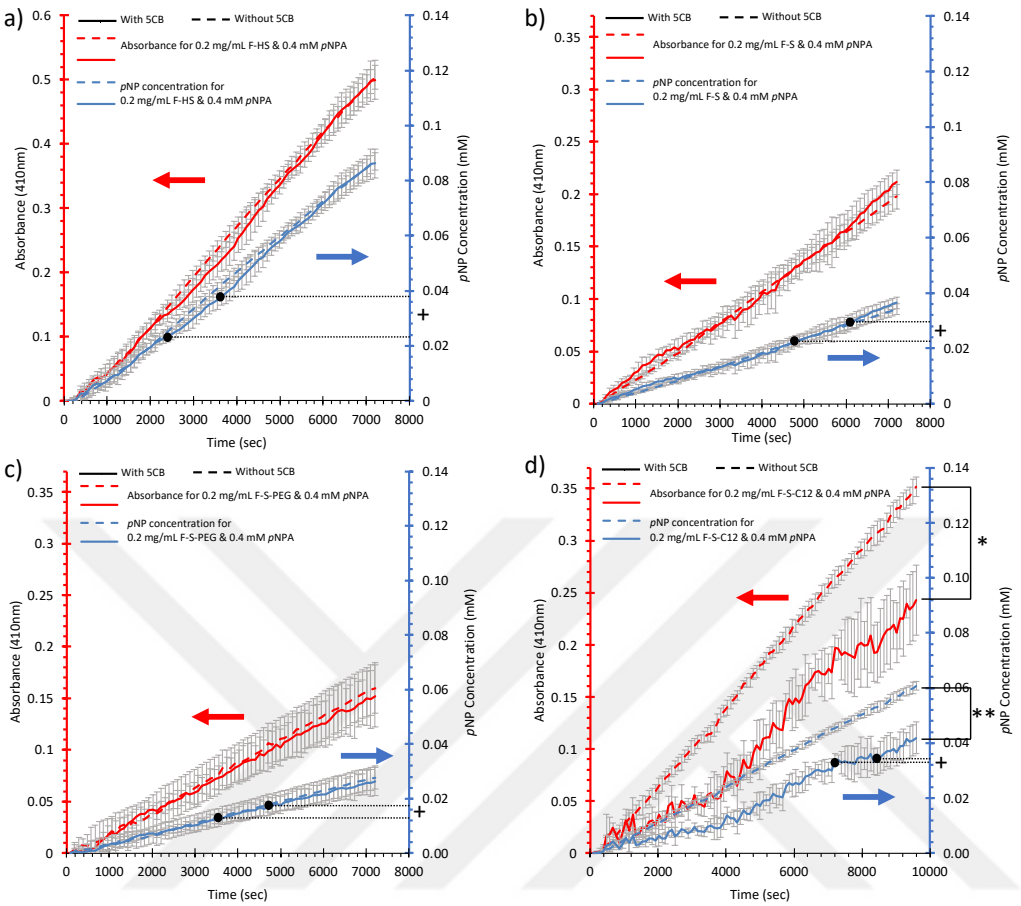

Figure 4.30. Time-dependent absorbance and corresponding *p*NP concentrations for (a) 0.2 mg/mL F-HS with 0.4 mM *p*NPA (7200 s), (b) 0.2 mg/mL F-S with 0.4 mM *p*NPA (7200 s), (c) 0.2 mg/mL F-S-PEG with 0.4 mM *p*NPA (7200 s), and (d) 0.2 mg/mL F-S-C12 with 0.4 mM *p*NPA (9600 s), measured at 410 nm and room temperature using UV-Vis spectroscopy with and without 5CB. Solid lines represent data with 5CB, dashed lines without 5CB. Dark dots (•) represent the recovery time intervals and dotted lines mark *p*NP concentrations at these intervals, with average *p*NP concentration indicated by a plus (+) symbol. Graphs represent mean ± standard deviation from three independent experiments.

We investigated the interactions of 0.8 mM *p*NP —double the amount of *p*NP obtained from the complete hydrolysis of 0.4 mM *p*NPA— with 0.2 mg/mL enzyme mimics (F-HS, F-S, F-S-PEG, F-S-C12) in the absence of *p*NPA. We observed that

the addition of *p*NP did not influence the configuration distribution of the 5CB droplets interacting with enzyme mimics (Appendix M, Figure M. 1). When we quantified the mean [*p*NP]/[*p*NPA] ratio within the recovery time interval of the droplets dispersed in F-HS solutions between 40 and 60 minutes was determined to be 0.082 ± 0.023 using the data shown in Figure 4.30a (as indicated by the average *p*NP concentration plotted with a plus (+) sign) and as shown in Table 2. For the F-S, the recovery time interval of between 80 and 100 minutes corresponded to an average [*p*NP]/[*p*NPA] of 0.069 ± 0.011 (Figure 4.30b). For F-S-PEG, as shown in Figure 4.30c, the recovery time interval between 60 and 80 minutes yielded an average [*p*NP]/[*p*NPA] ratio of 0.039 ± 0.009. Lastly, for F-S-C12, as shown in Figure 4.30d, the recovery time interval between 120 and 140 minutes, marked with dark dots (•), corresponded to an average [*p*NP]/[*p*NPA] ratio of 0.092 ± 0.010.

Table 2. The recovery time intervals of the droplets dispersed in 0.2 mg/mL solutions of enzyme mimics and the average [*p*NP]/[*p*NPA] corresponding to this time interval after addition of *p*NPA

Enzyme Mimic	Recovery Time Interval (min)	$[pNP]/[pNPA]_{ave}$ in 0.4 mM *p*NPA	$[pNP]/[pNPA]_{ave}$ in 1.5 mM *p*NPA
F-HS	40-60	0.082 ± 0.023	0.076 ± 0.013
F-S	80-100	0.069 ± 0.011	0.069 ± 0.007
F-S-PEG	80-100	0.039 ± 0.009	0.041 ± 0.006
F-S-C12	120-140	0.092 ± 0.010	0.099 ± 0.016

In contrast to other enzyme mimics, F-S-C12 forms irreversible enzyme mimic-adsorbed 5CB-aqueous interfaces while demonstrating catalytic activity for the hydrolysis of *p*NPA. Appendix N, Figure N. 1 displays the graphs of time-dependent absorbance along with the associated *p*NP concentration for the medium of 0.2 mg/mL of F-HS, F-S, F-S-PEG, or F-S-C12 with 1.5 mM *p*NPA. The [*p*NP]/[*p*NPA] ratios averaged over the recovery time ranges of the droplets dispersed in F-HS, F-S, F-S-PEG, and F-S-C12 solutions were 0.076 ± 0.013, 0.069

± 0.007, 0.041 ± 0.006, and 0.099 ± 0.016, respectively, which was similar to the ratio using 0.4 mM *p*NPA (Table 2). Correspondingly, based on these two concentrations of *p*NPA, the ratios of [*p*NP]/[*p*NPA] at recovery times for the enzyme mimics F-HS, F-S, F-S-PEG, and F-S-C12 of 0.2 mg/mL were 0.079 ± 0.018, 0.069 ± 0.009, 0.040 ± 0.007, and 0.095 ± 0.013, respectively. The [*p*NP]/[*p*NPA] ratio of 0.079 ± 0.018 for 0.2 mg/mL F-HS at the recovery time was lower than the ratio measured as ~0.25 with 0.5 mg/mL F-HS in Figure 4.23. Such a difference can be reasoned to be the higher partitioning of *p*NP at lower enzyme concentration. Decreased product formation was thus enough for enzyme mimic-substrate-product equilibrium (Figure 4.30a).

The time-dependent absorbance and *p*NP concentrations measured in solutions of F-HS, F-S and F-S-PEG enzyme mimics were indistinguishable for the 5CB-containing and 5CB-free samples, showing no measurable influence of the presence of 5CB droplets in the hydrolysis kinetics of the enzymes (Figure 4.30a-c). However, for the droplets incubated in solutions of F-S-C12, there was a significant reduction of absorbance and the corresponding *p*NP concentrations for 5CB-containing samples compared to 5CB-free samples, as indicated by * and ** in Figure 4.30d. This result was in line with the experiments reported in Figure 4.26c, Figure 4.27, and the discussion on the data that related to the irreversible adsorption of the F-S-C12 mimics to the 5CB-aqueous interfaces. When we compared the increase rates of the absorbance measured in cases of F-S, F-S-PEG, and F-S-C12 mimics, F-S-C12 exhibited a higher rate compared to others in the absence of 5CB (Figure 4.30). However, in the presence of the 5CB, the absorbance rate of F-S-C12 decreases significantly, approaching to that measured for F-S-PEG, which possessed the slowest catalytic activity among the enzyme mimics, likely due to the hydrophilic modification and steric hindrance effect (Figure 4.30c,d). The significant submersion of the F-S-C12 mimics into the 5CB phase due to their hydrophobicity potentially limited the *p*NPA access to the serine-based active sites. The steric hindrance imparted by the C12 tails may also increase this effect by further hindering the partitioning of *p*NPA. In the presence of 5CB-aqueous interfaces, these effects

dramatically lowered the catalytic activity of the F-S-C12 mimics (Figure 4.30d). Furthermore, in contrast to the other mimics, the $\Delta config._{Substrate}$ plateaued at a much lower value for F-S-C12, indicating the limitation of *p*NPA concentration at the enzyme mimic interface (Figure 4.28e). The prolonged recovery time of the droplet configurations incubated in F-S-C12 solutions compared to the other mimics further reflects limited *p*NPA access to the active sites and inhibited *p*NP accumulation at the interface due to its hydrophobic character, necessitating higher product conversion to accomplish complete recovery (Figure 4.29, Table 2). Notably, configurations of the 5CB droplets in F-S-PEG solutions achieved the second-fastest recovery time after F-HS (Figure 4.28a-d, Figure 4.29), even though it exhibited the lowest increase rate of the absorbance among the enzyme mimics (Figure 4.30). This was potentially because the hydrophilic modification in F-S-PEG leads to a low [*p*NP]/[*p*NPA] ratio (0.040 ± 0.007), which was sufficient to reach complete recovery. This was possible due to enhanced *p*NP accumulation at the interface, resulting from the hydrophilic nature of PEG chains nature.

CHAPTER 5

CONCLUSION

We demonstrate that thermotropic nematic LC droplets can serve as sensitive probes for aqueous phase reactions catalyzed by fullerene-based enzyme mimics (F-HS, F-S, F-S-PEG, and F-S-C12), specifically the hydrolysis of the model substrate *p*NPA. The responses of LC droplets to fullerene-based enzyme mimics were examined as a function of time and concentration. The results indicate that the chemical structure of the enzyme mimics strongly influences LC droplet configurations. Specifically, F-HS, F-S, and F-S-PEG mimics induce a tilted LC orientation at the LC-aqueous interface, leading to preradial droplet configurations, whereas the F-S-C12 mimic induces a homeotropic LC orientation, resulting in radial droplet configurations due to its hydrophobic modification. We characterized the LC-aqueous interface decorated with enzyme mimics by performing interfacial tension measurements and configuration reversibility experiments. Unlike other enzyme mimics, F-S-C12 formed "enzyme-immobilized" LC-aqueous interfaces with irreversible adsorption. In contrast, F-HS, F-S, and F-S-PEG mimics exhibit a reversible adsorption mechanism at the LC interfaces, as revealed by these measurements. We monitored the enzyme mimic-*p*NPA interactions by investigating the dynamic response of the LC droplets. Different chemical modifications of the enzyme mimics modulated these interactions, resulting in notable variations in LC configuration distributions and recovery times, reflecting distinct interaction dynamics. It was observed that LC droplets exhibit high sensitivity, responding to [*p*NPA]/[Enzyme mimic] as low as 0.1 (for F-S-C12 at 0.01 mM *p*NPA). Kinetic measurements of *p*NPA hydrolysis catalyzed by F-HS, F-S, and F-S-PEG mimics, conducted in the absence and presence of LC droplets, indicated that LC droplets do not affect enzymatic reaction kinetics. In contrast, the catalytic activity of F-S-C12 was significantly reduced in the presence of LC droplets. Additionally, the

[*p*NP]/[*p*NPA] ratios obtained at recovery times remained constant across different *p*NPA concentrations at a fixed enzyme mimic concentration. This observation supports that the response of LC droplets originates from enzyme mimic–substrate–product interactions in the bulk phase, with recovery times governed by the product-to-substrate concentration ratio.

Our LC-based system is ideally suited for complex catalytic systems that involve multiple enzymes and reaction pathways due to its high sensitivity, as demonstrated by its response at specific substrate-to-product ratios and low substrate concentrations. Additionally, the capacity to respond to chemical modifications of fullerene-based enzyme mimics shows the potential of LC-aqueous interfaces to identify subtle chemical changes and their impact on intermolecular interactions, opening up a versatile sensing platform. While the reaction product *p*NP does not directly affect LC droplet configurations, our system is still useful for investigating substrates or products that induce LC ordering transitions, with responses tailored to their chemical properties. Applications in biochemical assays, environmental monitoring, and clinical diagnostics are supported by these capabilities.

To further advance the LC-based sensing platform presented in this thesis for new applications, several future directions can be envisioned. First, since the fullerene-based enzyme mimics are stable single-unit catalysts, they allow facile chemical modifications at interfaces based on the characteristics of the target analyte.[30–33] This allows them to catalyze the hydrolysis of the analyte, improving the sensor's sensitivity and selectivity for particular analytes or conditions. Second, while we provided insights into the chemical structure–response relationships at LC–aqueous interfaces, the molecular-level mechanisms underlying the observed configurational transitions remain unresolved. Molecular dynamics simulations and interfacial modeling studies could provide valuable information in this regard. Thirdly, recent research reveals that microfluidic systems sustain stable LC–aqueous interfaces during simultaneous flow, allowing shear-driven interfacial deformation to facilitate precise modulation and sensitive detection of LC behaviors.[25,80]

Integrating our study with microfluidic platforms could enable real-time monitoring and automation, paving the way for fast and comprehensive diagnostic applications. Finally, research has demonstrated the usage of microfluidic flow-focusing systems to generate LC droplets with precise control over their size and uniformity.[53] Additionally, flow cytometry techniques have been shown to provide rapid, high-throughput analysis of LC droplet configurations by distinguishing light scattering patterns without the need for manual counting.[54] By combining our LC-based sensing platform with these technologies, uniform LC droplets of desired sizes can be produced, and efficient, automated configuration analysis can be performed. This approach greatly accelerates the sensing process while maintaining high accuracy for various applications.

REFERENCES

(1) Bukusoglu, E.; Pantoja, M. B.; Mushenheim, P. C.; Wang, X.; Abbott, N. L. Design of Responsive and Active (Soft) Materials Using Liquid Crystals. *Annu Rev Chem Biomol Eng* **2016**, *7*, 163–196. https://doi.org/10.1146/annurev-chembioeng-061114-123323.

(2) Bai, Y.; Abbott, N. L. Recent Advances in Colloidal and Interfacial Phenomena Involving Liquid Crystals. *Langmuir* **2010**, *27* (10), 5719–5738. https://doi.org/10.1021/la103301d.

(3) de Gennes, P. G.; Prost, J. *The Physics of Liquid Crystals*, Second edition.; Oxford University Press, 1993.

(4) Carlton, R. J.; Hunter, J. T.; Miller, D. S.; Abbasi, R.; Mushenheim, P. C.; Tan, L. N.; Abbott, N. L. Chemical and Biological Sensing Using Liquid Crystals. *Liq Cryst Rev* **2013**, *1* (1), 29–51. https://doi.org/10.1080/21680396.2013.769310.

(5) Miller, D. S.; Carlton, R. J.; Mushenheim, P. C.; Abbott, N. L. Introduction to Optical Methods for Characterizing Liquid Crystals at Interfaces. *Langmuir* **2013**, *29* (10), 3154–3169. https://doi.org/10.1021/la304679f.

(6) Lin, I. H.; Miller, D. S.; Bertics, P. J.; Murphy, C. J.; De Pablo, J. J.; Abbott, N. L. Endotoxin-Induced Structural Transformations in Liquid Crystalline Droplets. *Science* **2011**, *332* (6035), 1297–1300. https://doi.org/10.1126/science.1195639.

(7) Kim, Y. K.; Wang, X.; Mondkar, P.; Bukusoglu, E.; Abbott, N. L. Self-Reporting and Self-Regulating Liquid Crystals. *Nature* **2018**, *557* (7706), 539–544. https://doi.org/10.1038/s41586-018-0098-y.

(8) Wang, Z.; Xu, T.; Noel, A.; Chen, Y. C.; Liu, T. Applications of Liquid Crystals in Biosensing. *Soft Matter* **2021**, *17* (18), 4675–4702. https://doi.org/10.1039/d0sm02088e.

(9) Kim, Y. K.; Noh, J.; Nayani, K.; Abbott, N. L. Soft Matter from Liquid Crystals. *Soft Matter* **2019**, *15* (35), 6913–6929. https://doi.org/10.1039/c9sm01424a.

(10) Brake, J. M.; Mezera, A. D.; Abbott, N. L. Effect of Surfactant Structure on the Orientation of Liquid Crystals at Aqueous-Liquid Crystal Interfaces. *Langmuir* **2003**, *19* (16), 6436–6442. https://doi.org/10.1021/la034132s.

(11) Gupta Vinay K.; Dubrovsky, T. B.; Skaife, J. J.; Abbott, N. L. Optical Amplification of Ligand-Receptor Using Liquid Crystals. *Science* **1998**, *279* (5359), 2077–2080.

(12) Kinsinger, M. I.; Sun, B.; Abbott, N. L.; Lynn, D. M. Reversible Control of Ordering Transitions at Aqueous/Liquid Crystal Interfaces Using Functional Amphiphilic Polymers. *Advanced Materials* **2007**, *19* (23), 4208–4212. https://doi.org/10.1002/adma.200700718.

(13) Price, A. D.; Schwartz, D. K. DNA Hybridization-Induced Reorientation of Liquid Crystal Anchoring at the Nematic Liquid Crystal/Aqueous Interface. *J Am Chem Soc* **2008**, *130* (26), 8188–8194. https://doi.org/10.1021/ja0774055.

(14) Tan, L. N.; Orler, V. J.; Abbott, N. L. Ordering Transitions Triggered by Specific Binding of Vesicles to Protein-Decorated Interfaces of Thermotropic Liquid Crystals. *Langmuir* **2012**, *28* (15), 6364–6376. https://doi.org/10.1021/la300108f.

(15) Nguyen, D. K.; Jang, C. H. A Cationic Surfactant-Decorated Liquid Crystal-Based Aptasensor for Label-Free Detection of Malathion Pesticides in Environmental Samples. *Biosensors (Basel)* **2021**, *11* (3), 1–11. https://doi.org/10.3390/bios11030092.

(16) Brake, J. M.; Daschner, M. K.; Luk, Y. Y.; Abbott, N. L. Biomolecular Interactions at Phospholipid-Decorated Surfaces of Liquid Crystals. *Science* **2003**, *302* (5653), 2094–2097. https://doi.org/10.1126/science.1091749.

(17) Brake, J. M.; Abbott, N. L. Coupling of the Orientations of Thermotropic Liquid Crystals to Protein Binding Events at Lipid-Decorated Interfaces. *Langmuir* **2007**, *23* (16), 8497–8507. https://doi.org/10.1021/la0634286.

(18) Hartono, D.; Bi, X.; Yang, K. L.; Yung, L. Y. L. An Air-Supported Liquid Crystal System for Real-Time and Label-Free Characterization of Phospholipases and Their Inhibitors. *Adv Funct Mater* **2008**, *18* (19), 2938–2945. https://doi.org/10.1002/adfm.200800424.

(19) Hartono, D.; Qin, W. J.; Yang, K. L.; Yung, L. Y. L. Imaging the Disruption of Phospholipid Monolayer by Protein-Coated Nanoparticles Using Ordering Transitions of Liquid Crystals. *Biomaterials* **2009**, *30* (5), 843–849. https://doi.org/10.1016/j.biomaterials.2008.10.037.

(20) Tripathi, A.; Wolter, T. J.; Twieg, R. J.; Mavrikakis, M.; Abbott, N. L. Responsive Liquid Crystalline Materials Based on Interfacial Photocatalytic Processes. *Chemistry of Materials* **2025**, *37* (9), 3221–3235. https://doi.org/10.1021/acs.chemmater.4c03397.

(21) Bilal, M.; Cui, J.; Iqbal, H. M. N. Tailoring Enzyme Microenvironment: State-of-the-Art Strategy to Fulfill the Quest for Efficient Bio-Catalysis. *Int J Biol Macromol* **2019**, *130*, 186–196. https://doi.org/10.1016/j.ijbiomac.2019.02.141.

(22) Dobson, C. M. Protein Folding and Misfolding. *Nature* **2003**, *426* (6968), 884–890.

(23) Maldonado-Valderrama, J.; Fainerman, V. B.; Aksenenko, E.; Gálvez-Ruiz, M. J.; Cabrerizo-Vílchez, M. A.; Miller, R. Dynamics of Protein Adsorption at the Oil-Water Interface: Comparison with a Theoretical Model. *Colloids*

Surf A Physicochem Eng Asp **2005**, *261* (1–3), 85–92. https://doi.org/10.1016/j.colsurfa.2004.10.131.

(24) Bergfreund, J.; Bertsch, P.; Fischer, P. Adsorption of Proteins to Fluid Interfaces: Role of the Hydrophobic Subphase. *J Colloid Interface Sci* **2021**, *584*, 411–417. https://doi.org/10.1016/j.jcis.2020.09.118.

(25) Özşahin, A. N.; Bukusoglu, E. Responsive Soft Interface Liquid Crystal Microfluidics. *Adv Mater Interfaces* **2024**, *11* (29), 1–13. https://doi.org/10.1002/admi.202400334.

(26) Zaramella, D.; Scrimin, P.; Prins, L. J. Catalysis of Transesterification Reactions by a Self-Assembled Nanosystem. *Int J Mol Sci* **2013**, *14* (1), 2011–2021. https://doi.org/10.3390/ijms14012011.

(27) Al-Garawi, Z. S.; McIntosh, B. A.; Neill-Hall, D.; Hatimy, A. A.; Sweet, S. M.; Bagley, M. C.; Serpell, L. C. The Amyloid Architecture Provides a Scaffold for Enzyme-like Catalysts. *Nanoscale* **2017**, *9* (30), 10773–10783. https://doi.org/10.1039/c7nr02675g.

(28) Nothling, M. D.; Ganesan, A.; Condic-Jurkic, K.; Pressly, E.; Davalos, A.; Gotrik, M. R.; Xiao, Z.; Khoshdel, E.; Hawker, C. J.; O'Mara, M. L.; Coote, M. L.; Connal, L. A. Simple Design of an Enzyme-Inspired Supported Catalyst Based on a Catalytic Triad. *Chem* **2017**, *2* (5), 732–745. https://doi.org/10.1016/j.chempr.2017.04.004.

(29) Gulseren, G.; Khalily, M. A.; Tekinay, A. B.; Guler, M. O. Catalytic Supramolecular Self-Assembled Peptide Nanostructures for Ester Hydrolysis. *J Mater Chem B* **2016**, *4* (26), 4605–4611. https://doi.org/10.1039/c6tb00795c.

(30) Gülseren, G.; Saylam, A.; Marion, A.; Özçubukçu, S. Fullerene-Based Mimics of Biocatalysts Show Remarkable Activity and Modularity. *ACS Appl Mater Interfaces* **2021**, *13* (38), 45854–45863. https://doi.org/10.1021/acsami.1c11516.

(31) Soylemez, S.; Dolgun, V.; Özçubukçu, S. Fullerene-Based Mimics of Enhanced Acetylcholine Detection for the Diagnosis of Alzheimer's Disease. *Microchemical Journal* **2023**, *193*, 1–9. https://doi.org/10.1016/j.microc.2023.109099.

(32) Demirsoy, Z.; Gulseren, G. Self-Assembled Fullerene Nanostructures for Mimicking and Understanding of Natural Enzymes. *ACS Appl Nano Mater* **2022**, *5* (10), 14285–14295. https://doi.org/10.1021/acsanm.2c02194.

(33) Yeniterzi, D.; Demirsoy, Z.; Saylam, A.; Özçubukçu, S.; Gülseren, G. Nanoarchitectonics of Fullerene-Based Enzyme Mimics for Osteogenic Induction of Stem Cells. *Macromol Biosci* **2022**, *22* (9), 1–11. https://doi.org/10.1002/mabi.202200079.

(34) Privett, B. J.; Shin, J. H.; Schoenfisch, M. H. Electrochemical Sensors. *Anal Chem* **2010**, *82* (12), 4723–4741. https://doi.org/10.1021/ac101075n.

(35) Chen, C.; Wang, J. Optical Biosensors: An Exhaustive and Comprehensive Review. *Analyst* **2020**, *145* (5), 1605–1628. https://doi.org/10.1039/c9an01998g.

(36) Naresh, V.; Lee, N. A Review on Biosensors and Recent Development of Nanostructured Materials-Enabled Biosensors. *Sensors (Switzerland)* **2021**, *21* (4), 1–35. https://doi.org/10.3390/s21041109.

(37) Rusmini, F.; Zhong, Z.; Feijen, J. Protein Immobilization Strategies for Protein Biochips. *Biomacromolecules* **2007**, *8* (6), 1775–1789. https://doi.org/10.1021/bm061197b.

(38) Piradashvili, K.; Alexandrino, E. M.; Wurm, F. R.; Landfester, K. Reactions and Polymerizations at the Liquid-Liquid Interface. *Chem Rev* **2016**, *116* (4), 2141–2169. https://doi.org/10.1021/acs.chemrev.5b00567.

(39) Rodrigues, R. C.; Berenguer-Murcia, Á.; Carballares, D.; Morellon-Sterling, R.; Fernandez-Lafuente, R. Stabilization of Enzymes via Immobilization:

Multipoint Covalent Attachment and Other Stabilization Strategies. *Biotechnol Adv* **2021**, *52*, 1–37. https://doi.org/10.1016/j.biotechadv.2021.107821.

(40) Lockwood, N. A.; Gupta, J. K.; Abbott, N. L. Self-Assembly of Amphiphiles, Polymers and Proteins at Interfaces between Thermotropic Liquid Crystals and Aqueous Phases. *Surf Sci Rep* **2008**, *63* (6), 255–293. https://doi.org/10.1016/j.surfrep.2008.02.002.

(41) Miller, D. S.; Wang, X.; Abbott, N. L. Design of Functional Materials Based on Liquid Crystalline Droplets. *Chemistry of Materials* **2014**, *26* (1), 496–506. https://doi.org/10.1021/cm4025028.

(42) Loudet, J.-C.; Barois, P.; Poulin, P. Colloidal Ordering from Phase Separation in a Liquid-Crystalline Continuous Phase. *Nature* **2000**, *407* (6804), 611–613.

(43) Bai, Y.; Abbasi, R.; Wang, C.; Abbott, N. L. Liquid Crystals Anchored on Mixed Monolayers of Chiral versus Achiral Molecules: Continuous Change in Orientation as a Function of Enantiomeric Excess. *Angewandte Chemie - International Edition* **2014**, *53* (31), 8079–8083. https://doi.org/10.1002/anie.201402770.

(44) Malone, S. M.; Schwartz, D. K. Macroscopic Liquid Crystal Response to Isolated DNA Helices. *Langmuir* **2011**, *27* (19), 11767–11772. https://doi.org/10.1021/la202640a.

(45) Jang, C. H.; Cheng, L. L.; Olsen, C. W.; Abbott, N. L. Anchoring of Nematic Liquid Crystals on Viruses with Different Envelope Structures. *Nano Lett* **2006**, *6* (5), 1053–1058. https://doi.org/10.1021/nl060625g.

(46) Lowe, A. M.; Ozer, B. H.; Bai, Y.; Bertics, P. J.; Abbott, N. L. Design of Surfaces for Liquid Crystal-Based Bioanalytical Assays. *ACS Appl Mater Interfaces* **2010**, *2* (3), 722–731. https://doi.org/10.1021/am900753v.

(47) Luk, Y. Y.; Tingey, M. L.; Dickson, K. A.; Raines, R. T.; Abbott, N. L. Imaging the Binding Ability of Proteins Immobilized on Surfaces with Different Orientations by Using Liquid Crystals. *J Am Chem Soc* **2004**, *126* (29), 9024–9032. https://doi.org/10.1021/ja0398565.

(48) Govindaraju, T.; Bertics, P. J.; Raines, R. T.; Abbott, N. L. Using Measurements of Anchoring Energies of Liquid Crystals on Surfaces to Quantify Proteins Captured by Immobilized Ligands. *J Am Chem Soc* **2007**, *129* (36), 11223–11231. https://doi.org/10.1021/ja073203x.

(49) Gupta, J. K.; Zimmerman, J. S.; De Pablo, J. J.; Caruso, F.; Abbott, N. L. Characterization of Adsorbate-Induced Ordering Transitions of Liquid Crystals within Monodisperse Droplets. *Langmuir* **2009**, *25* (16), 9016–9024. https://doi.org/10.1021/la900786b.

(50) Gupta, J. K.; Sivakumar, S.; Caruso, F.; Abbott, N. L. Size-Dependent Ordering of Liquid Crystals Observed in Polymeric Capsules with Micrometer and Smaller Diameters. *Angewandte Chemie - International Edition* **2009**, *48* (9), 1652–1655. https://doi.org/10.1002/anie.200804500.

(51) Sivakumar, S.; Wark, K. L.; Gupta, J. K.; Abbott, N. L.; Caruso, F. Liquid Crystal Emulsions as the Basis of Biological Sensors for the Optical Detection of Bacteria and Viruses. *Adv Funct Mater* **2009**, *19* (14), 2260–2265. https://doi.org/10.1002/adfm.200900399.

(52) Şengül, S.; Aydoğan, N.; Bukusoglu, E. Nanoparticle Adsorption Induced Configurations of Nematic Liquid Crystal Droplets. *J Colloid Interface Sci* **2022**, *608*, 2310–2320. https://doi.org/10.1016/j.jcis.2021.10.156.

(53) Hamlington, B. D.; Steinhaus, B.; Feng, J. J.; Link, D.; Shelley, M. J.; Shen, A. Q. Liquid Crystal Droplet Production in a Microfluidic Device. *Liq Cryst* **2007**, *34* (7), 861–870. https://doi.org/10.1080/02678290601171485.

(54) Miller, D. S.; Wang, X.; Buchen, J.; Lavrentovich, O. D.; Abbott, N. L. Analysis of the Internal Configurations of Droplets of Liquid Crystal Using

Flow Cytometry. *Anal Chem* **2013**, *85* (21), 10296–10303. https://doi.org/10.1021/ac4021193.

(55) Zhong, S.; Jang, C. H. Nematic Liquid Crystals Confined in Microcapillaries for Imaging Phenomena at Liquid-Liquid Interfaces. *Soft Matter* **2015**, *11* (35), 6999–7004. https://doi.org/10.1039/c5sm01320h.

(56) An, Z.; Jang, C. H. Sensitive and Selective Method for Detecting Cysteine Based on Optical Properties of Liquid Crystal. *Sens Actuators B Chem* **2018**, *269*, 135–142. https://doi.org/10.1016/j.snb.2018.04.168.

(57) Karausta, A.; Kocaman, C.; Bukusoglu, E. Controlling the Shapes and Internal Complexity of the Polymeric Particles Using Liquid Crystal-Templates Confined into Microwells. *J Mol Liq* **2021**, *324*, 1–8. https://doi.org/10.1016/j.molliq.2020.114710.

(58) Gupta, J. K.; Meli, M. V.; Teren, S.; Abbott, N. L. Elastic Energy-Driven Phase Separation of Phospholipid Monolayers at the Nematic Liquid-Crystal-Aqueous Interface. *Phys Rev Lett* **2008**, *100* (4), 1–4. https://doi.org/10.1103/PhysRevLett.100.048301.

(59) Gupta, J. K.; Abbott, N. L. Principles for Manipulation of the Lateral Organization of Aqueous-Soluble Surface-Active Molecules at the Liquid Crystal - Aqueous Interface. *Langmuir* **2009**, *25* (4), 2026–2033. https://doi.org/10.1021/la803475c.

(60) Brake, J. M.; Abbott, N. L. An Experimental System for Imaging the Reversible Adsorption of Amphiphiles at Aqueous-Liquid Crystal Interfaces. *Langmuir* **2002**, *18* (16), 6101–6109. https://doi.org/10.1021/la011746t.

(61) Park, C. S.; Iwabata, K.; Sridhar, U.; Tsuei, M.; Singh, K.; Kim, Y. K.; Thayumanavan, S.; Abbott, N. L. A New Strategy for Reporting Specific Protein Binding Events at Aqueous-Liquid Crystal Interfaces in the Presence of Non-Specific Proteins. *ACS Appl Mater Interfaces* **2020**, *12* (7), 7869–7878. https://doi.org/10.1021/acsami.9b16867.

(62) Zhang, R. H.; Hu, Q. Z.; Kang, Q.; Qı, L. Bin; Pang, Y. P.; Yu, L. Research on Competitive Enzymatic Hydrolysis-Assisted Liquid Crystal-Based Acetylcholine Sensor. *Chinese Journal of Analytical Chemistry* **2021**, *49* (2), 1–6. https://doi.org/10.1016/S1872-2040(20)60081-0.

(63) Brake, J. M.; Daschner, M. K.; Abbott, N. L. Formation and Characterization of Phospholipid Monolayers Spontaneously Assembled at Interfaces between Aqueous Phases and Thermotropic Liquid Crystals. *Langmuir* **2005**, *21* (6), 2218–2228. https://doi.org/10.1021/la0482397.

(64) Zografi, G.; Verger, R.; De Haas, G. H. Kinetic Analysis of the Hydrolysis of Lecithin Monolayers by Phospholipase A. *Chem. Phys. Lipids* **1971**, *7*, 185–206.

(65) Hussain, Z.; Zafiu, C.; Küpcü, S.; Pivetta, L.; Hollfelder, N.; Masutani, A.; Kilickiran, P.; Sinner, E. K. Liquid Crystal Based Sensors Monitoring Lipase Activity: A New Rapid and Sensitive Method for Cytotoxicity Assays. *Biosens Bioelectron* **2014**, *56*, 210–216. https://doi.org/10.1016/j.bios.2013.12.055.

(66) Sun, H.; Yin, F.; Liu, X.; Jiang, T.; Ma, Y.; Gao, G.; Shi, J.; Hu, Q. Development of a Liquid Crystal-Based α-Glucosidase Assay to Detect Anti-Diabetic Drugs. *Microchemical Journal* **2021**, *167*. https://doi.org/10.1016/j.microc.2021.106323.

(67) Wang, Y.; Hu, Q.; Tian, T.; Gao, Y.; Yu, L. A Liquid Crystal-Based Sensor for the Simple and Sensitive Detection of Cellulase and Cysteine. *Colloids Surf B Biointerfaces* **2016**, *147*, 100–105. https://doi.org/10.1016/j.colsurfb.2016.07.059.

(68) Lu, S.; Guo, Y.; Qi, L.; Hu, Q.; Yu, L. Highly Sensitive and Label-Free Detection of Catalase by a H2O2-Responsive Liquid Crystal Sensing Platform. *Sens Actuators B Chem* **2021**, *344*. https://doi.org/10.1016/j.snb.2021.130279.

(69) Hu, Q. Z.; Jang, C. H. Using Liquid Crystals for the Real-Time Detection of Urease at Aqueous/Liquid Crystal Interfaces. *J Mater Sci* **2012**, *47* (2), 969–975. https://doi.org/10.1007/s10853-011-5876-y.

(70) Murray, B. S. Equilibrium and Dynamic Surface Pressure-Area Measurements on protein Films at Air-Water and Oil-Water Interfaces. *Colloids Surf A Physicochem Eng Asp* **1997**, *125* (2–3), 73–83.

(71) Murray, B. S.; Nelson, P. V. Letters A Novel Langmuir Trough for Equilibrium and Dynamic Measurements on Air-Water and Oil-Water Monolayers. *American Chemical Society* **1996**, *12* (25), 5974–5976.

(72) Dickinson, E. Adsorbed Protein Layers at Fluid Interfaces: Interactions, Structure and Surface Rheology. *Colloids Surf B Biointerfaces* **1999**, *15*, 161–176.

(73) Liu, D.; Jang, C. H. A New Strategy for Imaging Urease Activity Using Liquid Crystal Droplet Patterns Formed on Solid Surfaces. *Sens Actuators B Chem* **2014**, *193*, 770–773. https://doi.org/10.1016/j.snb.2013.12.033.

(74) Jannat, M.; Yang, K. L. Continuous Protease Assays Using Liquid Crystal as a Reporter. *Sens Actuators B Chem* **2018**, *269*, 8–14. https://doi.org/10.1016/j.snb.2018.04.125.

(75) Sil, S.; Mishra, K.; Pal, S. K. Liquid Crystal Biosensors: An Overview of Techniques to Monitor Enzyme Activity. *Langmuir* **2025**, *41* (8), 4959–4975. https://doi.org/10.1021/acs.langmuir.4c04395.

(76) Xu, Y.; Rather, A. M.; Song, S.; Fang, J. C.; Dupont, R. L.; Kara, U. I.; Chang, Y.; Paulson, J. A.; Qin, R.; Bao, X.; Wang, X. Ultrasensitive and Selective Detection of SARS-CoV-2 Using Thermotropic Liquid Crystals and Image-Based Machine Learning. *Cell Rep Phys Sci* **2020**, *1* (12), 1–14. https://doi.org/10.1016/j.xcrp.2020.100276.

(77) Menger, F. M.; Rizvi, S. A. A. Relationship between Surface Tension and Surface Coverage. *Langmuir* **2011**, *27* (23), 13975–13977. https://doi.org/10.1021/la203009m.

(78) Hyun, C. K.; Choi, J. H.; Kim, J. H.; Ryu, D. D. Y. Enhancement Effect of Polyethylene Glycol on Enzymatic Synthesis of Cephalexin. *Biotechnol Bioeng* **1993**, *41* (6), 654–658. https://doi.org/10.1002/bit.260410608.

(79) Pasut, G.; Sergi, M.; Veronese, F. M. Anti-Cancer PEG-Enzymes: 30 Years Old, but Still a Current Approach. *Adv Drug Deliv Rev* **2008**, *60* (1), 69–78. https://doi.org/10.1016/j.addr.2007.04.018.

(80) İlhan, G.; Carenza, L. N.; Bukusoglu, E. Shear-Induced Structural Transitions in Confined Nematic Soft Interfaces. *Commun Phys* **2025**, *8* (1). https://doi.org/10.1038/s42005-025-02058-5.

(81) Kramer, C. N. *Fullerene Research Advances*; Nova Science Publishers, 2007.

APPENDICES

A. Thermogravimetric analysis of fullerene

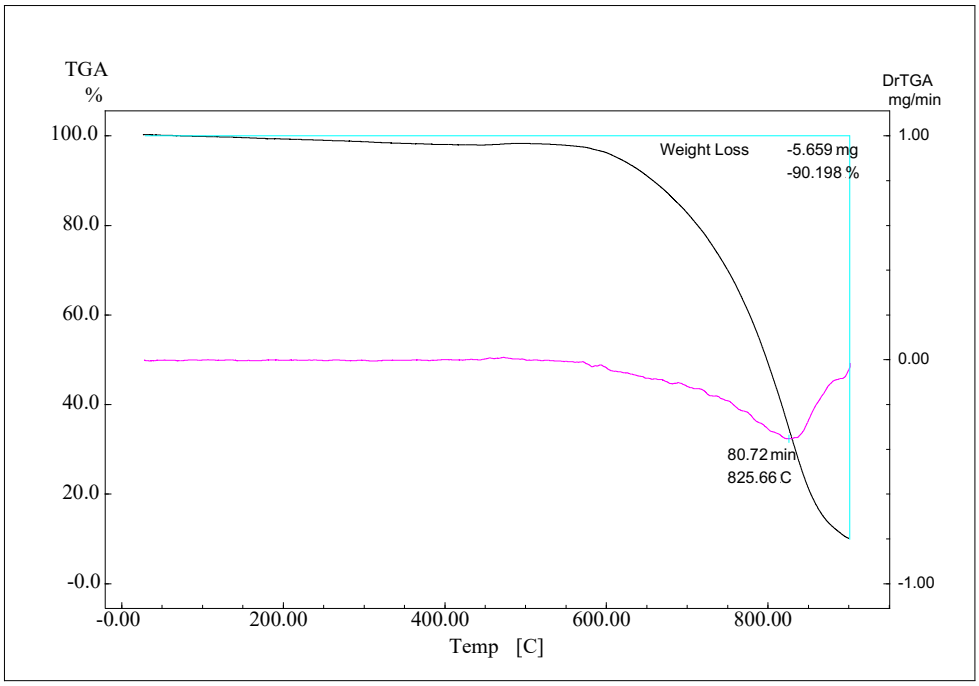

Figure A. 1. Thermogravimetric analysis of fullerene.

B. Thermogravimetric analysis of fullerenol

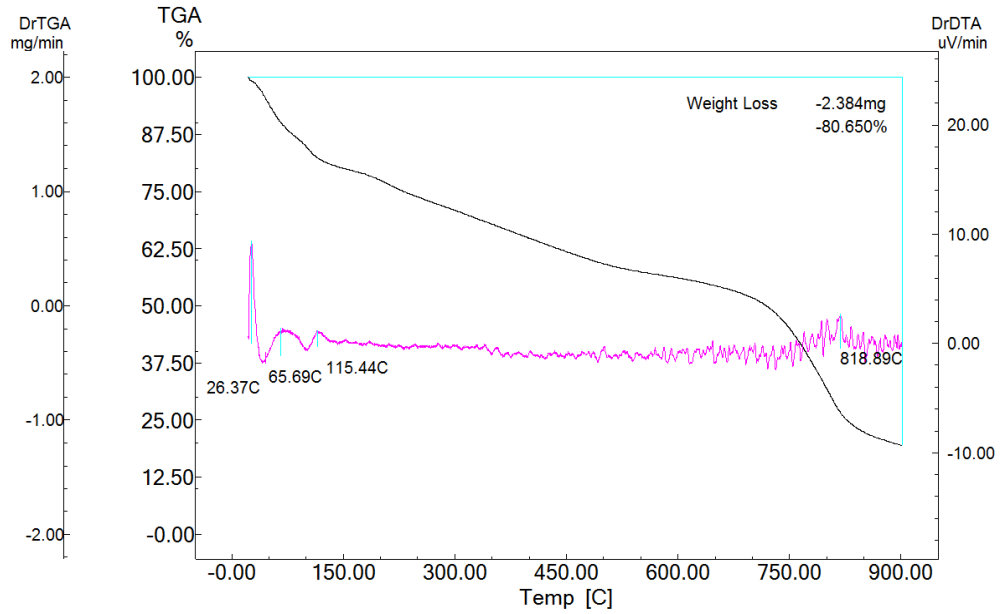

Figure B. 1. Thermogravimetric analysis of fullerenol for hydroxyl group quantification.

About Figure B. 1: The number of OH groups attached to the fullerenol was determined by analyzing it using TGA.[81] The TGA curve shows a mass loss percentage between 150–570 °C (which corresponds to the detachment of -OH groups) and between 570–900 °C (which is attributed to the structural degradation of fullerene). These mass loss percentages, 23.2% for the 150–570 °C range and 37.4% for above 570 °C, were used to calculate the number of OH groups in the fullerenol. The calculation for the number of OH groups was found to be approximately 26, using the formula (720/37.4) × (23.2/17).

C. [1]H-NMR spectrum of activated fullerenol

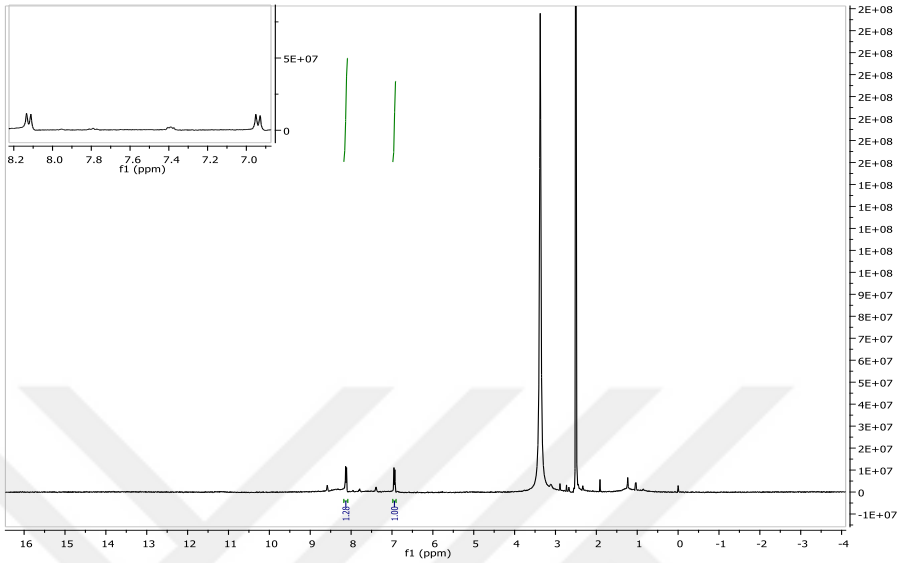

Figure C. 1. [1]H-NMR spectrum of activated fullerenol (400 MHz, DMSO-d6) δ 8.12 (d, J = 9.1 Hz), 6.94 (d, J = 9.1 Hz).

D. ^{1}H-NMR spectrum of Fullerenol-Histidine-Serine (F-HS)

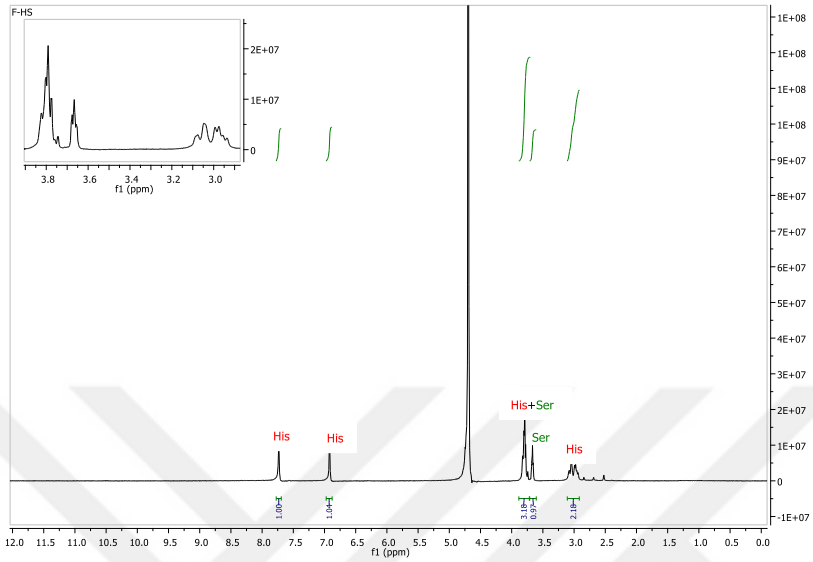

Figure D. 1. ^{1}H-NMR spectrum of F-HS (400 MHz, D_2O) δ 7.73 (s, 1H), 6.91 (s, 1H), 3.86 – 3.75 (m, 3H), 3.71-3.64 (m,1H), 3.15 – 2.90 (m, 2H).

E. [1]H-NMR spectrum of Fullerenol-Serine (F-S)

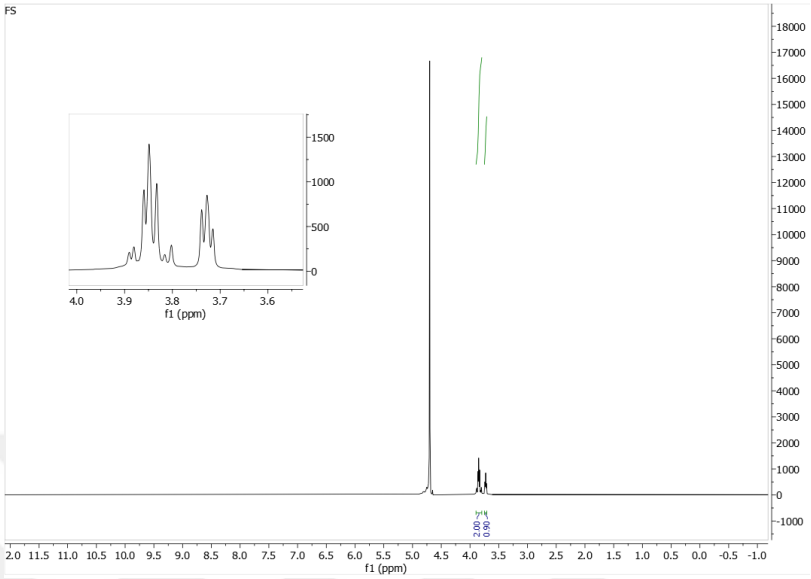

Figure E. 1. [1]H NMR spectrum of F-S (400 MHz, D_2O) δ 3.90 – 3.80 (m, 2H), 3.73 (dd, J = 5.5, 4.0 Hz, 1H).

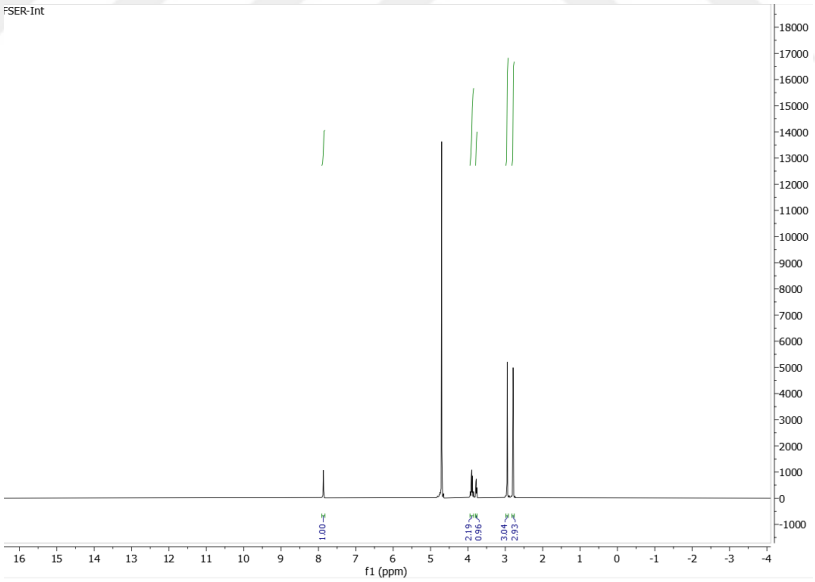

Figure E. 2. [1]H NMR spectrum of F-S and including DMF as internal standard (in D_2O).

About Figure E. 2: The number of substituted serine units (n) was calculated using the internal standard method. 3.0 μL DMF was used as an internal standard and added to the NMR tube along with a known amount of the F-S. By comparing the integrals of known DMF signals with those of the characteristic protons of the serine, the degree of substitution could be determined, allowing for accurate estimation of the molecular weight.

The degree of functionalization of the F–S was calculated using the following equation:

$((105.09\text{n})\ \text{g/mol})\ /\ ([720+105.09n+17(26\text{-}n)]\ g/mol) = x_1/x_2$

Where:

- 105.09 is molecular weight of the serine
- 720 is the molecular weight of fullerene C_{60}
- n is the number of serine conjugated on fullerenol
- 17 indicates the molecular weight of OH while 26 is the number of hydroxy groups on fullerenol molecule
- x_1 (NMR-derived mass) is 3.9 mg and x_2 (actual mass) is 16 mg

Solving this equation, the degree of substitution (n) yielded as 6, resulting in an estimated molecular weight of 1690 g/mol for F-S.

F. ^{1}H-NMR spectrum of Fullerenol-Serine-PEG$_5$ (F-S-PEG)

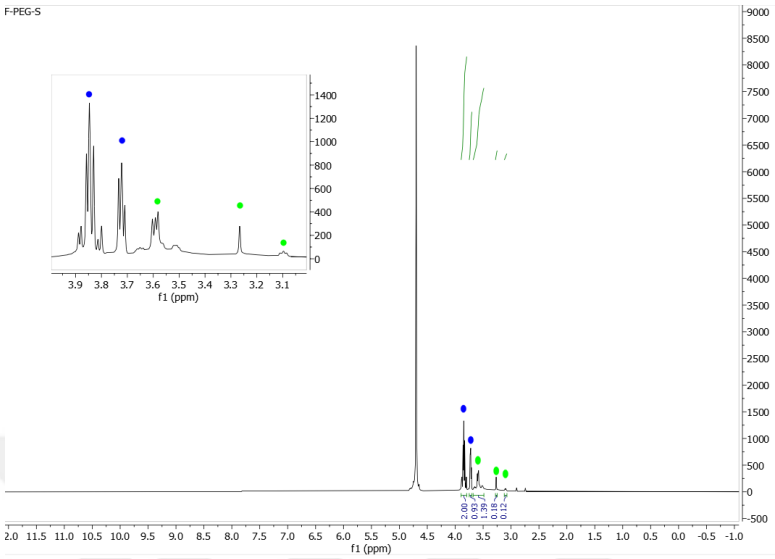

Figure F. 1. ^{1}H NMR spectrum of F-S-PEG$_5$ (400 MHz, D_2O) δ 3.87 (dd, J = 12.5, 4.2 Hz, 1H-Ser), 3.82 (dd, J = 12.2, 5.5 Hz, 1H-Ser), 3.72 (dd, J = 5.4, 4.1 Hz, 1H-Ser), 3.67 – 3.49 (m, 18H- PEG$_5$), 3.27 (s, 3H-PEG$_5$), 3.10 (t, J = 5.0 Hz, 2H-PEG$_5$).

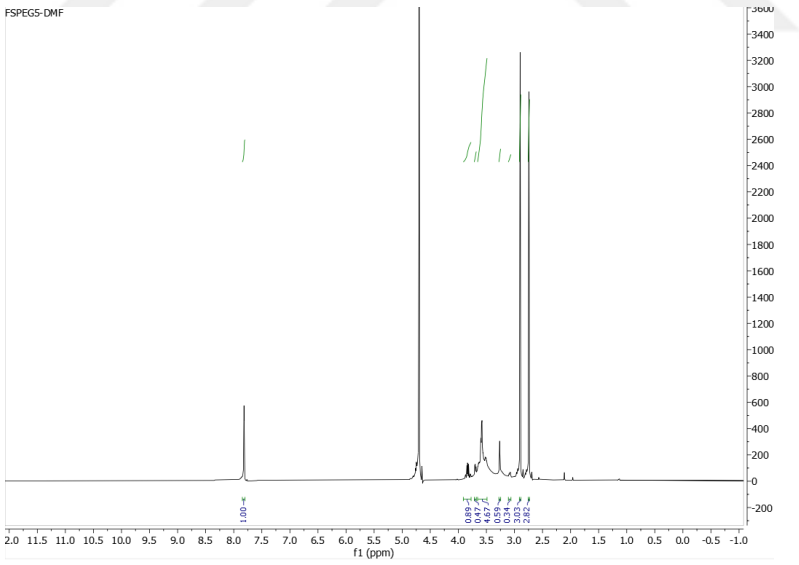

Figure F. 2. ^{1}H NMR spectrum of F-S-PEG$_5$ including DMF as internal standard (in D_2O).

About Figure F. 2: To determine the degree of substitution (*n*) on the fullerenol scaffold, the ratio of the NMR-derived mass (x_1) which was calculated based on the amount of DMF used (5.0 µL) to the actual weighed mass (x_2) of F-S-PEG_5 was used and substituted in the following equation:

$$((105.09n)\ \text{g/mol}) / ([720+105.09n+251.32(0.21n)+17(26-1.21n)]\ \text{g/mol}) = x_1 / x_2$$

Where:

- 105.09 is molecular weight of serine
- 251.32 indicates the molecular weight of m-PEG_5-NH_2
- *n* is the number of serine conjugated on fullerenol
- (26 - 1.21*n*) accounts for the average OH content on fullerenol based on substitution
- 0.21 shows the ratio of the number of proton signals corresponding to PEG_5 to that of serine, derived from NMR integration
- x_1 (NMR-derived mass) is 1.95 mg while x_2 (actual mass of) is 6.6 mg

From this equation, the value of *n* was calculated as 4. Inserting this value into the molecular weight equation yielded an estimated molecular weight of 1550 g/mol for F-S-PEG_5.

G. ^{1}H-NMR spectrum of Fullerenol-Serine-Dodecyl Amine (F-S-C12)

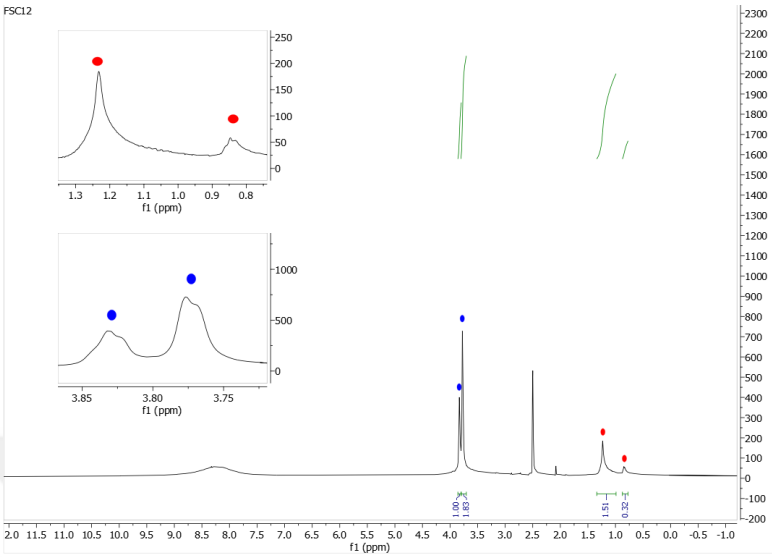

Figure G. 1. ^{1}H NMR (400 MHz, DMSO-d_6) δ 3.83 (m, 1H-Ser), 3.77 (d, J = 4.1 Hz, 2H-Ser), ~2.50 (br s, 2H-C_{12}, overlapped with DMSO-d_6), 1.23 (br s, 20H-C_{12}), 0.84 (t, J = 7.7 Hz, 3H-C_{12}).

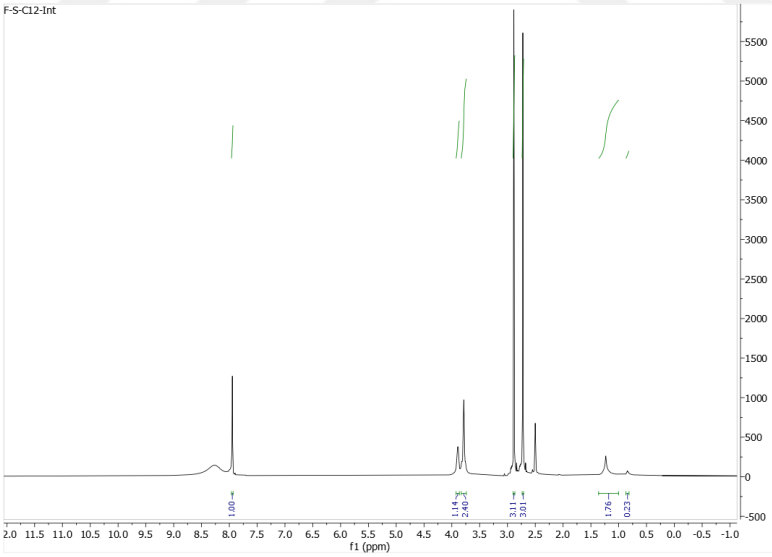

Figure G. 2. ^{1}H NMR spectrum of F-S-C_{12} including DMF as internal standard (in DMSO-d_6).

About Figure G. 2: Degree of functionalization of F-S-C_{12} was calculated from ^{1}H NMR spectrum including DMF as internal standard (5.0 μL) as follows:

((105.09*n*) g/mol) / ([720+105.09*n* +185.36(0.08*n)*+17(26−1.08*n*)] g/mol)= x_1 / x_2

Where:

- 105.09 is molecular weight of serine
- 185.36 indicates the molecular weight of dodecyl amine
- 17 is molecular weight of OH
- *n* is the number of serine conjugated on fullerenol
- 0.06 is the ratio of the number of proton signals corresponding to dodecyl amine to that of serine, derived from NMR integration
- (26 - 1.06*n*) accounts for the average hydroxy group content on fullerenol based on substitution
- x_1 (NMR-derived mass) is 7.3 mg and x_2 (actual mass) is 16.8 mg

Based on this calculation, the value of *n* was calculated as 9 which means 9 serine units were conjugated per F-S-C_{12} leading to an estimated molecular weight of 2180 g/mol for F-S-C12.

H. Interfacial tension measurements of the 5CB-aqueous interface before and after addition of 0.2 mg/mL F-HS

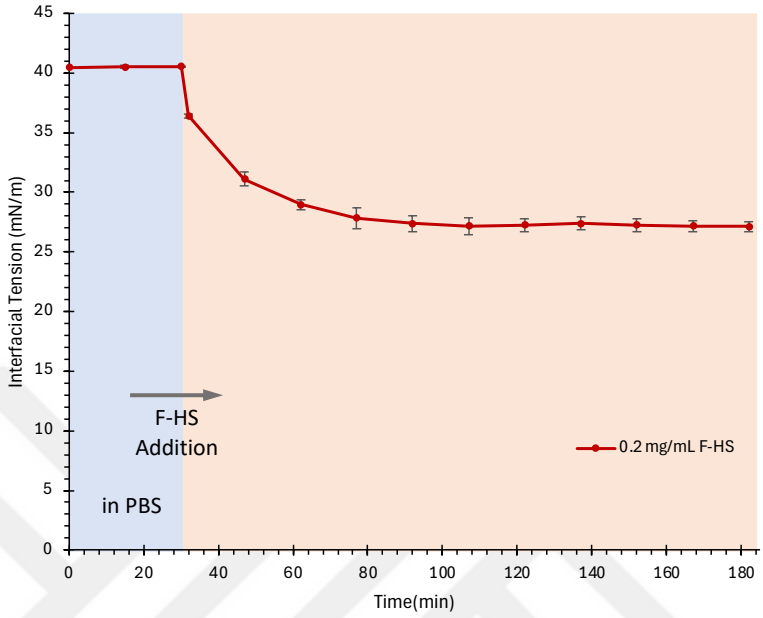

Figure H. 1. Interfacial tension measurements of the 5CB-aqueous interface before and after addition of 0.2 mg/mL F-HS using the pendant drop technique (n=3). All time points were obtained from the averages of ten individual measurements and reported with mean ± standard deviations.

İ. Configuration frequency distributions of 5CB droplets induced by the interaction of 0.2 mg/mL F-HS with varying *p*NPA concentrations

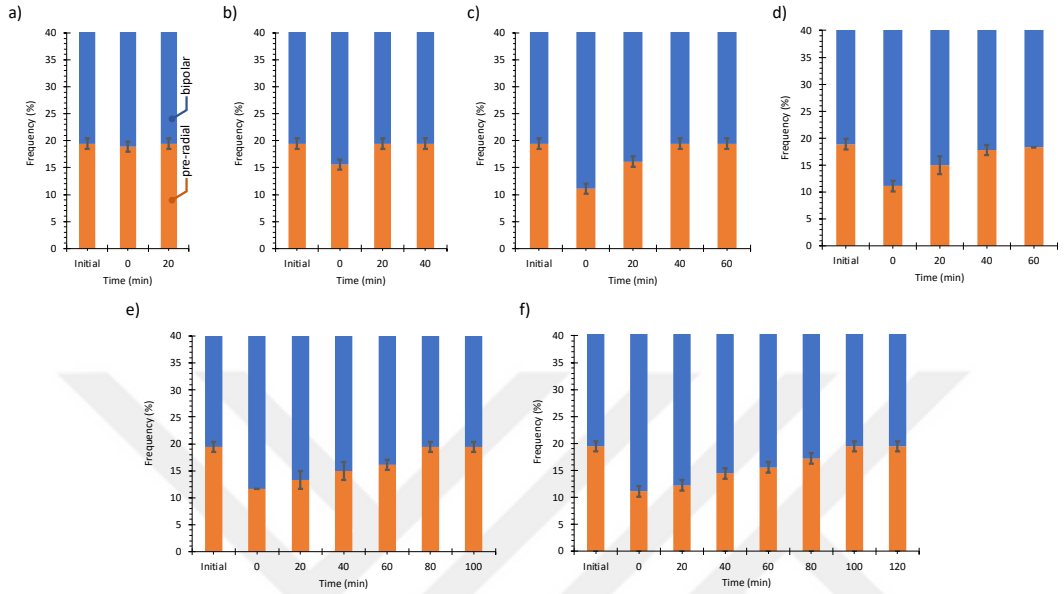

Figure İ. 1. Configuration frequency distributions of 5CB droplets induced by the interaction of 0.2 mg/mL F-HS with (a) 0.02 mM *p*NPA for 20 minutes, (b) 0.05 mM *p*NPA for 40 minutes, (c) 0.1 mM *p*NPA for 60 minutes, (d) 0.2 mM *p*NPA for 60 minutes, (e) 1 mM *p*NPA for 100 minutes, and (f) 1.5 mM *p*NPA for 120 minutes. Each dataset represents averages and standard deviations from three independent measurements (n=3).

J. Configuration frequency distributions of 5CB droplets induced by the interaction of 0.2 mg/mL F-S with varying *p*NPA concentrations

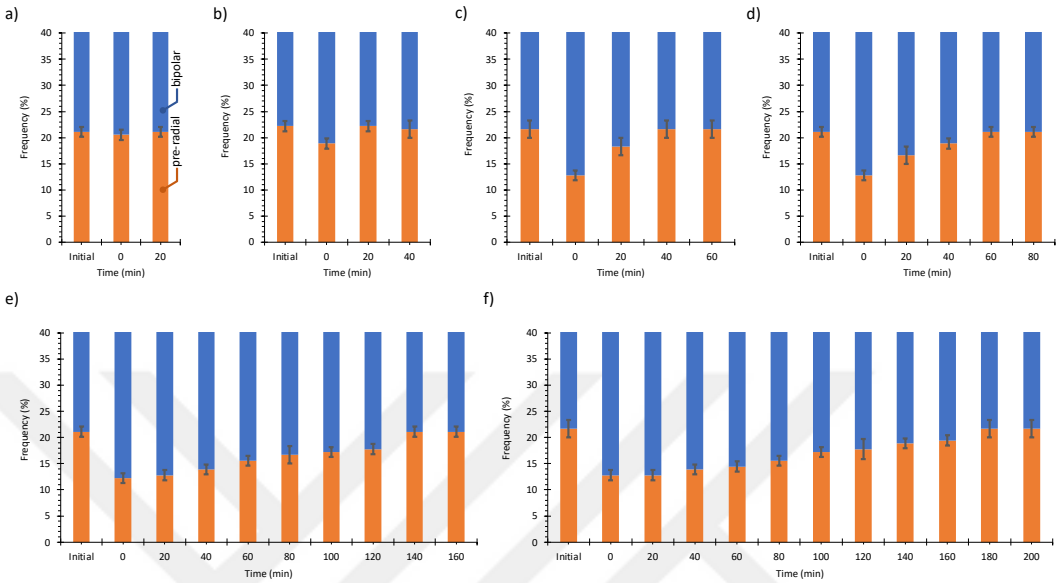

Figure J. 1. Configuration frequency distributions of 5CB droplets induced by the interaction of 0.2 mg/mL F-S with (a) 0.02 mM *p*NPA for 20 minutes, (b) 0.05 mM *p*NPA for 40 minutes, (c) 0.1 mM *p*NPA for 60 minutes, (d) 0.2 mM *p*NPA for 80 minutes, (e) 1 mM *p*NPA for 160 minutes, and (f) 1.5 mM *p*NPA for 200 minutes. Each dataset represents averages and standard deviations from three independent measurements (n=3).

K. Configuration frequency distributions of 5CB droplets induced by the interaction of 0.2 mg/mL F-S-PEG with varying *p*NPA concentrations

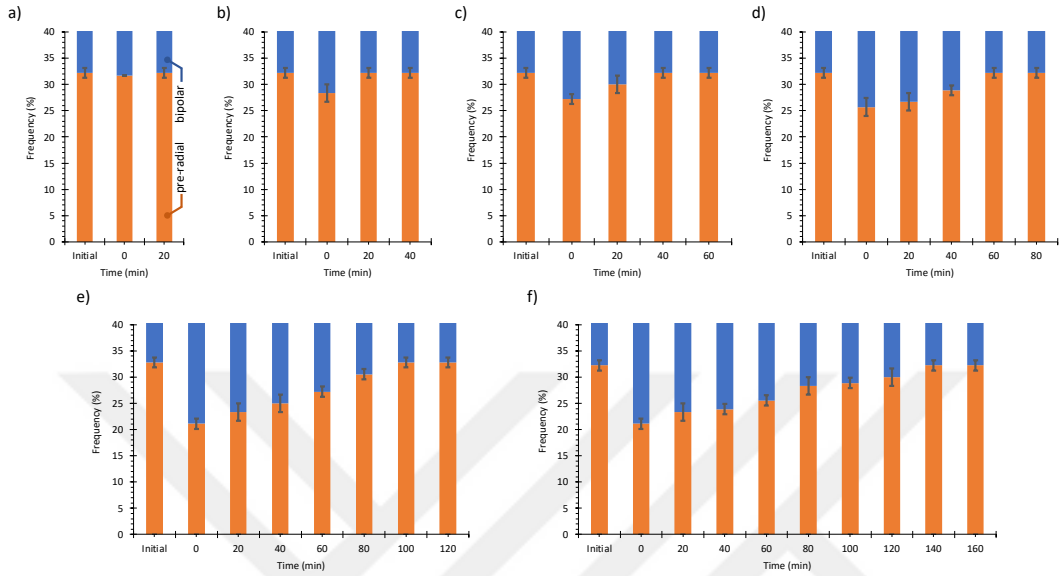

Figure K. 1. Configuration frequency distributions of 5CB droplets in response to 0.2 mg/mL F-S-PEG with varying *p*NPA concentrations and durations: (a) 0.02 mM *p*NPA for 20 minutes, (b) 0.05 mM *p*NPA for 40 minutes, (c) 0.1 mM *p*NPA for 60 minutes, (d) 0.2 mM *p*NPA for 80 minutes, (e) 1 mM *p*NPA for 120 minutes, and (f) 1.5 mM *p*NPA for 160 minutes. Each dataset represents averages and standard deviations from three independent measurements (n=3).

L. Configuration frequency distributions of 5CB droplets induced by the interaction of 0.2 mg/mL F-S-C12 with varying *p*NPA concentrations

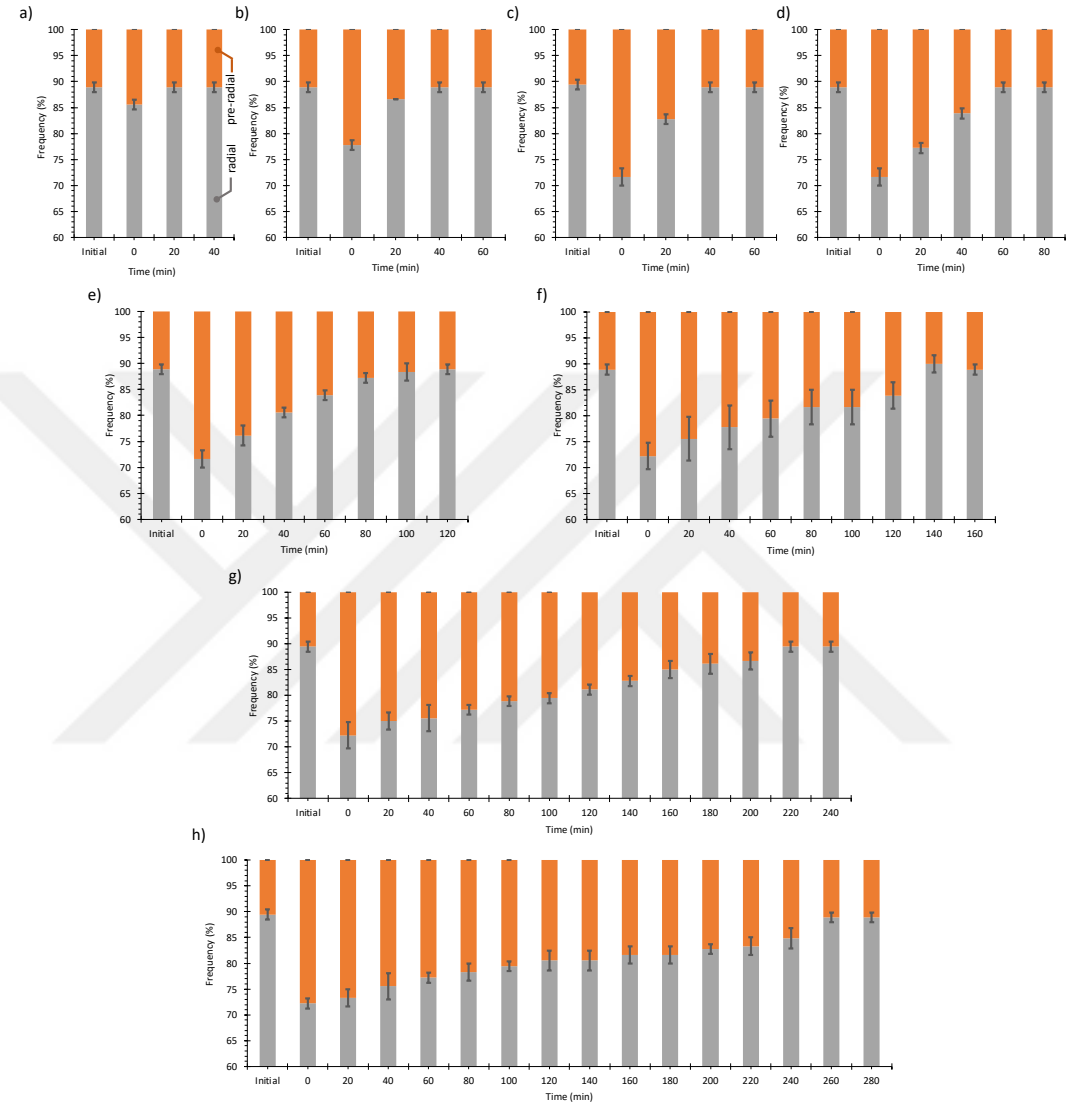

Figure L. 1. Configuration frequency distributions of 5CB droplets induced by the interaction of 0.2 mg/mL F-S-C12 with (a) 0.01 mM *p*NPA for 40 minutes, (b) 0.02 mM *p*NPA for 60 minutes, (c) 0.05 mM *p*NPA for 60 minutes, (d) 0.1 mM *p*NPA for 80 minutes, (e) 0.2 mM *p*NPA for 120 minutes, (f) 0.4 mM *p*NPA for 160 minutes, (g) 1 mM *p*NPA for 240 minutes, and (h) 1.5 mM *p*NPA for 280 minutes. Each dataset represents averages and standard deviations from three independent measurements (n=3).

M. Configuration frequency distributions of 5CB droplets induced by the interaction of 0.2 mg/mL enzyme mimics with *p*NP

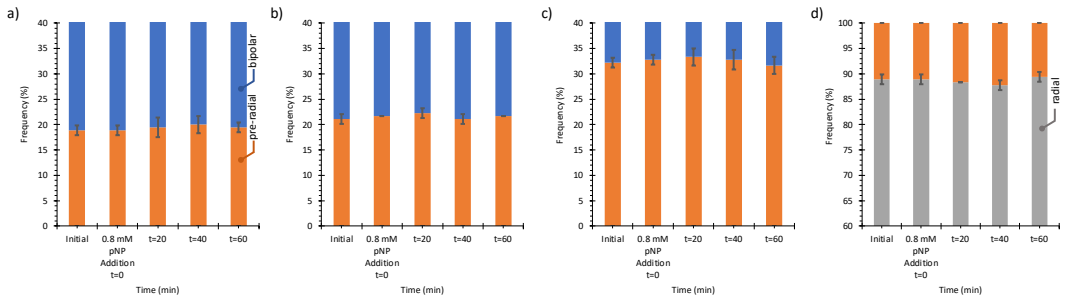

Figure M. 1. Configuration frequency distribution of 5CB droplets obtained in (a) 0.2 mg/mL F-HS, (b) 0.2 mg/mL F-S, (c) 0.2 mg/mL F-S-PEG, and (d) 0.2 mg/mL F-S-C12 enzyme mimics with the addition of 0.8 mM *p*NP for 60 mins. The graphs represent the three independent experiments and reported as mean ± standard deviation.

N. Graphs of time-dependent absorbance along with the associated *p*NP concentration for the interactions of 0.2 mg/mL of F-HS, F-S, F-S-PEG, and F-S-C12 with 1.5 mM *p*NPA

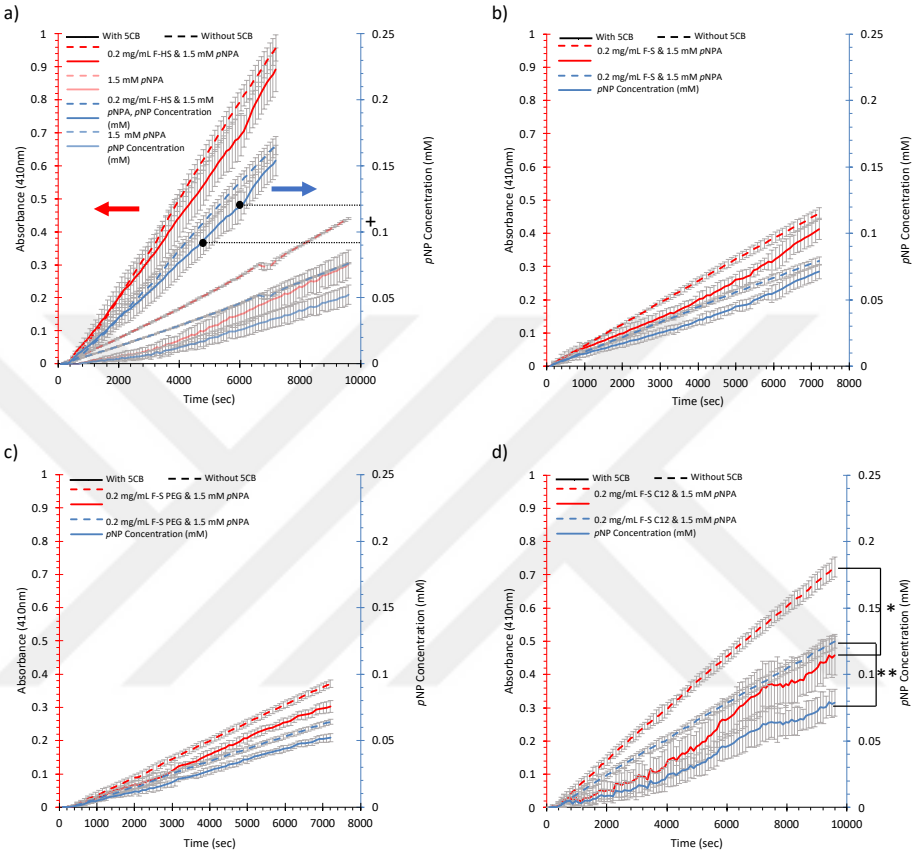

Figure N. 1. Time-dependent absorbance and *p*NP concentrations (mM) for (a) 0.2 mg/mL F-HS with 1.5 mM *p*NPA (7200 s), self-hydrolysis of 1.5 mM *p*NPA (9600 s) shown in muted colors, dark dots represent the recovery time intervals (80-100 mins) and dashed lines mark *p*NP concentrations (mM) at these intervals, with average *p*NP concentration indicated by a plus (+) symbol (b) 0.2 mg/mL F-S with 1.5 mM *p*NPA (7200 s), (c) 0.2 mg/mL F-S PEG with 1.5 mM *p*NPA (7200 s), and (d) 0.2 mg/mL F-S C12 with 1.5 mM *p*NPA (9600 s), measured at 410 nm and room temperature using UV-Vis spectroscopy with and without 5CB. Solid lines represent data with 5CB, dashed lines without 5CB. Graphs represent mean ± standard deviation from three independent experiments.